RAPID

The Imaging Energetic Particle Spectrometer on Cluster

B. WILKEN, W. I. AXFORD, I. DAGLIS, P. DALY, W. GÜTTLER, W. H. IP,
A. KORTH, G. KREMSER, S. LIVI, V. M. VASYLIUNAS and J. WOCH
Max-Planck-Institut für Aeronomie, D-37191 Katlenburg-Lindau, Germany

D. BAKER
Laboratory for Astrophysics and Space Physics, University of Colorado, Boulder, CO 80309, U.S.A.

R. D. BELIAN
Los Alamos National Laboratory, Los Alamos, NM 87545, U.S.A.

J. B. BLAKE, J. F. FENNELL and L. R. LYONS
The Aerospace Corp., Los Angeles, CA 90009, U.S.A.

H. BORG
Institut för Rymdfysik, Swedish Institute of Space Physics, 90187 Umeå, Sweden

T. A. FRITZ
Center of Space Physics, Boston University, MA 02215, U.S.A.

F. GLIEM and R. RATHJE
Institut für Datenverarbeitungsanlagen, Techn. University, D-38023 Braunschweig, Germany

M. GRANDE and D. HALL
*Science and Engineering Research Council, Rutherford Appleton Laboratory, Chilton, 0X11 OQX,
U.K.*

K. KECSUEMÉTY
Central Research Institute for Physics, Academy of Sciences, H-1525 Budapest, Hungary

S. MCKENNA-LAWLOR
Experimental Physics Department, St. Patrick's College, Maynooth, Ireland

K. MURSULA and P. TANSKANEN
Department of Physics, University of Oulu, 90570 Oulu, Finland

Z. PU
Department of Geophysics, Peking University, Beijing 100871, China

I. SANDAHL
Institutet för Rymdfysik, Swedish Institut of Space Physics, 98128 Kiruna, Sweden

E. T. SARRIS
Department of Electronic Engineering, University of Thrace, Xanthi, Greece

M. SCHOLER
Max-Planck-Institut für Extraterr. Physik, 85748 Garching, Germany

M. SCHULZ
Lockheed Research Laboratory, Palo Alto, CA 94304, U.S.A.

F. SØRASS and S. ULLALAND
Physics Department, University of Bergen, 5007 Bergen, Norway

Abstract. The RAPID spectrometer (Research with Adaptive Particle Imaging Detectors) for the Cluster mission is an advanced particle detector for the analysis of suprathermal plasma distributions in the energy range from 20–400 keV for electrons, 40 keV–1500 keV (4000 keV) for hydrogen, and 10 keV nucl^{-1}–1500 keV (4000 keV) for heavier ions. Novel detector concepts in combination with pin-hole acceptance allow the measurement of angular distributions over a range of 180° in polar angle for either species. Identification of the ionic component (particle mass A) is based on a two-dimensional analysis of the particle's velocity and energy. Electrons are identified by the well-known energy-range relationship. Details of the detection techniques and in-orbit operations are described. Scientific objectives of this investigation are highlighted by the discussion of selected critical issues in geospace.

Table of Contents

1. Introduction

Over many years of intense research the Earth's magnetosphere has emerged as a highly structured and dynamic, magnetically contained body of plasma. At times or permanently, parts of the magnetosphere seem to be connected with interplanetary magnetic field lines. The field topology in the outer regions of the magnetosphere and its time dependence is by and large a result of currents carried by the thermal plasma. The suprathermal component, on the other hand, may be less important for most of the macroscopic plasma quantities but it plays an important role on its own right due to peculiarities in the physics of energetic particles. Acceleration processes in the magnetosphere of still unknown nature energise particles in the magnetosphere to hundreds of keV. The relatively fast motion of these particles can carry information about the energisation process over significant distances to an observing platform. Studies of the intensity profile, the energy distribution and the ionic mass and charge composition can provide important clues on the nature of the process. Furthermore, the kinetic properties of these particles can be used as a tool to trace out plasma structures over distances as large as an Earth radius by utilising the particle's gyroradius. Information can even be transmitted over global distances by the rapid drift of energetic particles in field gradients or, even more important, by field-aligned swift electrons travelling with speeds comparable with the speed of light. In tail-like field configurations these particles can transmit over very large distances almost instant information on changes in the field topology.

The Cluster polar orbit ($4 \times 19.6 \; R_E$) provides excellent opportunities for energetic particle studies. The physics at the magnetopause, the bow shock, and the near-Earth magnetotail are key regions of interest for the RAPID investigation. The state-of-the-art detection techniques, the large energy range for nuclei and electrons, and the complete coverage of the unit sphere in velocity space lead to the following capabilities:

– Remote-sensing of local density gradients over distances comparable with particle gyroradii. Species-dependent structures in gradients can be studied, gradient motions can be resolved to one spin period ($T = 4$ s).

– Identification of major ion species (H, He, CNO) in the energetic plasma component. A special operational mode allows the identification and analysis of Energetic Neutral Atoms (ENA). The importance of ENAs in the magnetosphere and the detectability with RAPID is briefly described in Section 3.5.

– Characterisation of magnetic-field-line topologies using the fast motion of energetic electrons.

These observational features allow detailed studies in most regions of geospace visited by Cluster. Among a vast number of topics a selection discussed in Section 3 illustrates how RAPID can scrutinise as yet unexplained phenomena.

The RAPID instrument uses two different and independent detector systems for the detection of nuclei and electrons. The Imaging Ion Mass Spectrometer (IIMS) identifies the nuclear mass of incident ions or neutral atoms from the kinetic energy equation: a time-of-flight and energy measurement determines the particle mass. One-dimensional images of spatial intensity distributions result from the projection principle. The Imaging Electron Spectrometer (IES) is dedicated to electron spectroscopy. The well-known energy-range relationship is used to identify electrons over a limited energy range.

Close collaboration with the other Cluster teams is essential to bring to bear the wealth of information expected from this multi-spacecraft mission which indeed offers an unprecedented scientific tool for studies of long-standing problems in the magnetosphere.

An essential complement to the Cluster space segment is the Cluster science data system (CSDS) which is a pre-requisite for bringing together multiple data sets from the 44 Cluster instruments. A successful analysis of the enormous volume of data returned by Cluster requires support by a data network such as CSDS.

Section 2 gives an account of the detection techniques employed in IIMS and IES and expands on specific aspects of the signal processing and data generation in the two segments of RAPID. This Section also provides useful information on the flight operations and the data analysis. Section 3 addresses in some detail selected scientific objectives of the RAPID investigation.

2. Instrumentation

2.1. THE RAPID SPECTROMETER

Outer envelopes of the RAPID spectrometer with some principal dimensions are shown in Figure 1. The instrument is physically a single structure which contains all major elements of the instrument as sketched in Figure 2: the sensor systems IIMS and IES, the front-end electronics or Signal Conditioning Unit (SCU), and the Digital Processing Unit (DPU) with the the Low-Voltage Power-Supply (LVPS) and the spacecraft interface in the back of the box. Figure 3 is a photograph of the EM unit.
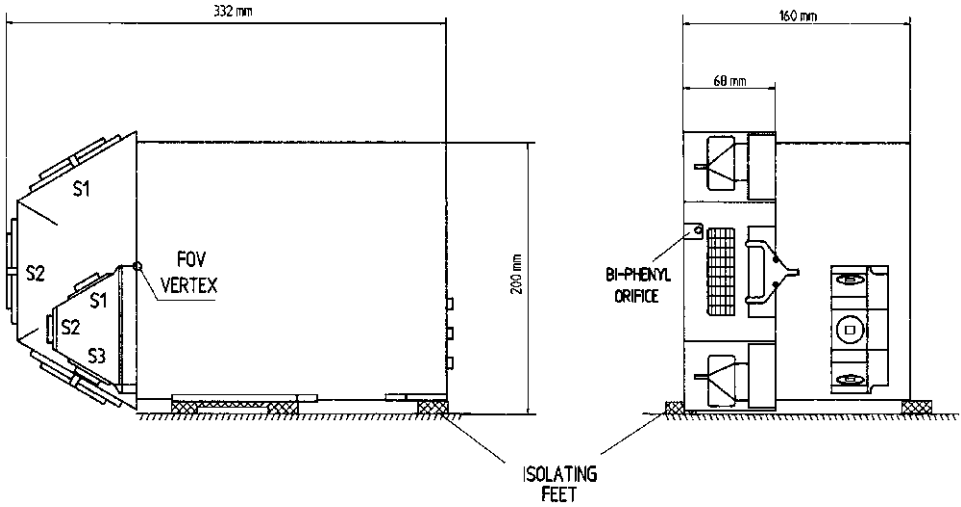
Figure 1. Mechanical configuration of the RAPID instrument showing the sensor system IIMS (on the left side of the unit in the right panel) and IES (small system in the right panel). Individual detector heads are identified by Sn ($n = 1, 2, 3$).
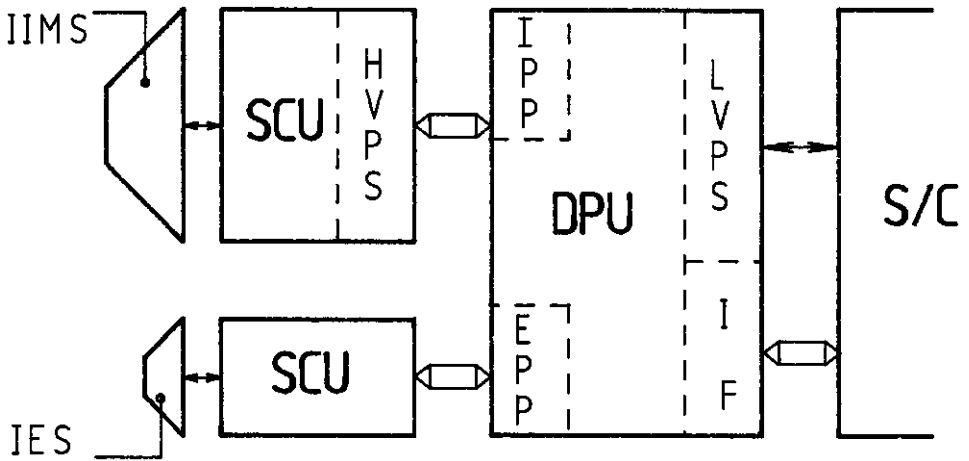
Figure 2. Key components of the dual sensor spectrometer integrated into the single RAPID box structure.

The sensor system for nuclei, the Imaging Ion Mass Spectrometer (IIMS), is composed of three identical SCENIC heads (Spectroscopic Camera for Electrons, Neutral and Ion Composition). The positions of the three systems S1, S2, and S3 in the instrument reference system are marked in Figure 1. Each spectrometer head Sy ($y = 1, 2, 3$) is protected by a mechanical door. After insertion into the vacuum of space the individual door latches are released by bi-phenyl ($C_{12}H_{10}$) operated mechanisms and the doors are rotated into the open position by the action of a
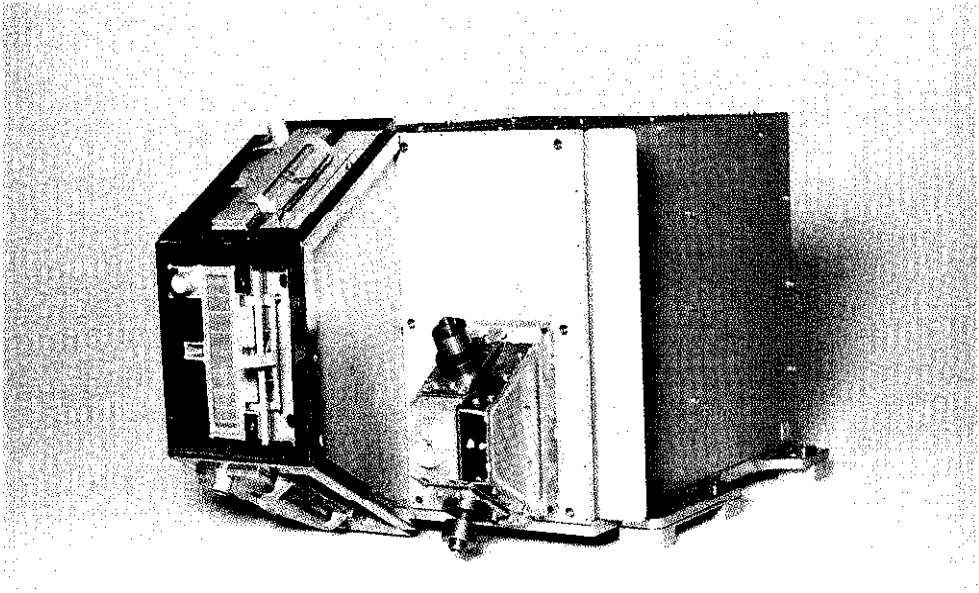
Figure 3. A photograph of the RAPID unit. The sensor system IIMS is on the left side.

spring. An opened door and the orifice for the bi-phenyl evaporation is sketched in Figure 1 for head S2 (right panel in Figure 1). This rather straightforward scheme for an one-shot actuator is based on the vast difference in evaporation speed of large bi-phenyl molecules in air and in vacuum. However, the obvious simplicity of such a device is somewhat offset by the difficulty to predict with reliability the accurate release time due to the uncertainty in the knowledge of the bi-phenyl temperature during the launch phase. Measurements in the laboratory suggest a delay time of about 30 to 40 hours for the doors to be released after launch.

The electron detector, IES, is composed of three identical sensor heads as well, however, the detection technique differs entirely from the principle used in SCENIC. Again the apertures are protected by bi-phenyl operated closures but in this case the 'mechanism' is rather simplified: the tiny entry holes of the IES heads are closed by bi-phenyl 'plugs' which leave the holes open after evaporation in space. The positions of the heads Sn are also shown in Figure 1.

2.1.1. *The Nuclei Detector SCENIC*

The centre piece of the IIMS sensor system is the SCENIC detector head. In essence SCENIC is a miniature telescope composed of a time-of-flight (TOF) and energy (E) detection system. The novel aspect is the imaging of flux distributions and the capability to identify Energetic Neutral Atoms (ENA) in a certain energy band.

The particle-identifying function of the SCENIC spectrometer is obtained from a two-parameter measurement: the particle velocity (V) and the energy (E) are measured as independent quantities, the particle mass A is then uniquely determined either by computation ($A \sim EV^{-2}$) or by statistical analysis in two-dimensional (V, E) space with the mass A as the sorting parameter. Actually the velocity detector measures the flighttime (T) the particle needs to travel a known distance in the detector geometry. The time-of-flight/energy measuring technique is described in detail, e.g., by Wilken (1984).

Figure 4 shows cross-sections of the SCENIC detector telescope drawn to scale. A particular feature is the triangular structure with a $60°$ opening angle. The energy measuring solid-state detectors (SSD) are mounted in the apex at the rear of the system. A group of two SSDs (an energy detector ED and a back detector BD) is combined in an anticoincidence condition for high-energy-electron detection. The flighttime (T) measuring system is the entry element of the telescope. It is essentially composed of a thin foil ($10 \, \mu\text{g cm}^{-2}$ Lexan foil with aluminium coating) and the front surface of detector ED. The distance between the foil and detector ED along the line of symmetry is the nominal flight path for the T-measurement.

Particles passing through the telescope release secondary electrons (SE) from the entry foil. The SE are accelerated and directed to a microchannel plate (MCP) for detection. The MCP output signal constitutes the START signal for the T-measurement. Details of the isochronous SE transfer to the START-MCP are shown in the upper cross-Section of Figure 4. Upon impact of the particle on detector ED secondary electrons are ejected from its surface as well. These SE are transferred to the STOP-MCP by a technique similar to the start electrons. The STOP signal completes the T-measurement.

The energy E of the incident particle, reduced by the loss in the START foil, is measured in detector ED. For sufficiently high energies the particle is able to penetrate detector ED and to strike the back detector BD. This leads to the elimination of the event from analysis as described in Section 2.2.1.

Figure 4 shows the START foil as an elongated rectangle. The design of the START-system is such that the SE transfer to the MCP is not only isochronous but also position-preserving: Four read-out anodes behind the START-MCP (not shown in Figure 4) correspond to four contiguous segments on the entry foil and each of these forms a $12°$ by $15°$ viewing cone with the ED detector in the back of the system. In a sense this geometry can be considered a degenerated case of a 'projection camera' with only one pixel in the back plane. In this special case the 'virtual' image plane coincides with the entrance foil.

Incident particles are strongly collimated before they reach the T/E-telescope. Two microchannel collimators (COLL1 and COLL2 in Figure 4) define a highly anisotropic field-of-view with $6°$ lateral and $60°$ polar opening. A set of plates between the collimating elements with alternating potentials (0 and $+U_{\text{def}}$) forms a linear electrostatic deflector (DEFL). The primary purpose of DEFL is to protect the instrument from overloads due to large fluxes of low-energy particles (e.g.,
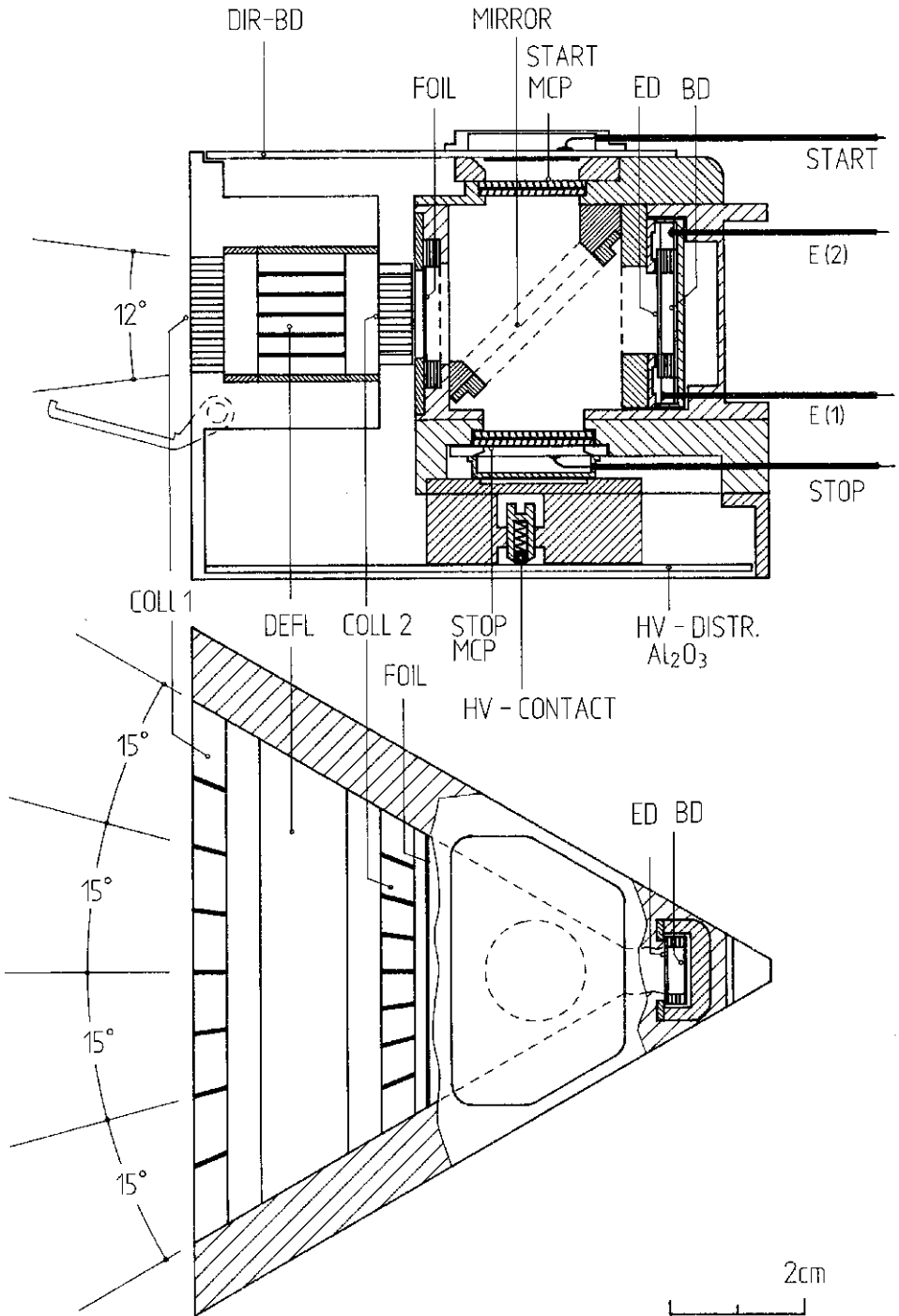
Figure 4. Cross-sections of the SCENIC head. Two narrow collimators (COLL1 and COLL2) and a set of deflection plates (DEFL) form the entry element. The foil (FOIL) and the solid-state detector (ED) define the time-of-flight geometry. The detector BD is in anti-coincidence to ED · Microchannel plates (MCP) detect 'START' and 'STOP' secondary electrons.

Table I
Technical parameters of the SCENIC head

Flightpath s (mean)	34 mm
Field-of-view (total)	$6° \times 60°$
Polar angles	$4 \times 15°$
E-detector (ED)	
Area/thickness	5×15 mm^2/300 μ
B-Detector (BD)	
Area/thickness	5×15 mm^2/300 μ
START foil[a]	
Al/Lexan/Al	63 nm/83 nm/63 nm
Deflection voltage	0–10 kV

[a] The high-quality foils were manufactured by the Luxel Corporation, Friday Harbor, WA (U.S.A.).

solar wind plasma). Some selected technical parameter of the SCENIC head are listed in Table I.

The relatively high gain $g = 10$ achieved with the active collimator with the deflection voltage DEFL set to 10 kV allows efficient separation of energetic neutral atoms (ENA) from ions for energies up to 150 keV (this operational configuration of RAPID is called ENA mode). The energy band between 20 and 150 keV is generally considered important for magnetospheric neutrals produced in the ring current region. RAPID, in the ENA mode, covers the high energy end of the ENA distribution (compare also Section 3.5).

The deflection voltage DEFL can be set to 16 different levels between 0 and 10 kV. Experience with an instrument on GEOTAIL similar to RAPID shows that a rather low level for DEFL (about 1 kV) is sufficient to avoid excessive counting rates in the inner magnetosphere and thus provides adequate protection. There is no plan to operate DEFL at any other level than described above.

The fraction in (E, T) space covered by the SCENIC head is shown in Figure 5 together with calculated loci of major magnetospheric nuclei or groups of nuclei. The width of the particle traces reflects the effect of flight path variations over the $60°$ opening of the SCENIC head. The energy (E) scale from 0 keV up to 4000 keV is partitioned by electronic thresholds A and C which define the lower (30 keV) and the upper (4000 keV) limit of the *measured* energy range. The upper end of the linear energy range B is defined by the last channel of the 8-bit amplitude-to-digital-converter (ADC). The time (T) range extends essentially from 0 ns to 80 ns.

Particles (electrons or nuclei) with sufficient energy to penetrate the ED-detector create a veto signal in the BD-detector which results in the elimination of this event from subsequent analysis.

With reference to Figure 5 the following definitions are used to identify hydrogen, helium, particles of the CNO and Si-Fe groups (carbon, nitrogen, and oxygen
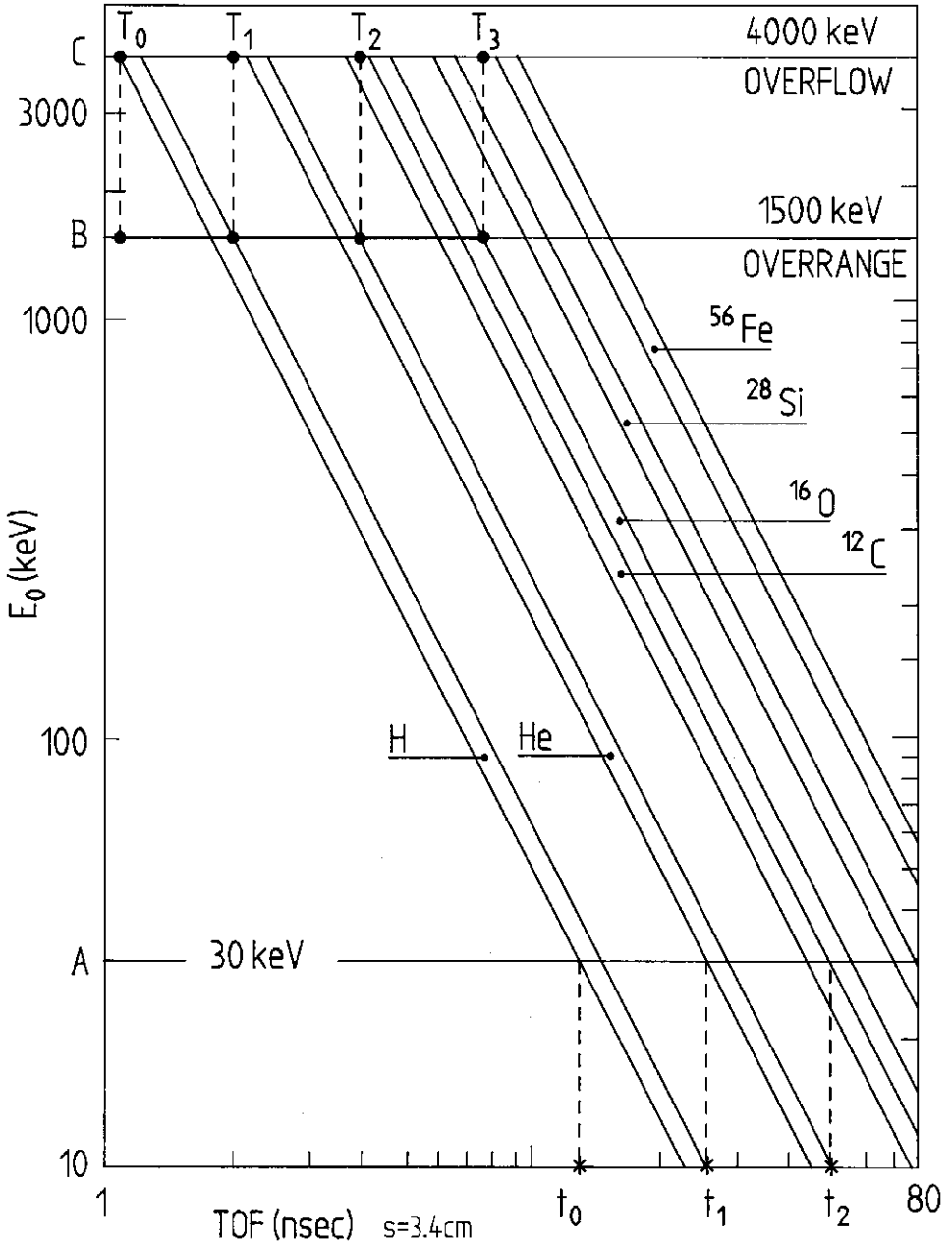
Figure 5. The energy-time plane covered by the IIMS detector. The width of the particle traces reflects the variation of the flight-path in the SCENIC geometry. Energy thresholds *A* and *C* define the lowest energy value accepted and over-range, respectively. The level *B* denotes channel 256 in the energy ADC which is equivalent to the upper limit for the linear energy response.

in the CNO group and particles with masses between silicon and iron in the Si–Fe group cannot be resolved as individual species):

Logic state in the E-channel	T$-$range	Species	Remarks
$\overline{ABC}$	$t0 - t1$	H	Reduced resolution
$\overline{ABC}$	$t1 - t2$	He	Reduced resolution
$A\overline{BC}$	2–80 ns	H, He, CNO, Si–Fe	Nominal resolution
$AB\overline{C}$	$T0 - T1$	H	Unique identification
$AB\overline{C}$	$T1 - T2$	He	Unique identification
$AB\overline{C}$	$T > T2$	CNO and heavier	No mass resolution

Comment:

A and C denote physical threshold, B is defined by the last channel of the energy ADC (upper limit of the linear range).

As mentioned earlier the IIMS sensor system is composed of three identical SCENIC heads in a configuration such that contiguous coverage over $180°$ in the polar angle is achieved (the polar angle is defined with respect to the Cluster spin axis). The sectored rotation of the spacecraft provides the completing azimuthal coordinate. The design features of the SCENIC head combined with the specific layout of the electronic system lead to performance parameters summarised in Table II. It should be noted that hydrogen and helium particles are identified by the time-of-flight T only if the *measured* particle energy is outside the nominal range, i.e., below 30 keV (measured energy $= 0$ keV) or above 1500 keV. In the latter case the measured energy value is constant and equal to E_M (see Table II) which corresponds to the highest ADC channel.

The response functions of the SCENIC head (and likewise of the IIMS sensor system) are generally describe by a complex family of energy-dependent functions parameterised by the particle mass A and the selected type of science data (science data (SD) are defined in Section 2.4.). The conversion from observed counting rates n (cts s^{-1}) to particle flux j in physical units is therefore represented by functions of the form

$$j = [GF \ \varepsilon(E, A; SD)]^{-1} n$$

with GF denoting the geometric factor and ε describing the detection efficiency as a function of particle energy (E), particle mass (A) and selected Science Data (SD).

2.1.2. *The Electron Detector IES*
Electrons with energies from 20 keV and 400 keV are measured with the novel Imaging Electron Spectrometer (IES). Advanced microstrip solid-state detectors

Table II

Characteristic parameters of the IIMS and IES sensor systems

	IIMS	IES
Energy range (keV)		
Hydrogen $(0, T)$	40–75	–
Hydrogen (E, T)	75–1500	–
Hydrogen $(E_M{}^{\text{a}}, T)$	1500–4000	–
Helium $(0, T)$	40–100	–
Helium (E, T)	100–1500	–
Helium (E_M^{a}, T)	1500–4000	–
CNO	210–1500 (oxygen)	–
Electrons	–	20–400
ENA	40–200	–
Mass classes (amu)	1, 4, 12–16, 28–56	–
Mass resolution (A/dA)	4 (oxygen)	–
Field-of-view	$\pm 3° \times 180°$	$\pm 17.5° \times 180°$
Angular coverage		
Polar (range/intervals)	$180°/12$	$180°/9$
Azimuthal (range/sectors)	$360°/16$	$360°/16$
Deflection voltage (kV)		
Range/steps	0–10/16	–
Geometric factor (cm^2 sr)		
Total $(180°)$/per pixel	$2.7 \times 10^{-2}/2.2 \times 10^{-3}$	$2.0 \times 10^{-2}/2.2 \times 10^{-3}$

$^{\text{a}}$ The value E_M corresponds to channel 256 in the energy ADC.

having a 0.5 cm × 1.5 cm planar format with three individual elements form the image plane for three acceptance 'pin-hole' systems. Each system divides a 60° segment into three angular intervals. A schematic cross-Section of an IES pin-hole camera is presented in Figure 6. Three of these detectors arranged in the configuration shown in Figure 1 provide electron measurements over a 180° fan in polar angle. Figure 7 shows an exploded view of the complete IES sensor head with the integrated monolithic Switched Charge/Voltage Converter (SCVC) chip and boards in the stack containing bias resistors and coupling resistors required by the charge sensitive pre-amplifier/detector operation.

The 800-micron-thick ion-implant solid-state devices are covered with a 450 μg cm^{-2} (Si eq) absorbing window which eliminates ions up to 350 keV through the mass dependent range-energy relationship. The principle energy range for IES is shown in Figure 8: The curves labeled e and p show the amount of energy deposited in an 800 μ silicon detector by electrons and protons, respectively. Electrons with energies above E_D penetrate the detector and, as a result, the deposited energy is no longer proportional to the incident energy. Protons, on the other hand, can traverse an absorbing foil in front of the detector only for energies above E_A.

CROSS-SECTION
of the
IES-HEAD

SHIELDING

S 3

S 2

S 1

PINSLIT

ACTIVE
STRIP AREAS

20°

20°

20°
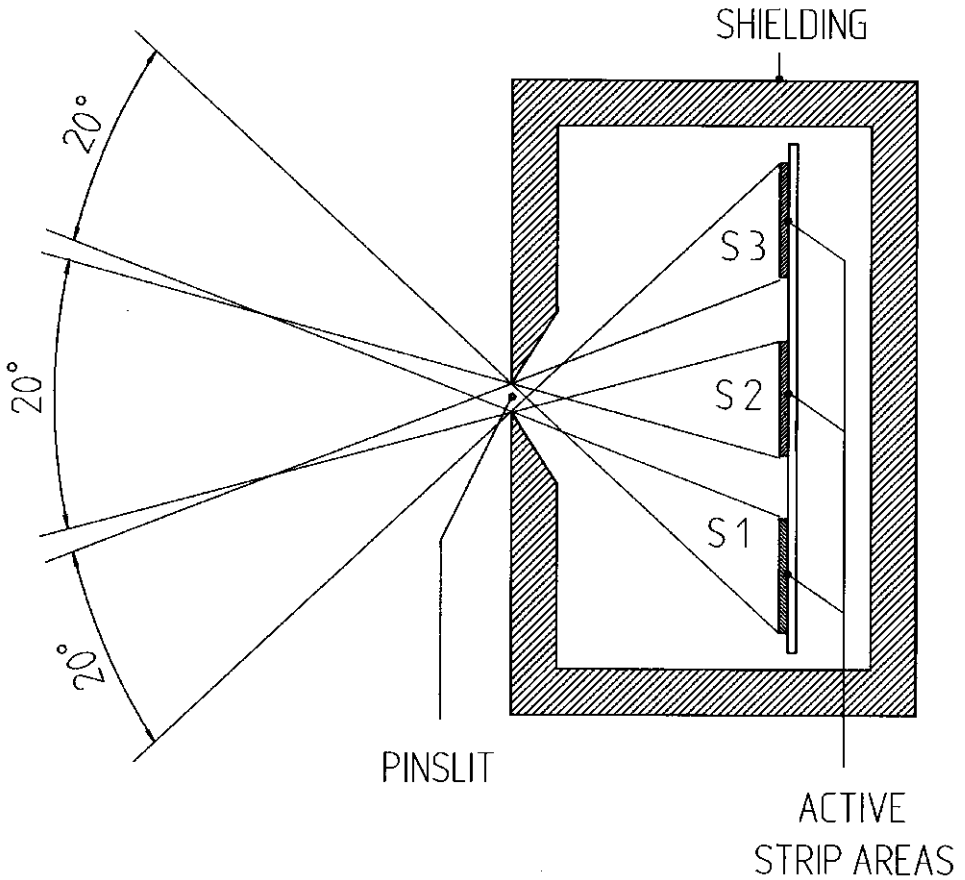
Figure 6. The IES Sensor Concept. Multiple look directions are achieved using a single detector with multiple elements placed behind a pin slit.

The separation of electrons in the nominal range 20–400 keV from high energy electrons $E \leq E_D$ and from protons between E_A and the proton 'veto' discriminator relys on the observational fact that the particle spectra are steeply decreasing with energy.

Figure 9 demonstrates the very good angular resolution obtained with an IES camera for three electron energies (65, 90, and 114 keV). The nine individual strips on the three focal plane detectors are interrogated by the multichannel SCVC circuit.

SPACER
DETECTOR
SPACER/
CONNECTOR
REGISTOR
SPACER/
CONNECTOR
CAPACITOR
RIGHT ANGLE
CONNECTOR
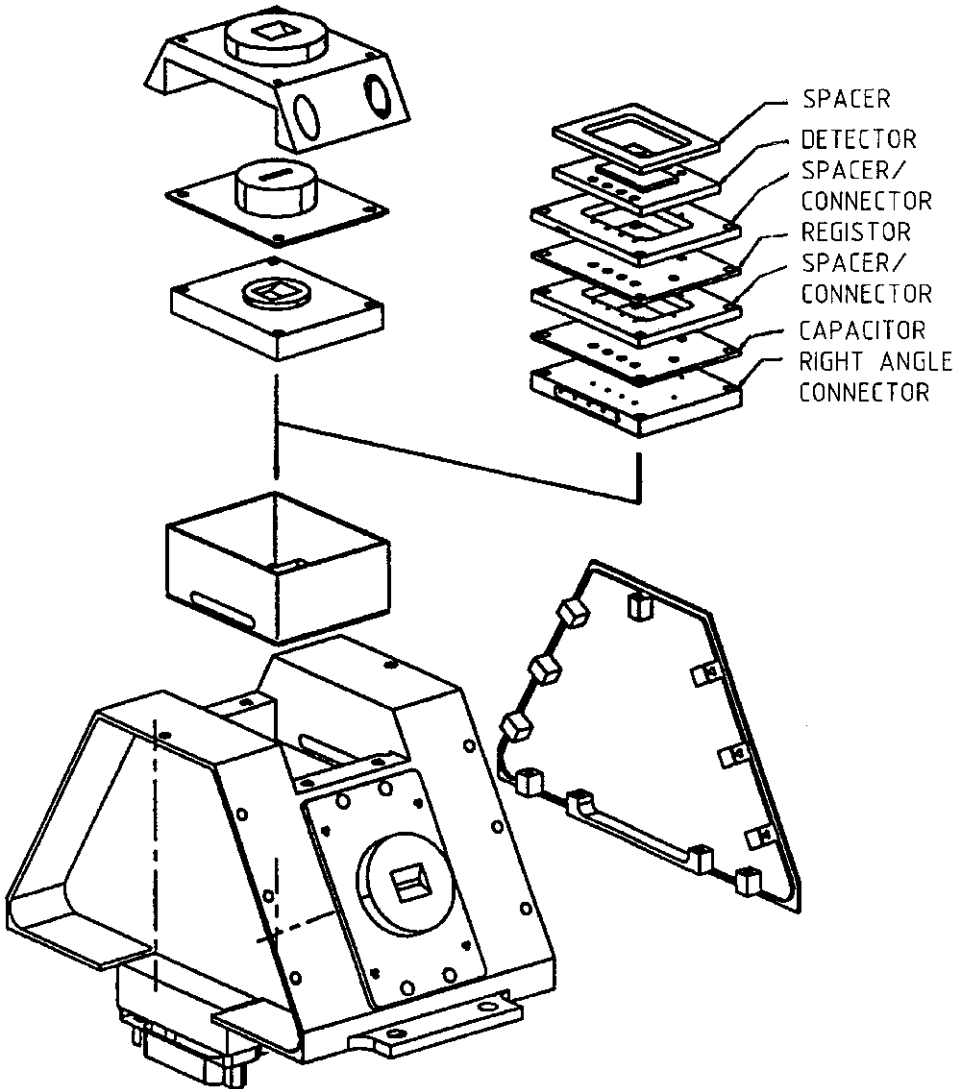
Figure 7. The IES sensor head in an exploded configuration showing the orientation of the three pin slits and the proximity of the microelectronics pre-amplifier board to the sensors. Boards contained in the stack actually contain the bias resistor and coupling capacitors required by the charge sensitive pre-amplifier/detector operation.

The SCVC provides for each particle coded information on the strip number and particle energy. This primary information is transferred to the DPU for further evaluation.

The SCVC is laid out for a total of 16 charge-sensitive pre-amplifier channels of which nine are used in this IES application. The circuit diagram of a single channel in the SCVC chip is shown in Figure 10 (the chip was developed and qualified by
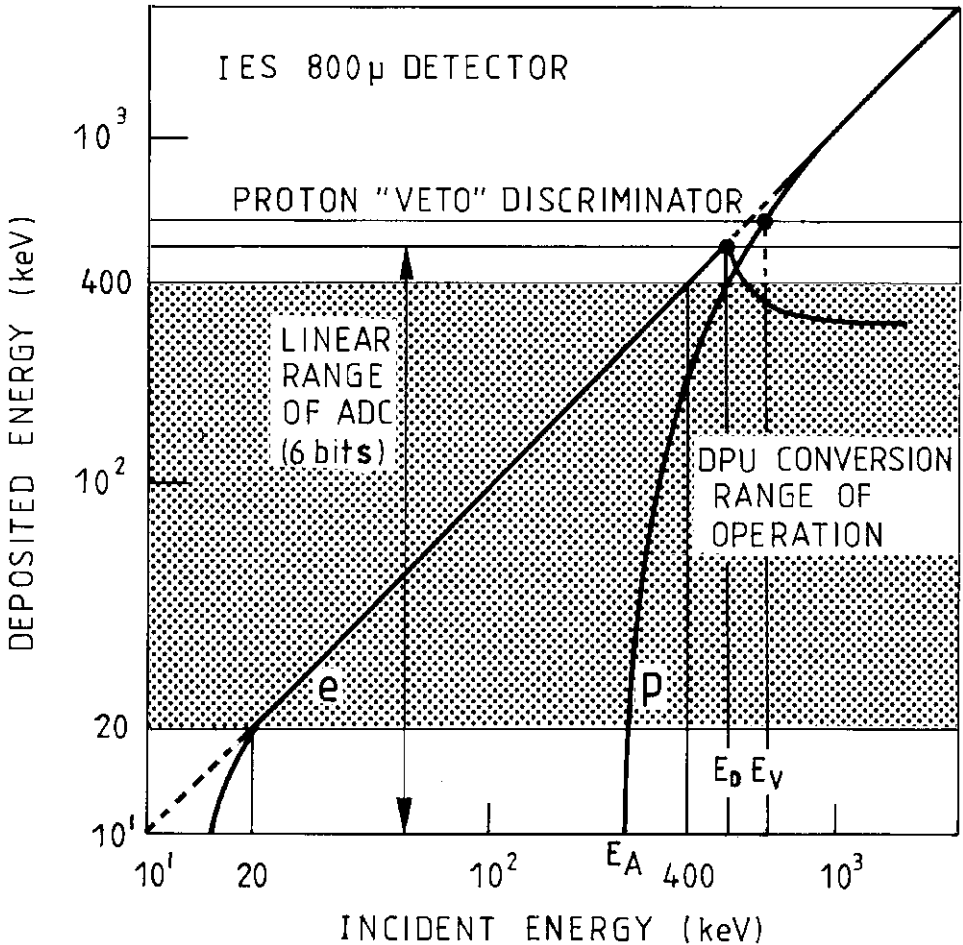
Figure 8. Energy range of the IES detector system. The shaded area indicates quasi-unique electron identification. An absorber in front of the detector transmits protons only for energies exceeding E_A. Electrons with energies above E_D and protons in the narrow energy and E_A onto E_V can confuse the electron measurement but the rather low intensity makes this background insignificant under all preactical conditions.

the Rutherford Appleton Laboratory, Oxford (UK)). Each pre-amplifier channel has typically a noise at zero input capacitance of 700 electrons r.m.s. equivalent to 6 keV Full-Width-at-Half-Maximum (FWHM). The total power consumed by the chip is about 10 mW.

According to Figure 10, the charge placed in the solid-state detector by an incident particle is stored on a capacitor (e.g., C2) following the pre-amplifier. This stored charge is compared to a background value stored in a companion capacitor (e.g., C1). The difference between these two values of charge is then strobed out and fed into a comparator for further evaluation (see Section 2.2.2).
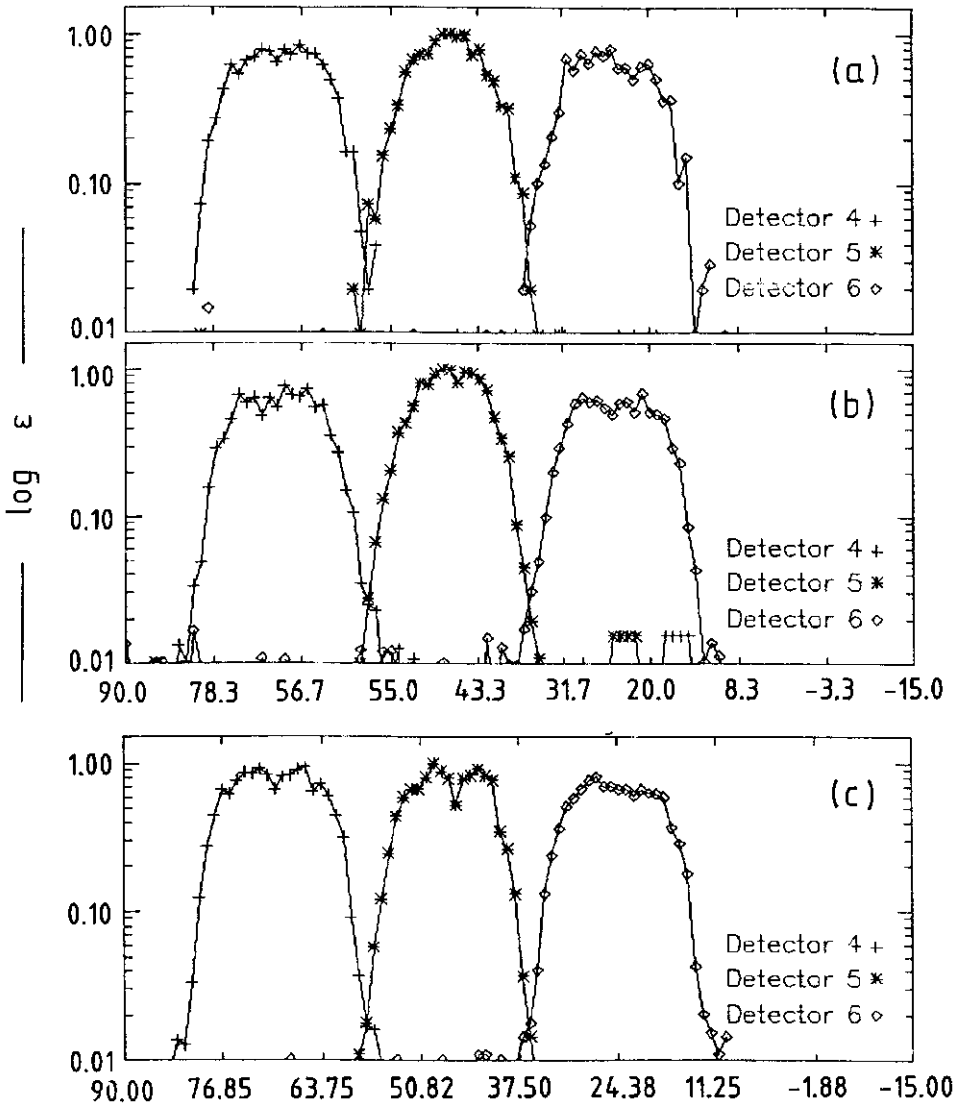
Figure 9. Angular response of an IES head with three detector strips. The panels (a), (b), and (c) show angular scans for 65, 90, and 114 keV electrons.

The SCVC chip operates the nine detector strips in a parallel/sequential fashion:

(1) At the time $t = 0$ all nine detector/charge sensitive pre-amplifier systems are activated for an integration time t_{int} (t_{int} can be set to 2 μs, 10 μs, 50 μs, and 100 μs).

(2) After closing the integration window, the nine channels are strobed-out in 47 μs (a 1–2 μs deadtime between the integration interval and the beginning of the read-out process is insignificant).
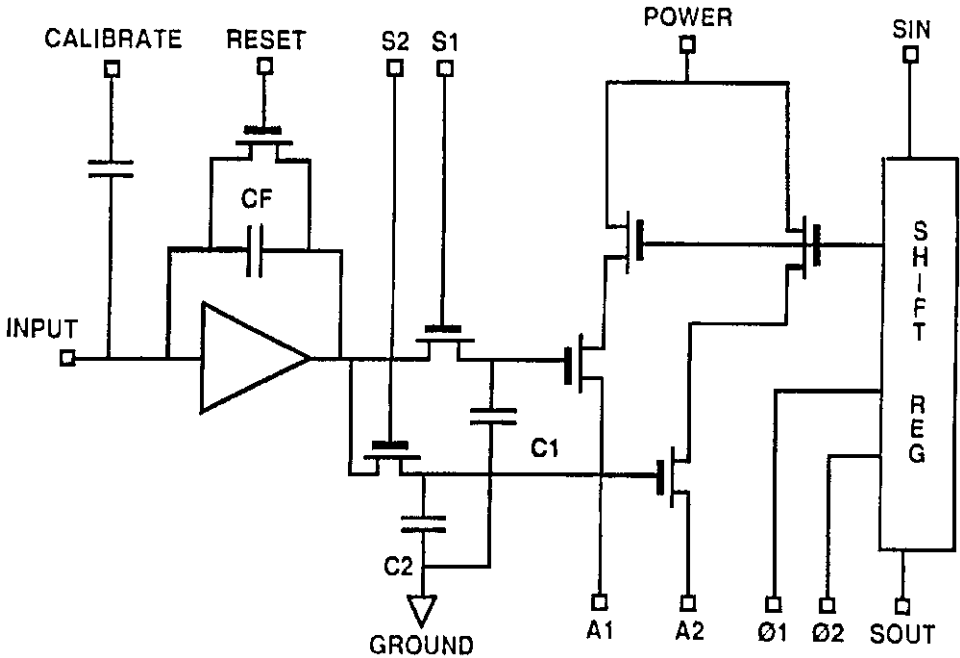
Figure 10. Schematic of the Switched Charge/Voltage Converter (SCVC) showing one of 16 identical channels. The switches S1 and S2 control the charging of the capacitors C1 and C2.

As a result the duty cycle of the system varies from 4% ($t_{int} = 2\ \mu s$) to 68% (for $t_{int} = 100\ \mu s$); the long integration times are particularly useful for low electron fluxes. Particle pile-up effects in the SCVC present a serious problem and, therefore, the actual counting rates have to be monitored carefully and the integration time t_{int} has to be adjusted according to the flux level. IES has the built-in feature to switch automatically to a shorter integration time t_{int} if the counting rate exceeds a certain limit. The limit value is set such that pile-up has a rather low probability.

The SCVC design principle leads to the existence of residual charge values at the entrance of the comparator. These offsets or 'pedestal' values are different for each channel but they are stable over time and temperature; the analysis of digitised charge values must correctly handle these pedestals. An example for the variation of pedestal values is given in Figure 11 for the flight unit RAPID-5: the pedestal positions for the nine detector strips, measured with the 8-bit ADC in the instrument, varies in the extreme by as much as a factor of 10 to 15. The impact of the pedestal value on instrument performance and data interpretation is discussed in Section 2.2.2.
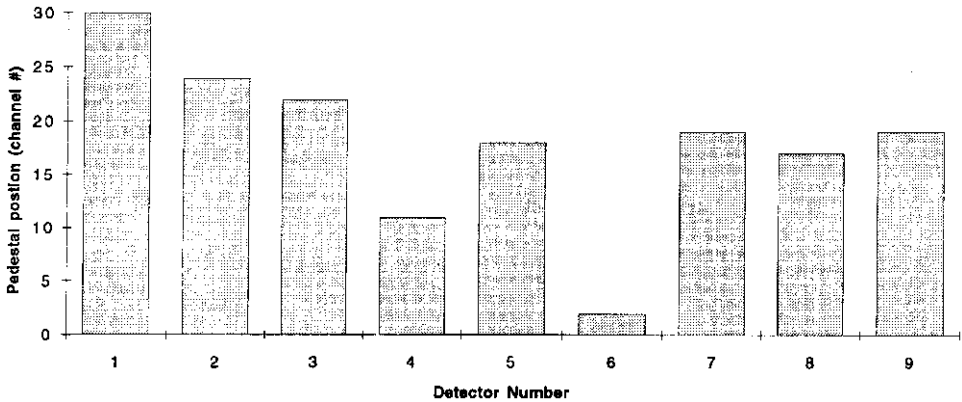
Figure 11. The mean pedestal positions of the 9 IES detector strips in the RAPID unit F5. The positions are given as channel numbers out of total of 256 CH.

2.2. SIGNAL-CONDITIONING UNITS (SCU)

The general lay-out of the RAPID instrument in Figure 2 shows that either of the two sensor systems is followed by dedicated circuitries called the Signal Conditioning Unit (SCU). The primary task of the SCU is to provide proper analogue amplification and signal shaping, event-definition logic, control functions for configuring the detector system and to interface with the Digital Processing Unit or DPU.

2.2.1. *The IIMS Signal-Conditioning Unit*

Figure 12(a) is a simplified representation of the IIMS Signal Conditioning Unit (SCU) which is intended to show essential components and their role in the complex signal generation and signal processing on different levels. An important task of the SCU is to ensure that signals generated in the IIMS sensor system are indeed caused by a single incident particle. Within limits the SCU detects and excludes events which involve two or more particles arriving at the sensor system within a defined time window. The following is a description of major electronic SCU components and the sequential signal-processing on different levels:

Level 0

A particle passing through a SCENIC head Sy is analysed with respect to its flight time T (or equivalently to its velocity), to its energy E and to its direction-of-incidence (DIR). Accordingly, the SCENIC head generates a set of signals (analogue and digital) in the energy, time and direction channels with the following definitions:
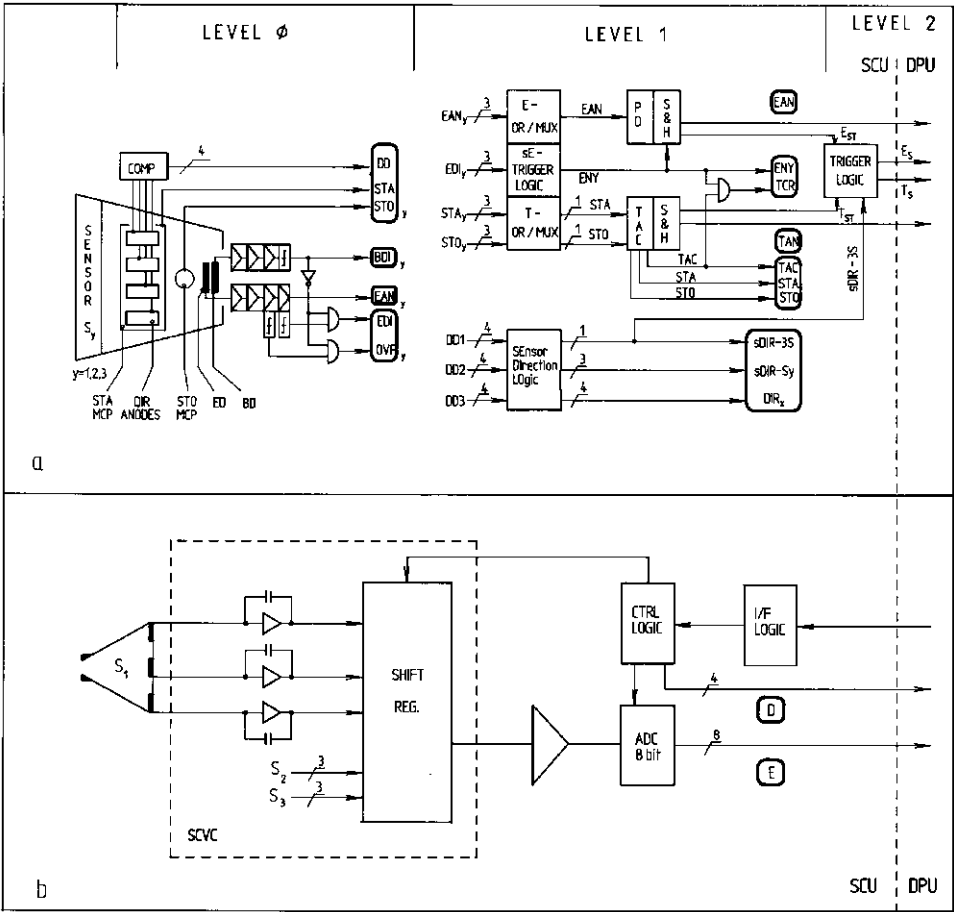
Figure 12. Simplified diagrams of (a) the IIMS and (b) IES signal conditioning units with emphasis on the signal and data formation (data are shown in heavy rounded rectangles).

CH	Signal	Definition
E	EAN	Analogue signal from the energy detector ED.
	EDI, OVF	Digital pulses from the lowest (A) and highest (C) thresholds in the ED amplifier chain.
		Overflow indicator.
	BDI	Digital pulse from the back detector BD,
		BDI inhibits EDI and OVF.
T	STA, STO	START and STOP signals.
DIR	DD	One-out-of-four direction signals.

The signal multiple (EAN, EDI, OVF, BDI, STA, STO, DD)y obtained from the head Sy represents an event at level 0. The subset (EAN, EDI, STA, STO,

DD)y is used for further processing in the SCU whereas the duple (BDI, OVF)y is transferred directly to scalers in the DPU.

Level 1

The signals (EAN, EDI, STA, STO, DD)y are offered to the next stage in the SCU for a first evaluation. As sketched in Figure 12 the analogue signals EANy and the time signals (STA, STO)y are connected to so-called OR/MUX devices for selection. The DPU can specify the sensor operation by setting the E and T multiplexer to the OR or MUX mode. In the OR mode signals are accepted on a first-come-first-served basis; in operational terms this mode is called Parallel Mode (PM). In the MUX mode sensors Sy are selected sequentially and only signals from a given sensor are accepted at any one time; in operational terms this mode is called Serial Mode (SM).

An analogue EANy signal in the E-channel is processed only if the digital EDIy meet some constraints. The EDIy signals are evaluated in the sE-TRIGGER LOGIC (sE stands for 'single EAN') to ensure that a single Sy sensor was active. The peak detector PD in the analogue path can operate on the EAN signal only if exactly one out of the three EDIy lines carries a pulse. If this condition is met sE-TRIGGER LOGIC creates an ENY pulse to indicate that the (EAN, EDI)y combination concurs with the above-mentioned requirements. In general, an EAN signal will not be accepted by the PD circuit if:

– its amplitude was below the lower threshold A (no EDI created);
– the particle energy was sufficiently high to stimulate the back detector BD and the resulting BDI signal disabled the EDI pulse;
– more than one EDI pulse was detected by the sE-TRIGGER LOGIC.

The T-OR/MUX circuit in the T-channel selects a (STA, STO) pair in a similar manner as the EAN signal is selected in the E-channel. The time-to-amplitude converter (TAC) transforms the pair into an analogue signal called TAN (T analogue) with an amplitude proportional to the observed flighttime T, and issues a digital TAC pulse to indicate the detection of a valid TAN signal.

In the DIR-channel a device marked SEDILO (Figure 12) converts the pulse pattern on the DDy lines (three times four lines) into signals and codes characterising the status and contents of the direction measurement:

(1) A sDIR-3S pulse is issued if only a single active x-direction was found in all three detector heads.
(2) The sDIR-Sy pulse defines the stimulated detector head Sy ($y = 1, 2, 3$).
(3) The DIR-x ($x = 1, 2, 3, 4$) code defines the four look-directions in Sy.

In summary the Level 1 processing leads to the following products: a new multiple of digital pulses (STA, STO, TAC, ENY) is established, reflecting that START and STOP pulses are selected and a valid TAN signal is produced; an EAN signal from a single detector is received and the sampling process in the Sample-and-Hold circuitry (S & H) is initiated. As indicated in Figure 12(a) ENY and TAC signals are combined to form a TCR pulse (functionally TCR is formed at this stage

but the logic is actually located in the DPU). This pulse proves that valid analogue energy (EAN) and time (TAN) signals are present. However, it is important to note that the compliance of the (EAN, TAN) pair with the trigger condition specified in the TRIGGER LOGIC has yet to be demonstrated in the Level 2 processing phase.

The DIR-channel has found a single direction, a corresponding (sDIR-3S) signal is created and the direction is characterised by the duple (sDIR-Sy, DIR-x) with the ranges $y = 1, 2, 3$ and $x = 1, 2, 3, 4$.

As discussed above, a particle's direction of incidence within $180°$ polar angle is defined by a coarse direction Sy (one of the three $60°$ SCENIC heads Sy) and a fine direction DIR-x (division of Sy in four $15°$ intervals). The coarse direction Sy can be obtained from three different channels: From the E-channel (EDI-Sy), from the DIR-channel (sDIR-Sy) and from the multiplexer system (E-, T-, DIR-MUX) by selecting a sensor head Sy. The fine direction DIR-x, on the other hand, is extracted only from the DIR-channels. Of particular interest is the susceptibility of this system to particle pile-up in the DIR-channel and its dependence on the sensor mode (parallel or serial):

Serial Mode

The DPU activates a single sensor head Sy at any given time and cycles through the sensor heads Sy ($y = 1, 2, 3$) in a preprogrammed sequence. A unique coarse direction y is therefore imposed for all events. A fine direction DIR-x will be issued by SEDILO only if the DDy code from the DIR-channel shows unambiguous direction information. Invalid DDy codes (two or more lines show high levels due to multi-particle interaction or charge splitting between read-out modes) disable SEDILO and the triple (sDIR-3S, sDIR-Sy, DIR-x) will not be generated. However, the DPU accepts the remaining digital signals for accumulation in COUNTER ARRAY but the classification is restricted to MTRX data as will be discussed in Section 2.3.1.

Parallel Mode

All three sensor heads are active and particles are accepted on a first-come-first serve basis. The direction of incidence (Sy, DIR-x as defined in Figure 20) is obtained from measured quantities only. The unbiased sensitivity over $180°$ makes this mode attractive in low flux environments but this advantage is increasingly qualified by the susceptibility to multi-particle events if the flux exceeds a certain critical level.

The response to ambiguous directional measurements can be presented in a convenient form by using the definitions:

– DDu(2): DIR-detector in sensor head Su shows two active anodes due to multiparticle interaction or charge splitting; the DIR-detectors from the other heads are assumed to be inactive;

– 2DD: DIR-detectors from two different heads, Su and Sv, show valid single directions; the third detector is assumed to be inactive;

– EDI-y: single (s) or multiple (m) y-directions active, and by referring to the DPU description in Section 2.3.1:

Sensor		SEDILO			DPU	
EDI-y	DDy	sDIR-3S	sDIR-Sy	DIR-x	Class.	CTR. array
s, m	DDu(2)	–	–	–	I-MTRX	Yes
s	valid	Yes	$\neq$EDI-Sy	Yes	no	Yes
s, m	2DD	–	sDIR-Su;v	–	no	Yes

Level 2

The digitisation of the EAN and TAN amplitudes in the analogue-to-digital converters (actually located in the DPU) depends on precise coincidence conditions. The circuitry TRIGGER LOGIC imposes commandable trigger modes and time windows on the event pattern (EAN, TAN, sDIR) with sDIR-3S abbreviated to sDIR:

Trigger mode	Accepted event type
1. $E + (T \star \text{sDIR})$	$(E, T, \text{sDIR}), (0, T, \text{sDIR})$
2. $E + T$	$(E, T), (E, 0), (0, T)$
3. $E \star T \star \text{sDIR}$	(E, T, sDIR)
4. $E \star T$	(E, T)
5. E	$(E, T), (E, 0)$
6. T	$(E, T), (0, T)$

The above trigger conditions lead obviously to a digital filter function with effects on the overall detection efficiency of the spectrometer. The following is a qualitative assessment of the filter effect:

– The triple coincidence required in Modes 1 and 3 has generally a rather low rate of occurrence. This is even amplified by the relatively low probability of creating a sDIR-3S pulse. As a result little practical value will be put on these modes.

– The double coincidence in Mode 2 has a reasonable efficiency but the accepted event structures have clearly a mixed distribution.

– The double coincidence in Mode 4 is lower in occurrence rate than Mode 2, but it creates clean distributions with acceptable efficiency. This mode is therefore the preferred operational mode.

– Modes 5 and 6 are implemented merely for the case of drastic failures in either the energy or the time channel.

The E- and T-ADC in the DPU start the conversion in binary codes if the analogue pair (EAN, TAN) meets the coincidence requirement set in TRIGGER
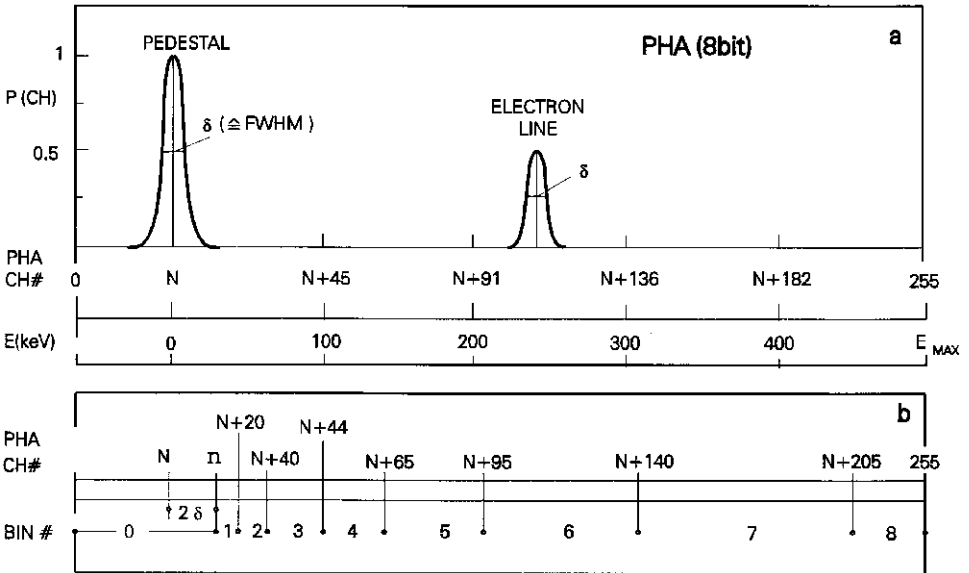
Figure 13. Principle of the pulse-height analysis for an IES detector strip/pre-amplifier channel. The pedestal distribution with the width δ reflects the variation of the minimum charge about its mean value at channel $= N$. If an incident electron deposits additional charge on the strip the pulse amplitude is found in channel $N + \Delta$ ('electron line'). The position of the pedestal ($CH = N$) corresponds therefore to the particle energy $E = 0$ keV. The lower part of the figure shows the prescription for mapping the 256 channels into 9 bins: a single pedestal bin ($b0$) and eight energy bins $b1$ to $b8$.

LOGIC and the event, now represented in an all-digital form, is ready for the classification process in the DPU.

2.2.2. *The IES Signal-Conditioning Unit*

Figure 12(b) deliniates the principal features of the IES signal conditioning unit (SCU). The initial amplifier stages for the nine energy channels and a multiplexer (comparator/shift register) are implemented in monolithic technology. This SCVC chip (see also Section 2.1.2) is physically integrated into the sensor housing. The second part of the SCU, designed with standard electronic components, accepts the serialised output signals from the chip for amplification in a single amplifier chain and subsequent digitisation in an 8-bit ADC. The resultant digitised signal represents the 'pulse height' or energy E of the incident particle.

More precisely, the measured signal amplitude corresponds either to the pedestal value (explained in Section 2.1.2) or to the pedestal-plus-energy value if a particle was detected. Figure 13 is an illustration of the peculiar effect of the pedestal on the electron energy range. The pulse amplitude offered to the 8-bit ADC is proportional to the charge found by the SCVC on the strip capacitor. However, there is always a minimum charge in the detector-pre-amplifier channel (pedestal) with a mean value, e.g., in ADC channel N, the fluctuations of this charge are characterised by

the FWHM (full width at half maximum) value δ. If a particle-related additional charge was present, the signal amplitude is shifted to a higher value called 'electron line' in Figure 13; this line has the same width δ as the pedestal distribution.

Two consequences are related to the existence of the pedestal:

(1) The total number of counts per time interval R found in the pulse-height distribution (obtained with a pulse-height analyser (PHA) is a constant. The value R is equal to the SCVC sampling frequency, i.e., a count is either found in the pedestal (no particle present) or in the appropriate ADC channel (particle energy E).

(2) In energy space the lower limit $E = 0$ keV is defined by the PHA channel N; the upper limit of the energy range is $E_{\max} = (255 - N)g$, with g denoting the system gain (nominally $g = 2.0$ keV CH^{-1}).

The conclusion from the above is that each single detector strip is associated with a specific energy range defined by its characteristic pedestal value N, a fact that has to be accounted for in the data analysis.

The output of the IES/SCU is a set of nine ADC values corresponding to the signal-plus-pedestal recorded since the previous readout. As indicated in Figure 12(b), each of the energy measurements is associated with a four-digit direction number D to form an (E, D) address pair for the information processing in the follow-on Electron Pre-Processor (EPP) in the DPU and accumulation by the microprocessor (see Section 2.3.2). This permits the DPU to handle the IES data at a sample time equivalent to strobing-out the SCVC channels.

As stressed in Section 2.1.2, the IES is a very compact sensor system. Because of this compactness, it has not been possible to monitor the system in the standard manner of electronic pulse stimulation through a charge terminator. Instead, the full system can be stimulated with a set of radioactive sources which produce a series of gamma- or X-ray lines in the 20 to 100 keV region. When a set of spectra is recorded from these sources, it is possible to verify the IES system performance very accurately, demonstrate the linearity of the amplifier gains, and observe the effect of the pedestal variation from channel-to-channel.

Figure 14 displays, as an example, the X-ray spectrum obtained from detector strip No. 2 in the RAPID flight unit F4 when a standard $_{63}$Eu^{155} source was mounted on the IES head. The radioactive source emits a series of X-ray lines with energies at 18.9, 26.5, 45.3, 60.0, 86.5, and 105.3 keV. The distribution in Figure 14 shows clearly a very strong peak at the pedestal position (PO) and peaks (P1 to P4) for the four most intensive X-ray lines. A fitting routine with gaussians allows the extraction of the characteristic values of the peaks (position and width). The obtained channel numbers, when referenced to the pedestal position, correspond to the X-ray lines at 45.3, 60.0, 86.5, and 105.3 keV. The FWHM (full width at half maximum) values, which should be equal for all lines, reflect the noise in the selected detector strip No. 2 (the obvious variation in the FWHM values is probably due to the fitting procedure). The line positions allow a very accurate check of the system linearity and slope (equivalent to the gain factor g in keV CH^{-1})

RAPID IES f4 − 2 microseconds − Strip # 2
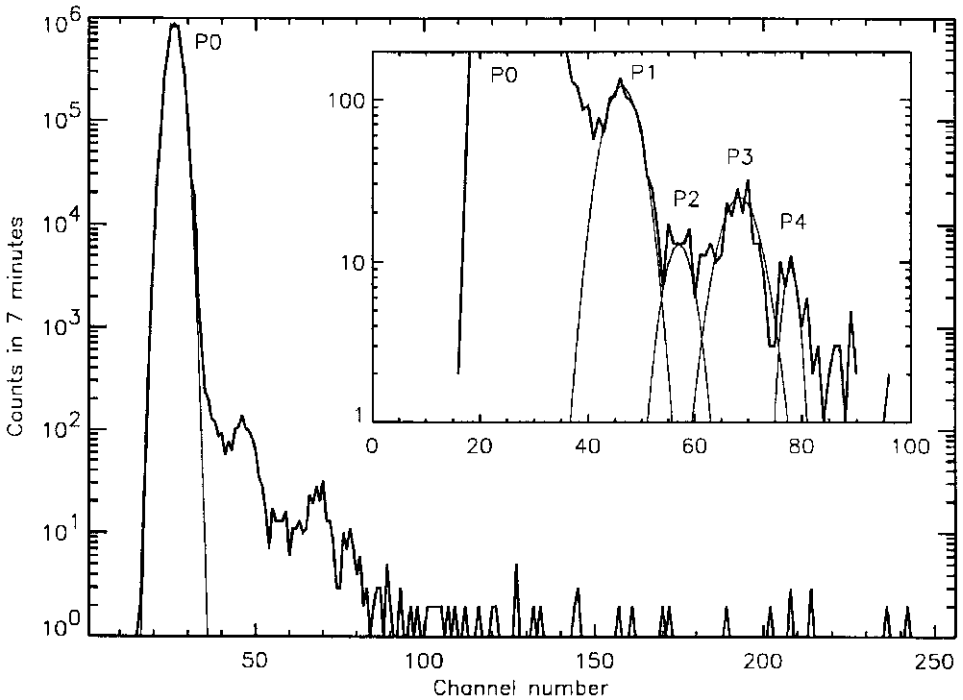
Figure 14. X-ray spectrum from an EU[155] radioactive source obtained with detector strip number 2 in the RAPID unit F4 (integration time 2 μs). The peaks P0 through P4 correspond to the pedestal and four X-ray lines at 45 keV, 60 keV, 80 keV, and 105 keV.

as demonstrated in Figure 15. This test and verification concept with a radioactive source as an external stimuli has the obvious advantage of providing truly front-to-end information with no electronic interference. The shortfall, on the other hand, is that the source can only be used for ground tests, in-orbit IES has rather limited test capabilities.

2.3. THE DIGITAL PROCESSING UNIT (DPU)

The internal digital processing unit (RAPID-DPU) serves the SCUs and sensor systems (IIMS and IES), evaluates and compresses the primary event data rate to a level which is compatible with the telemetry capacity and arranges the output data in the format of an Experiment Data Block (EDB). The present description of the DPU and its functions is a rather brief extract with strong emphasis on the data manipulation and the final construction of 'Science Data'.

   The simplified DPU block diagram in Figure 16 amplifies the following key elements:
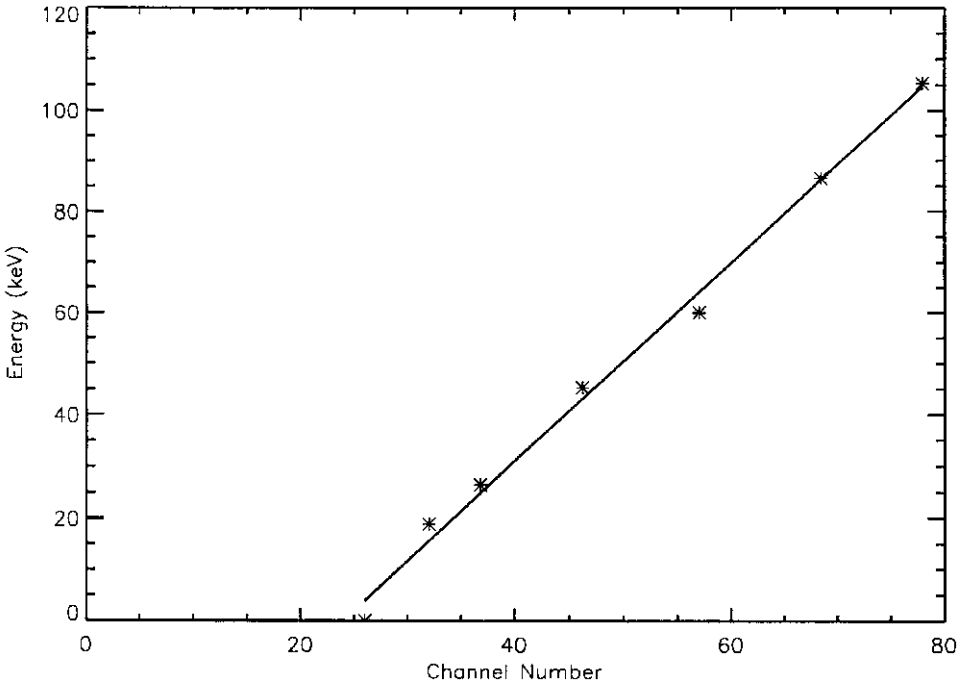
Figure 15. Energy versus channel plot produced from the pedestal and x-line positions in Figure 14. This technique monitors the channel gain (slope of the straight line) and linearity.
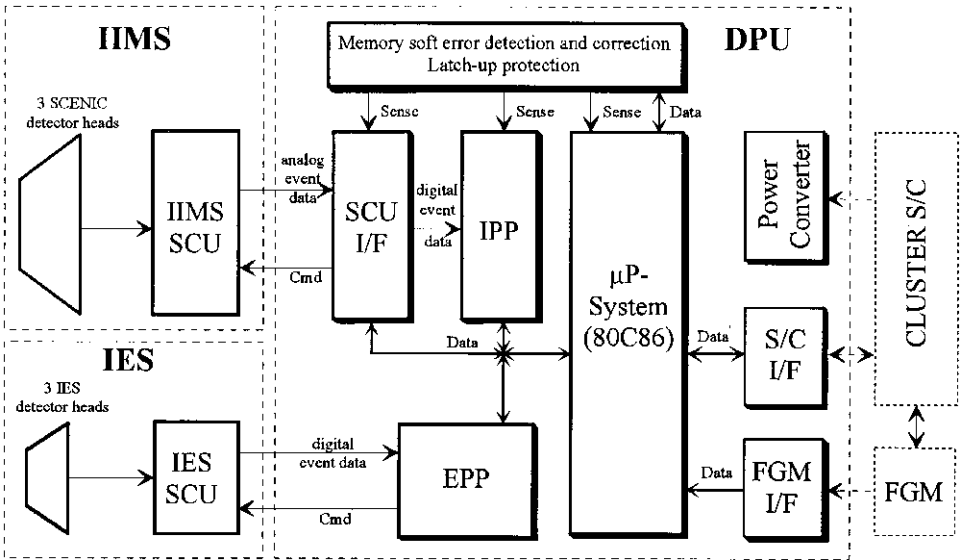

Figure 16. Block diagram of the RAPID digital processing unit (DPU) and the interfaces to the sensors, the spacecraft, and the magnetometer (FGM).

 – Interface to the IIMS SCU.
 – Ion Pre-Processor (IPP).
 – Electron Pre-Processor (EPP).
 – Microprocessor system (80C86-based).
 – Memory protection and latch-up detection safeguard electronics.
 – Interface to the Cluster spacecraft.
 – Inter-experiment-link (IEL) to the magnetometer instrument (FGM).
 – Low-voltage power converter.

2.3.1. *IIMS Event Processing*

A main task of the DPU is the compression of the enormous quantity of data received from the IIMS/SCU system. It was mentioned in the previous section that each fully defined particle event is described by two analogue signals (EAN, TAN) and a set of 18 digital pulse channels. These data are processed in the DPU and eventually transformed into 'Science Data' for nuclei. The various data types created in the SCU on the different levels of processing are transferred to the DPU as schematically shown in Figure 17. The multitude of IIMS signal channels, shown on the left side of Figure 17, is divided into three groups. The first group includes the 18 digital pulse channels. A subset (TAC, EDI-y, sDIR-Sy, DIR-x) is passed through a logic to expand the TAC and EDI-y pulses into channels with higher directional resolution. This process leads to pulse types of the form TAC-y, TAC-yx and EDI-yx. These pulses and the set (STA, STO, BDI-y, OVF-y, ENY, sDIR-3S) are offered to COUNTER ARRAY (Figure 17) to increment appropriate scalers.

The second group is essentially a duplication of direction relevant information from the DIR- and E-channels (sDIR-Sy, sDIR-3S, DIR-x, EDI-y) and the overflow indicator OVF-y. This subset is used for consistency checks in a precursing process before the analogue signals EAN and TAN in the third group are accepted for digitisation and classification. Events showing overflow in the energy channel ($E \geq 4$ MeV) and/or inconsistent direction information in EDI-y and sDIR-Sy are discarded. For all other events the two ADCs can be enabled by the trigger signals Es and Ts. At the same time the DPU processes the event-related direction information (sDIR-Sy, DIR-x) and synchronises it with the digitised (E, T) pair to remove dynamic phase shifts. The DPU also converts the SCU direction code (Sy, DIR-x) into a serial number $D = 0, \ldots, 11$ which defines twelve unique directions within the $180°$ polar range of the instrument with the counting convention specified in Section 2.5.1. (Figure 20). In case the sDIR-3S pulse fails to indicate the presence of a high resolution directional measurement (positive identification of a single direction out of the 12 polar angular intervals) the DPU determines a coarse y direction from the EDI-y pattern and assigns to these the direction numbers $D = 12, 13, 14$ (inspect Figure 20 for the counting convention).

The event (E, T, D) is now prepared for the classification process in the follow-on ion pre-processor or IPP in Figure 18. The objective is to extract from the (E, T)
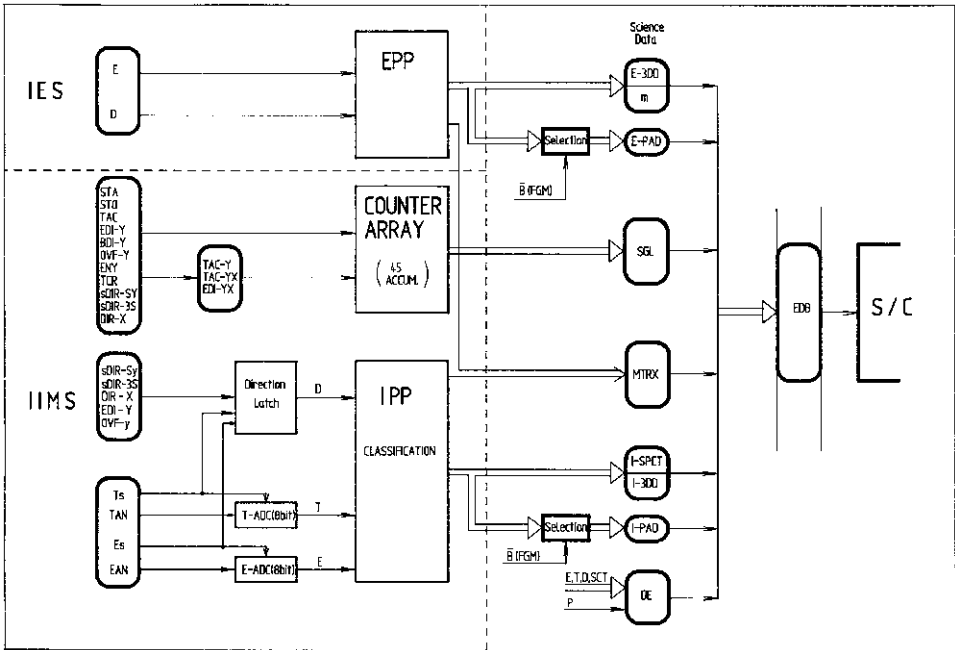
Figure 17. Schematic representation of the data processing in the DPU. Input data from the SCUs are shown on the left (heavy rounded rectangles). The sorting and classification processes eventually result in the Science Data which, in turn, are organised in Experiment Data Blocks (EDB) for transmission. The vertical dashed line separates the Micro-Processor supported data evaluation (right side) from the hardware logic and the pre-processing systems EPP (Electron Pre-Processor) and IPP (Ion Pre-Processor).

pair the particle mass A and the energy per mass ratio E/A with high precision. In addition the $A - (E/A)$ space is subdivided into a coarse bin field which is then combined with high-resolution direction information. This leads to a substantial reduction in the required data rate without the necessity to reduce resolution in time and direction.

The DPU initiates the classification process upon the appearance of at least one of the trigger signals Es and Ts (compare Figure 12(a)). The E/A ratio is established in a straightforward single table look-up technique, since this quantity is obtained from the measured flighttime T directly. The particle mass A, on the other hand, depends on energy E and flighttime T. A five-step successive approximation in an $E = f(T, A)$-table is applied to obtain the mass A. This process can handle a maximum event rate of roughly 50 000 s^{-1}.

The final product of the classification is the construction of high-resolution $(A, E/A)$ vectors which are used to address:

(1) a (32×64) matrix counter field and

(2) a bin-definition field.
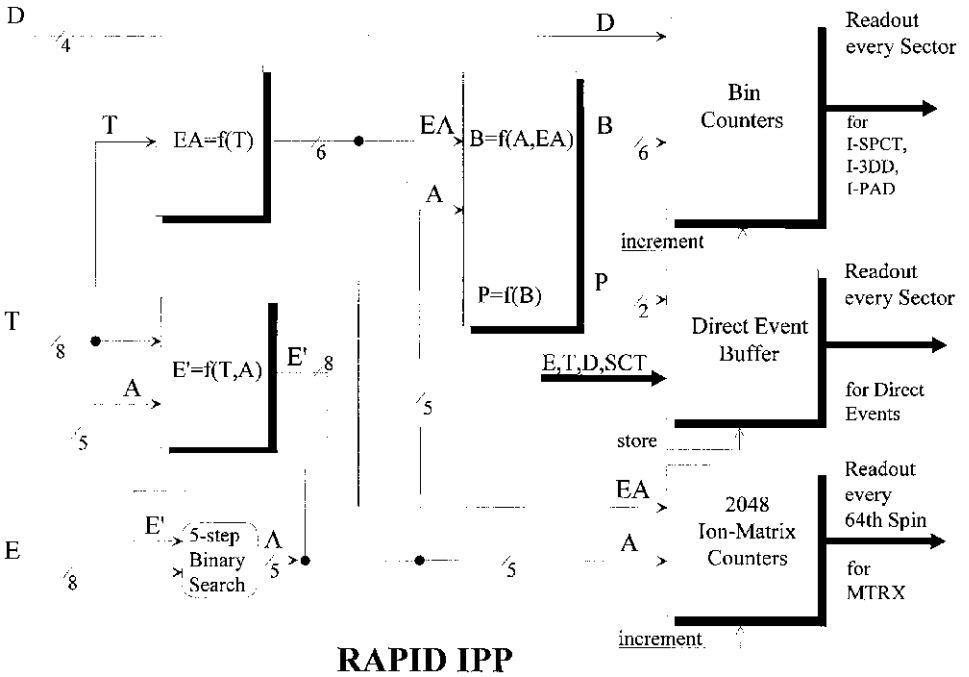
Figure 18. Schematic diagram of the ion pre-processor IPP showing the data flow in the classification process.

The selected matrix counters are incremented, the contents of this counter field represents the IIMS part of the 'Science Data' MTRX. The output of the bin-definition field is a bin number B which defines 35 bins in the $(A - (E/A))$ plane. The bin number, combined with the direction number D, addresses the bin counter array and the respective bin counter is incremented. The contents of the bin counter array is the basis for the 'Science Data' I-SPCT, I-PAD, and I-3DD described in Section 2.4. This process reduces the $(A - (E/A))$-matrix from a total of 2048 to 35 elements which cover the same area in $(A - (E/A))$ space with a coarser resolution.

The above description of the classification process refers essentially to (E, T, D) events with valid values for all three parameters. Events with missing parameters are processed according to the following scheme (missing parameters are shown as 0):

E	T	D	Classification
0	T	D	yes
E	0	D	no
E	T	0	MTRX only
0	T	0	MTRX only
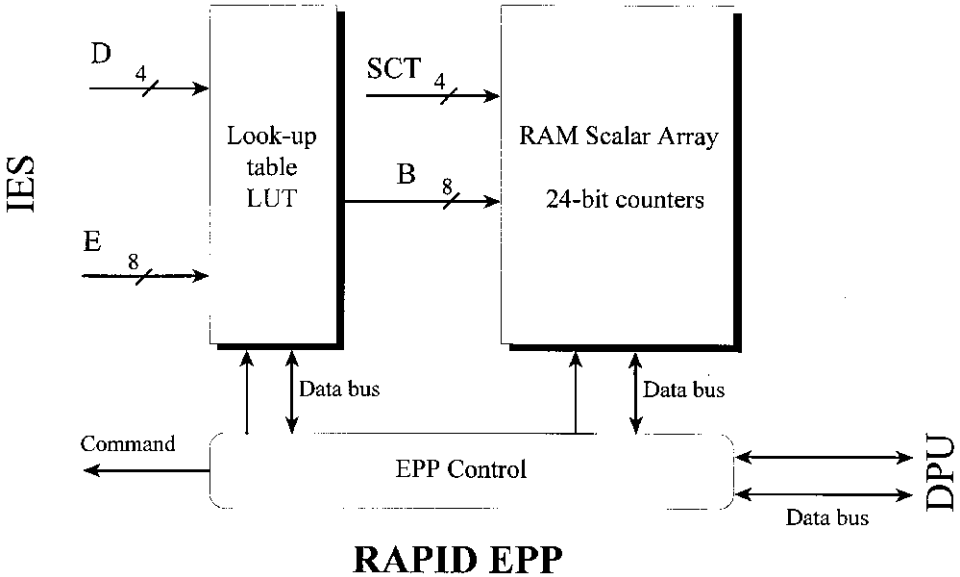
Figure 19. Schematic diagram of the electron pre-processor (EPP). Electron input data (energy E and direction number D) are passed through a sorting process to reduce the data volume.

2.3.2. *Electron Pre-Processor (EPP)*

According to Figure 17 signals from the IES /SCU are transferred to the Electron Pre-Processor (EPP) in the DPU. The EPP tasks are the provision of a serial command interface to IES and the pre-processing of IES event data. A simplified block diagram of the electron pre-processor is presented in Figure 19. A valid electron event at the EPP input is described by a digital signal duple (E, D), with E (8 bit) and D (4 bit) denoting the electron's energy and direction of incidence, respectively. The (E, D) pair serves as an input vector for a bin definition look-up table (LUT) which defines a bin number B (8 bit). The bin number B and the current sector number SCT (SCT defines 16 azimuthal sectors) are concatenated to form another vector pointing to a RAM SCALER field (a RAM-based counter array) and the selected counter is then incremented. The contents of the RAM SCALER serves as the basis for the generation of the electron Science Data E-3DD and E-PAD. These data types, with reduced binning in energy space (8 bins and 2 bins, respectively) form by far the most important data for routine operation in-orbit.

As mentioned earlier, the IES SCU uses a 256-channel pulse-height-analyser or PHA (the PHA consists of an 8-bit ADC and the associated RAM scaler field which stores the pulse-height distribution). The limited telemetry capacity requires information reduction by mapping the original 256 PHA channels to 8 energy bins (or 2 bins for E-PAD). The principle of the bin-mapping concept is illustrated in Figure 13(b) for E-3DD (8 bins). The bin boundaries b are referenced to the

pedestal position ($CH = N$ corresponding to $E = 0$ keV) by using the algorithm $b = (N + ch)$, with $ch = 20$–205, etc., denoting predefined fixed channels as shown in Figure 13. The seven boundaries $b = (N + 20)$ to $b = (N + 205)$ define six energy bins ($b2$ to $b7$) with a quasi-logarithmical increase in width. These bins move obviously in 'channel space' but they are fixed in energy space (!) since they are referenced to the pedestal position N ($E = 0$ keV).

However, inspection of Figure 13(b) reveals:

(1) The width of the first bin ($b1$) is defined by the system noise δ: $\Delta(b1) = (20 - 2\delta)$. This follows from the prescription for the lower boundary n of $b1$: $n = (N + 2\delta)$.

(2) The width of the last bin ($b8$) is defined by the pedestal position N: $\Delta(b8) = (50 - N)$.

As illustrated in Figure 13(a), the channel boundaries can be recast in energy space by applying the mean value $g = 2.0$ keV channel^{-1} for the system gain factor (the variation of g for the nine detector strips is no more than $\pm 5\%$).

Actually the above mapping process creates a total of 9 bins in energy space:

– Bin 0 (between ch 0 and ch $n = (N + 2\delta)$ contains the vast majority of the pedestal counts plus counts of the energy spectrum between $E = 0$ keV and $E = (2\delta g)$ keV. The counts in this bin are transmitted in the housekeeping data (HK-data). Bin 0 monitors in essence the pedestal count rate and allows a judgement on the performance of the read-out system for the channel in question.

– Bin 1 through 8 form the 8 energy bins used in the Science Data for E-3DD (the two energy bins for E-PAD are generated in the same spirit), they are essentially free of noise counts from the pedestal distribution. An accurate knowledge of the pedestal position N and noise width δ is required for the channel-to-energy transformation.

The DPU constructs the bin boundaries in the 256-channel-to-8-bin mapping process from look-up tables (LUTs). This implies the following steps:

(1) The LUT for a given IES unit (with nine detector strips) contains pairs $(Nn, \delta n)$, with $n = 1$–9, describing the pedestals for the nine detector strips and the values of 7 fixed bin boundaries. From this, as delineated above, the DPU computes the 9 bin boundaries required for the description of the 'pedestal bin' bin 0 and the 8 energy bins (bin 1 to bin 8). Since the noise values δn are dependent on temperature T and integration time t_{int} ($t_{\text{int}} = 2, 10, 50, 100 \, \mu s$) some fine tuning is necessary. Therefore a quadruple of LUTs (representing the four integration times t_{int}) is used for each of the two expected operational temperatures $T = -10 \, °C$ and $T = +20 \, °C$. This amounts to a total of 8 LUTs for a given IES unit.

(2) To increase the operational flexibility each RAPID DPU stores the LUTs of all five flight units (including the spare unit), i.e., each DPU can choose from a total of 40 LUTs.

(3) The compressed format of the 40 LUTs (described in (1)) is stored in a ROM. During commissioning or at certain phases along the operational orbit a LUT quadruple which is appropriate for the IES unit of interest and the temperature T

is selected by telecommand (TCMD). This quadruple is then copied into the non-volantile RAM (NVRAM). At this stage some editing of the $(Nn, \delta n)$ values is possible. In a next step the LUT quadruple is decompressed to generate a quadruple with explicit bin boundaries stored in the NVRAM. With a final TCMD the LUT with the optimum t_{int} is selected from the quadruple, fully expanded, and written into the EPP memory (the selected rad-hard memory components have very low SEU susceptibility; periodic reloading of the EPP memory limits the duration of corruption potential of IES measurements to fractions of an orbit). It is possible to combine the selected optimum choice LUT with a different value for the integration time t_{int} if this leads to better results.

The bin defining LUTs can be exchanged by telecommand thus allowing arbitrary schemes for binning the energy (E) and direction (D) ranges. A set of pre-defined LUTs is permanently available in the DPU. From either these resident LUTs or from up-linked new tables the DPU generates the electron Science Data (consult Table III for definitions):

(1) E-3DD (8 energy bins), E-PAD (2 energy bins) and the detector index m;

(2) Histogram mode (256 energy bins); this is not a routine mode.

Look-up tables are dedicated to either group (1) or group (2). This implies that, in contrast to IIMS, the two groups are mutually exclusive since only a single LUT is active at any given time. A set of about 16 different LUTs is required to cover the entire range in energy and direction for the high-resolution data in group (2).

2.3.3. *On-Board Pitch-Angle Computation*

The RAPID spectrometer is connected to the magnetic-field instrument FGM via the Inter-Experiment Link (IEL). FGM sends 64 uncorrected magnetic-field vectors $\mathbf{B} = (B_x, B_y, B_z)$ per spacecraft rotation ($T = 4$ s). Vector components are offered in digital form with a width of 12 bits each. The objective is to determine for each of the 16 azimuthal sectors which look direction in the IIMS and IES fan, respectively, is perpendicular to the $\mathbf{B}$-vector (the DPU uses the second $\mathbf{B}$-vector received in a given sector as the reference vector).

The DPU implements this $90°$ pitch-angle determination by applying the following algorithm in each sector: Unit vectors $\mathbf{D}_\nu$, ($\nu = 0, \ldots, 11$ for IIMS and $\nu = 0, \ldots, 8$ for IES) are introduced to describe the boresights of the detector look directions. A software routine calculates the 12 (9) vector products $(\mathbf{D}_\nu \cdot \mathbf{B})$ and determines the vector $\mathbf{D}_n$ for which the product assumes a minimum value, i.e., the direction $\mathbf{D}_n$ corresponds to $90°$ pitch angle. For each $\mathbf{D}_n$ the DPU assigns by means of a look up table two D_ν corresponding to look directions closest to the magnetic field direction (parallel and antiparallel). The number of events accumulated with these direction numbers form the I-PAD (E-PAD) Science Data.

2.4. THE IIMS AND IES SCIENCE DATA

The final data products resulting from the DPU are called 'Science Data'. According to Figure 17 the main body of the Science Data contains ion data (I-SPCT, I-PAD, I-3DD), electron data (E-PAD, E-3DD) and MTRX data. Each one of these data types is obtained from the classification process in IPP and the bin sorting in EPP. Four additional types of Science Data are provided:

– SGL-Data (IIMS): the DPU samples the 45 accumulators in COUNTER ARRAY with specified frequencies and forms single parameter rates called SGL-Data.

– DE-Data (IIMS): a fraction of unprocessed socalled direct events (DE) is selected to bypass the classification for transmission to the ground. A DE event is characterised by the 3 parameters (E, T, D) denoting energy (8 bit), time-of-flight (8 bit), and direction (4 bit). The selection of DE events is based on a four-step priority P which is assigned to the bin number B (see Figure 18). The P assignment can be changed by telecommand; default is $P = $ const. for all bin numbers B of a given particle species. Priority $P = 3$ refers to high-priority particles. With this definition priorities are assigned as follows:

Priority P	0	1	2	3
Species		e, p	He	CNO	Si-group

A maximum of 16 DEs per priority is accepted in each of the 16 azimuthal sectors on a first-come-first-served basis and written into a $(4 \times 16 \times 16)$ event buffer. Events are selected for addition to an EDB by applying the following prescription:

(a) At any given time the four least significant bits of the spin counter (INDEX) designate an azimuthal sector with the sector number SCT_n ($\mathrm{SCT}_n = $ INDEX MOD 16).

(b) The DPU starts the transmission in sector SCT_n by reading out the contents with decreasing priority $P\mu$ ($\mu = 3, 2, 1, 0$); the DPU sequences through the sectors until the number of events equals the maximum number S allowed per EDB. More precisely this can be written as:

$$\sum_{\nu=\mathrm{SCT}_n}^{\mathrm{SCT}_n+15} \sum_{\mu=3}^{0} P_\mu(\nu \bmod 16) \leq S$$

with $P\mu$ designating the number of events per priority P and sector ($P\mu \leq 16$); the total number of DE events S per EDB is given in Table IV. At this stage a DE event is represented by ($E = 8$ bit, $D = 4$ bit, SCT $= 4$ bit).

– Detector index m (IIMS and IES): defines for each sector the direction perpendicular to the magnetic field vector ($m = 0$–15). The directions in I-PAD and E-PAD are determined from tables with 'm' as the input parameter.

– **B**-vector polarity m-signs (IIMS and IES): indicates the polarity of the **B**-field in each sector.

Definitions of the Science Data together with a brief scientific description are given in Table III. It should be noted that RAPID/IIMS generates the same Science Data in energetic neutral atom (ENA) mode as in the ion mode.

The energy channels in Table III ($8d$ and $2w$) represent a contiguous coverage of the complete energy range for a given species. A precise position of the channel boundaries result from beam calibrations and will be compiled in the RAPID Data Analysis Reference Document (DARD) together with other calibration data.

The DPU samples the above data types and constructs an Experiment Data Block (EDB) as the basic unit for the data transmission to the ground. The EDB period $T = 4$ s is defined by the spacecraft telemetry system, however, the data structure varies with the telemetry mode. Tables IV(a) and IV(b) show the distribution of the Science Data in an EDB for the nominal (NM1 to NM3) and burst mode (BM1 and BM2) telemetry.

The principle difference between NM EDBs and BM EDBs is the higher sampling rate in the BM mode except for the electron data E-PAD and E-3DD. The former is omitted from the BM EDB because the pitch-angle distribution can be computed on the ground from the E-3DD distribution which covers the sphere with high angular resolution. The E-3DD data in NM mode are integrated over a spin whereas these data are subdevided in 16 assimuthal sectors in BM mode.

The socalled single rates SGL-0, SGL-1, SGL-2, and SGL-3 represent groups of counting channels from IIMS:

(a) One-dimensional parameter counters such as STOP rates and rates from the energy detectors.

(b) Two-dimensional parameters such as time-of-flight event rates (TAC), direction resolved rates from the energy detectors.

(c) Three-dimensional parameters such as time-of-flight/energy event rates (TCR) and direction-resolved TAC rates.

The frequency of transmission of a given SGL rate reflects the importance for the data analysis.

2.4.1. *Scratch Memory and Telemetry Mode BM3*

RAPID features a 64 kByte scratch memory which is organised as a ring buffer. It is used to collect BM1 mode EDBs as described in Table IV(b) in a continuous fashion. Upon the appearance of a trigger signal provided by the magnetic field instrument (FGM) via the IEL (Section 2.3.3) the instrument continous to collect data for one half of the ring buffer size. In this way the buffer captures high resolution data symmetric about the time at which the trigger pulse was issued. The total contens of the buffer corresponds to an observation time of approximately 2 min.

Table III
The RAPID science data

Data type	Particle species	No. of E-ch.	Polar intervals	Azimuthal sectors	Scientific description
H-SPCT	H	8 d	i	i	Proton energy spectrum
I-SPCT	He, CNO	8 d	i	i	He, CNO energy spectra
I-PAD	H	2 w	$3 \times 15°$	16	Selected pitch-angles ($0°$, $90°$, $180°$)
I-3DD	H, He, CNO	8 d	$12 \times 15°$	16	3D distribution
MTRX	all	all	i	i	$(A - (E/A))$ distribution
E-PAD	Electrons	2 w	$3 \times 20°$	16	Selected pitch-angles ($0°$, $90°$, $180°$)
E-3DD(NM)	Electrons	8 d	$9 \times 20°$	i	3D distribution, 9 pixels
E-3DD(BM)	Electrons	8 d	$9 \times 20°$	16	3D distribution, 144 pixels
m	all	–	–	16	Detector index
m-signs	all	–	–	16	**B**-vector polarity
DE	all	256	max $12 \times 15°$	16	High resolution direct events
SGL	na	na	na	variable	Digital pulse rates

d = narrow differential energy channels, w = wide-energy channels, i = integral

The BM1 EDBs read into the ring buffer are protected by check bytes appended to the EDB. Transmission to the ground is performed exclusively in telemetry mode BM3.

2.4.2. *Housekeeping Data and In-Flight Calibration*

Finally, it should be noted without details that SCU and DPU also provide valuable information in two other data fields which support the interpretation of the Science Data in a significant way. The first set comprises analogue and digital housekeeping data which reflect the actual operational configuration of the instrument and the health of all subsystems in an engineering sense. These data are transmitted in a dedicated telemetry channel. The second data set comes from the IIMS built-in precision pulse generator used to monitor and characterise the performance of the IIMS/SCU and, to some extent, of the DPU as well. The calibrator system operates in two different modes:

– The In-Flight Particle Simulator (IFPS): a calibrating (E, T) pulse pair is injected into the front-end electronics of the SCU once per spin and with a fixed phase. The DPU varies the pulse amplitudes by cycling through a pre-programmed sequence which simulates particle events such that an even coverage in $(A - (E/A))$ space is achieved. The IFPS is permanently active and cannot be switched off. A comparison of the simulated event pattern with the image returned to the DPU reveals irregularities in the analogue and digital signal processing. IFPS results are transmitted with full resolution in a dedicated area of the EDB (not included in Table IV) and contribute to science data I-SPCT, MTRX and SGL rates.

– The In-Flight Functional Test (IFFT): this routine must be initiated by tele-command; the instrument resumes the pre-test operational mode automatically after completing the test . The IFFT monitors threshold positions and amplifier linearity in the SCU. It should be noted that the transmission of science data is incomplete during execution of the IFFT test routine.

2.5. FLIGHT OPERATIONS

2.5.1. *Coverage in Phase Space*

RAPID is mounted on the spacecraft platform such that the field-of-view covers a range of 180° in the polar direction of a spherical system defined by the satellite's spin vector and spin plane. The sensor systems, IIMS and IES, scan the full range of the solid angle as the satellite rotates (16 azimuthal sectors). The data returned are used to construct intensity distributions of distant particle sources on a spherical or plane image area with 192 pixels for IIMS and 144 pixels for IES. Figure 20 shows the orientation of the instrument in the spacecraft reference system, defines the IIMS and IES look directions, and indicates the convention for the direction numbers D.
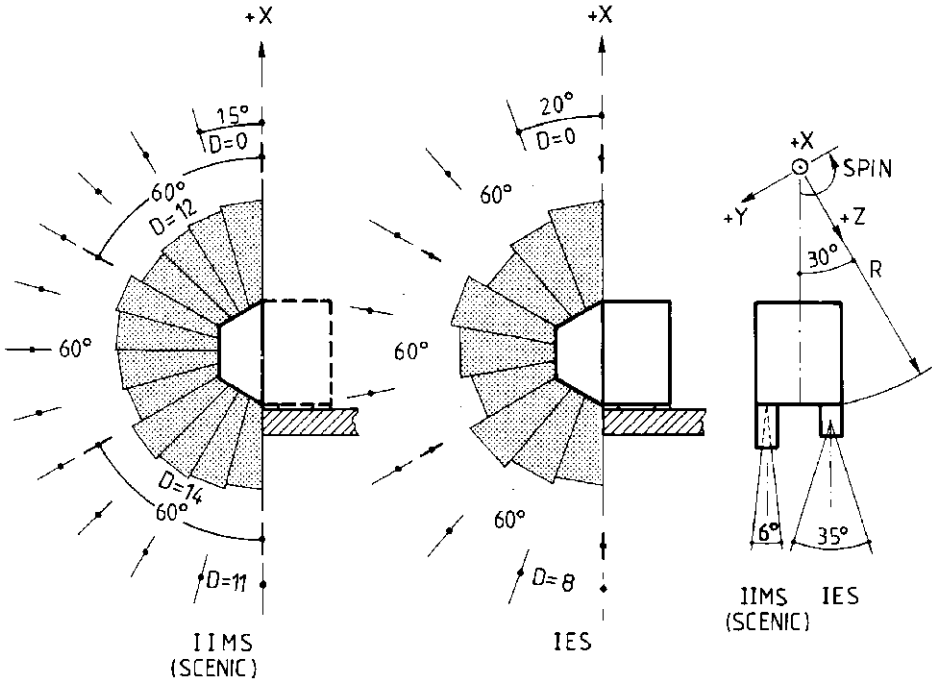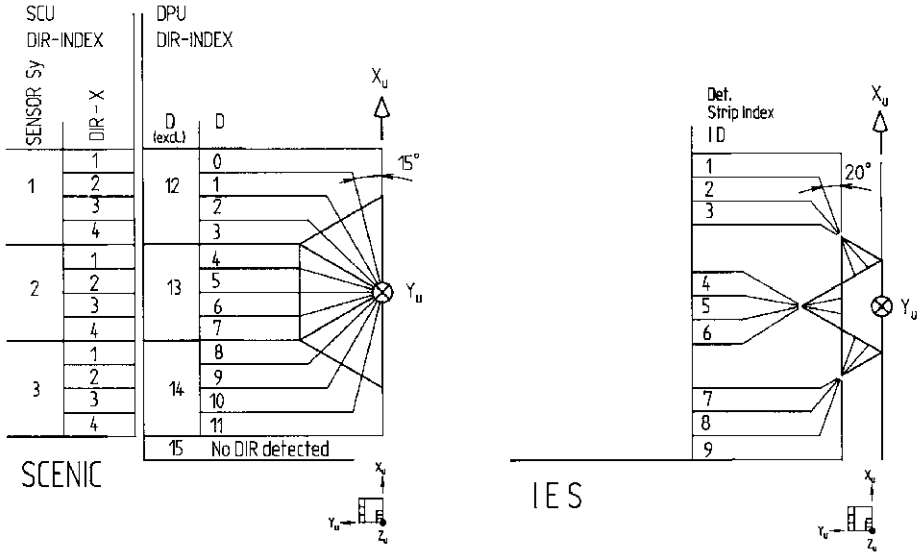
Figure 20. Orientation of RAPID on the Cluster spacecraft. The convention for the direction numbers D is shown for the two sensor systems.

Table IV(a)

Distribution of the science data in an EDB (1024.8 bit s^{-1}) (Telemetry modes: NM1, NM2, NM3, and BM2); Telemetry rate: 1024.8 bit s^{-1}

Science data	M–CH	E–CH	D–CH	Bytes per set	Bytes/ spin	Acc. period (spins)	Transfer time (spins)	Duty cycle
DE 20 ions, 3 bytes each	–	–	–	60	60	1	1	100%
SGL-0 (2 counters)	–	–	–	4	1	4	4	100%
SGL-1 (3 counters)	–	–	–	3	1	4	4	100%
SGL-2 (18 counters)	–	–	–	18	3	4	8	50%
SGL-3 (22 counters)	–	–	–	22	1	4	32	12.5%
H-SPCT	1	8	–	8	8	1	1	100%
I-SPCT	2	8	–	16	4	4	4	100%
I-PAD	1	2	3	6	96	$\frac{1}{16}$ [b]	1	100%
I-3DD	3	8	12	288	144	$\frac{1}{16}$ [b]	3 2	3%
I-MTRX	32	64	–	2048	8	64	256	25%
E-PAD	–	2	3	6	96	$\frac{1}{16}$ [b]	1	100%
E-3DD(NM)	–	8	9	72	72	1	1	100%
m	–	–	–	$\frac{1}{2}$	8	$\frac{1}{16}$	1	100%
m-signs	–	–	–	$\frac{1}{8}$	2	$\frac{1}{16}$	1	100%
Sync marker				3	3	–	1	
Subcommutation INDEX (EDB number)				1	1	–	1	
Content descriptors				2	2	–	1	
E/T-CAL				2	2	–	1	
			$\sum$		512			

[a] In units of the nominal spin period $T = 4$ s.
[b] 16 samples per spin ($16 \times \frac{1}{16}$).

2.5.2. *Spin Sectorisation and Spin Phase Offset*

The RAPID data are binned into 16 sectors, numbered 0–15, during the time of one rotation about the spin axis. The start of a spin is determined by the detection of a Sun pulse, plus an offset that allows the spin boundary (start of sector 0) to be located at any desired azimuth.

For comparison of spin-averaged data, it is desirable that all experiments start their spins simultaneously. This is considered more important than having all the spin boundaries pointing in the same azimuth. Thus spin-averaged data from RAPID, PEACE, and CIS will all be taken over the same time interval.

Bearing in mind various instrumental restrictions, it has been agreed by the Cluster teams to define a spin rotation as the time from one Sun-reference-pulse plus *offset*, to the next Sun-reference-pulse plus *offset*, where *offset* is defined as a rotation angle, with the same value for all instruments. The agreed value is

Table IV(b)
Distribution of the Science Data in an EDB (4620.92 bit s^{-1}) (Telemetry mode: BM1)

Science data	M–CH	E–CH	D–CH	Bytes per set	Bytes/ spin	Acc. period (spins)	Transfer time (spins)	Duty cycle
DE 106 ions, 3 bytes each	–	–	–	318	318	1	1	100%
SGL-1 (3 counters)	–	–	–	3	80	$\frac{1}{16}$	1	100%
SGL-2 (18 counters)	–	–	–	18	9	2	2	100%
SGL-3 (22 counters)	–	–	–	22	3	2	8	25%
H-SPCT	1	8	–	8	8	1	1	100%
I-SPCT	2	8	–	16	4	4	4	100%
I-PAD	1	2	3	6	96	$\frac{1}{16}$ [b]	1	100%
I-3DD	3	8	12	288	576	$\frac{1}{16}$ [b]	8	12.5%
I-MTRX	32	64	–	2048	32	64	64	100%
E-PAD	–	–	–	–	–	–	–	–
E-3DD(BM)	–	8	9	72	1152	$\frac{1}{16}$ [a]	1	100%
m				$\frac{1}{2}$	8	$\frac{1}{16}$	1	100%
m-signs				$\frac{1}{8}$	2	$\frac{1}{16}$	1	100%
Sync marker				9	9	–	1	
Subcommutation INDEX (EDB number)				1	1	–	1	
Content descriptors				2	2	–	1	
E/T-CAL				2	2	–	1	
Spare				2	2	–	1	
			$\sum$	2304				

[a] In units of the nominal spin period $T = 4$ s.
[b] 16 samples per spin ($16 \times \frac{1}{16}$).

$$\text{offset} = 75/1024 \times 360° \approx 26.367° \ .$$

For RAPID and the Sun Sensor (which replies the Sun-reference-pulse), the relevant data for this calculation are:

	Location on spacecraft relative to $+Y$ axis	Desired angle to Sun at start of spin
Sun sensor	26.2°	26.367°
RAPID	60.0°	60.167°

From these data one calculates that the Sun is to appear at $360° - 60.167° = 299.833°$, or in sector 13.326 (see Figure 21).

Looking down from Spin Axis
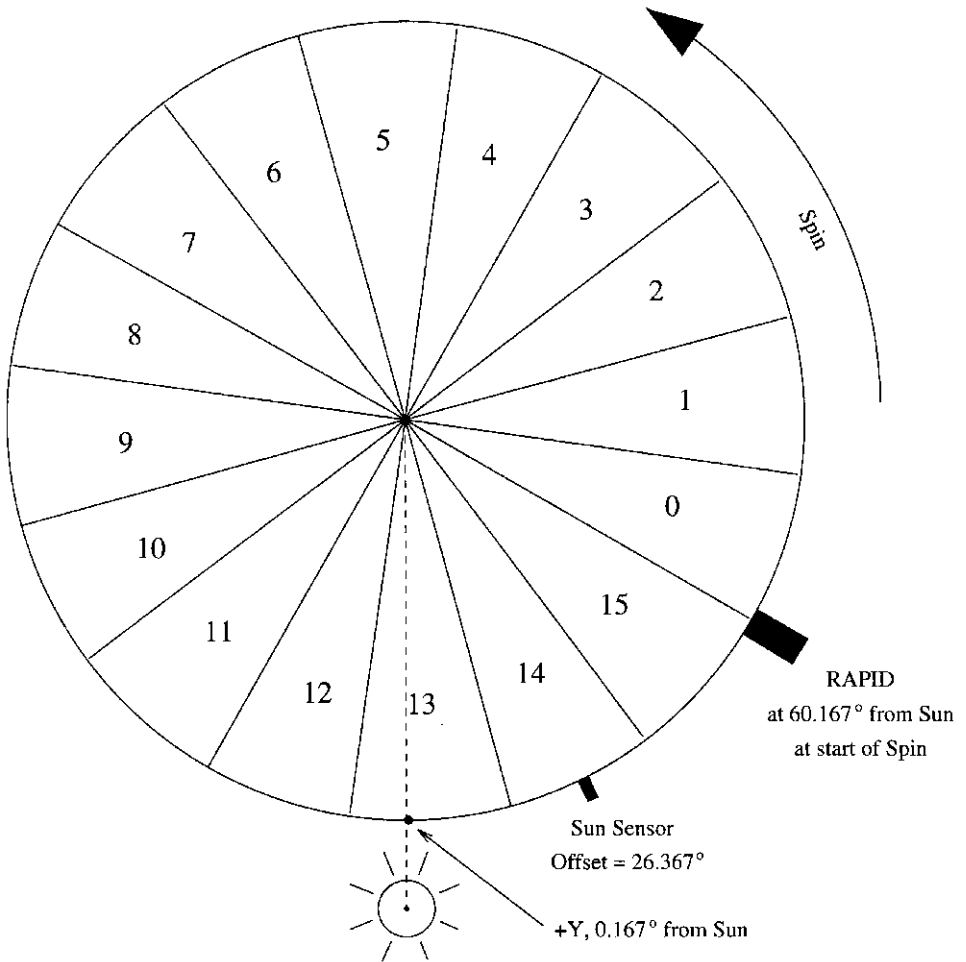
Figure 21. Definition of the RAPID sectors in the spin plan and the angular position of RAPID and the Sun Sensor relative to the Sun-satellite line at the start of a spin. Incidentally the spacecraft $+y$ axis only $0.167°$ away from the S/C-δm line at this instant in time.

For programming the DPU to accomplish this, we require the sector in which RAPID is looking when the Sun pulse occurs. This is the sector corresponding to the angle $360° - 26.367°$ which is sector 14 plus $\frac{212}{256}$. This result corresponds exactly to the precise definition of *offset*.

The azimuth of the centre of sector n is then given by

$$71.417° + 22.5°n \, .$$

The azimuth is the angle of rotation from the Sun counterclockwise when viewed looking down the spin axis (from the north). Figure 21 illustrates the position of

the Sun sensor and RAPID at the time when a spin starts. The sector pattern then follows.

It should be noted that the above formula applies only if the plane in which the Sun is sensed is located $26.2°$ from the $+Y$ axis. In the spin and attitude information given in the auxiliary files, the exact location of this plane is specified, including alignment and orientation errors. Any such deviation from the nominal value will not affect the time of the spin boundary, but will alter the centre positions of the sectors, in that their values will be *reduced* by the amount that the effective Sun sensor location is *increased*.

2.5.3. *Operational Modes*

The two RAPID spectrometers IIMS and IES, are to a large degree independent and each system can be put into specific 'configuration modes' by telecommand. Combinations of IIMS and IES configuration modes are called 'operational modes'. With just a few exceptions all 'operational modes' can be used in both telemetry modes (Science Nominal Modes NM-1 = NM-2 = NM-3 = 1024.80 bit s^{-1} and Science Burst Mode BM-1 = 4620.92 bit s^{-1}; BM-2 and BM-3 are insignificant for operational purposes).

2.5.4. *Configuration Modes*

IIMS and IES are largely independent subsystems of RAPID with different internal set-up structures called Configuration Modes (CM). Configuration modes (emergency modes are not discussed) are conveniently represented by Mode Matrices(AB) and (LMN) for IIMS and IES, respectively.

2.5.4.1. *IIMS Configuration Modes (CM)*

The IIMS CM Matrix (AB) describes two independent functional levels in the internal control system of the instrument. The parameter A defines sensor/DPU settings and the parameter B defines HV conditions in the instrument:

A	B			
0 = OFF	0 = HV OFF	(relay OFF)		
1 = S	1 = HV ON	STA = 0V	STO = 0 V	DEF = 0 V
2 = P	2 = HV ON	STA = r	STO = s	DEF = t
3 = SWG	3 = HV ON	STA = R	STO = S	DEF = T
4 = IFFT ON	4 = HV ON	STA = R	STO = S	DEF = 0 V
5 = DPU test	5 = HV ON	STA = R	STO = S	DEF = 10 kV

Explanations for the functions A: Serial (S), parallel (P) and arbitrary switching (SWG) operation of the three IIMS heads; IFFT: In-flight functional tests generator; DPU: Memory dump.

Explanations for the functions B: HV, High-voltage relay; STA, STO, DEF, high-voltage supplies for Start MCP, Stop MCP and deflection voltage DEFL; r, s, t, arbitrary step numbers (1 to 16) for STA, STO, and DEF; R, S, T, fixed step numbers for STA, STO, and DEF defined by pre-launch tests.

From these definitions follows the IIMS mode matrix **AB**:

A B	0	1	2	3	4	5
0	00	–	–	–	–	–
1	10	11	12	13	14	15
2	20	21	22	23	24	25
3	30	31	32	33	34	35
4	40	41	42	43	44	45
5	50	51	52	53	54	55

The CM matrix **AB** describes the multitude of IIMS modes available in flight operations.

2.5.4.2. *IES Configuration Modes (LMN)*

The operation of the IES subsystem requires three parameters L, M, and N which refer to three independent functional levels:

L: In-flight calibration.

A testpulse with constant amplitude is fed into the SCVC multiplexer.
This function can be activated in parallel to the current operational mode of the instrument.

M: Energy binning parameter.

This parameter transforms the 8-bit primary accuracy of energy signals into an output signal with lower or equal accuracy. The transformations are performed by look-up tables (LUTs); different LUTs are used for different instrument temperatures:

(1) LUT-1 Temperature $T = +20\ °C$, 256 to 9 binning (8 energy bins plus 1 pedestal bin).

(2) LUT-2 Temperature $T = -10\ °C$, 256 to 9 binning (8 energy bins plus 1 pedestal bin).

(3) LUT-3 Temperature $T =$ any, 1 to 1 binning (8-bit accuracy, socalled histogram mode).

This LUT is called if full energy resolution is required.

N: Integration time parameter.

This parameter defines the integration time t_{int} (2, 10, 50, 100 μs) in the detector read-out system. Selection of an integration time t_{int} depends on the ambient particle flux.

With these definitions the parameters M and N describe the IES status (the parameter L can be set to 0 or 1):

M		N		IES status
0		0		OFF
1	LUT1 (+20 °C)	1	$t = 2\ \mu$s	ON
2	LUT2 (– 10°C)	2	$t = 10\ \mu$s	ON
3	LUT3	3	$t = 50\ \mu$s	ON
4		4	$t = 100\ \mu$s	ON
5		5		MDM

MDM = Memory Dump Mode.

The resulting IES Configuration Matrix **LMN** is ($L = 0$ or 1):

M $\quad N$	0	1	2	3	4	5
0	00	–	–	–	–	–
1	–	11	12	13	14	–
2	–	21	22	23	24	–
3	–	31	32	33	34	–
4	–	–	–	–	–	–
5	–	51	52	53	54	55

2.5.5. *RAPID Operational Modes (OP Modes)*

RAPID operational modes are constructed from IIMS and IES configuration modes. Operational Modes are coded OP (AB.LMN):

Mode	AB (IIMS)	LMN (IES)
POWER ON	10	014
(default mode)		
Stand-by	10	0MN
Hot stand-by	11	0MN
Nominal operation		
Low flux mode	24	014 or 024
High flux mode	14	011 or 021
In-flight Calibration	4B (64 s)	1MN
ENA	15 or 25	LMN

The Energetic Neutral Atoms (ENA) mode is a special IIMS mode in which the deflection voltage DEF in the collimator is set to 10 kV. With this setting all ions with $E \leq 200$ keV are excluded from the detection system, i.e., detected particles with energies between 75 keV and 200 keV are considered neutral atoms.

The detection of ENAs requires the RAPID unit on only one spacecraft to be configured in the ENA mode (OP 15.LMN or 25.LMN). Orbital segments in the lobes/polar cap are ideal for this purpose (low background from ions).

2.6. ROUTINE IN-ORBIT OPERATIONS

The routine operations of RAPID are largely driven by the ambient particle flux (i.e., the region in geospace). Two selected categories of orbit may serve to illustrate anticipated sequences of operational modes (OP) along a trajectory:

(1) Apogee in the magnetotail inside the magnetopause

Region in geospace	OP	Mode
Plasma sheet	14.011 or 14.021	nominal high flux
Magnetopause (skimming)	14.011 or 14.021	nominal high flux
Lobe/polar cap	24.014 or 24.024	nominal low flux
Cusp	24.014 or 24.024	nominal low flux
Inner magnetosphere	11.011 or 11.021	hot stand-by (IIMS)
(inside $L = 5$)		

(2) Apogee in the solar wind (outside the bow shock)

Region in geospace	OP	Mode
Solar wind	24.014 or 24.024	nominal low flux
Bow shock	24.014 or 24.024	nominal low flux
Magnetosheath	24.014 or 24.024	nominal low flux
Magnetopause (crossing)	14.011 or 14.021	nominal high flux
Cusp	24.014 or 24.024	nominal low flux
Polar cap/lobe	24.014 or 24.024	nominal low flux
Inner Magnetosphere (inside $L = 5$)	11.011 or 11.021	hot stand-by (IIMS)

Transitions between Operational Modes require predefined groups of telecommands (socalled procedures Pn). A major concern in the RAPID commanding is to take proper account of the high voltage switching involved in a chosen sequence of telecommands (e.g., HV relay position, HV limit value, HV target value, etc.). The 'road map' in Figure 22 provides an overview for transitions between 'adjacent' operational modes (major modes are highlighted by heavy lines) and safe routes to more 'distant' OPs.

2.7. DATA HANDLING

The Onboard Data Handling (OBDH) system of CLUSTER integrates RAPID data into the CLUSTER telemetry format and prepares the transmission to a ground station. After placing the CLUSTER data on a suitable storage medium (CD-ROMs) the complete data set is made available to each PI institute and the national institutions participating in the CLUSTER Science Data System (CSDS). It is the task of the German CLUSTER Data Center (GCDC) to extract the RAPID data from the storage medium (CD-ROM) and convert selected subsets to physical units and make them, depending on the time resolution, accessible by the CLUSTER teams and the general scientific community, respectively. Spin-averaged time profiles of fluxes for electrons, protons, helium, and CNO group ions for two energy ranges each and field aligned anisotropies for electrons and protons from four satellites are provided for coordinated data analysis by CLUSTER Co-Investigators, while one-minute averages of the same parameters from a single spacecraft are made available to the general scientific community. For both data sets, publication may be undertaken only with the approval of the RAPID PI. These GSCS data products are complemented by the data analysis effort at the institutions participating in the RAPID investigation.

IDA/MPAe
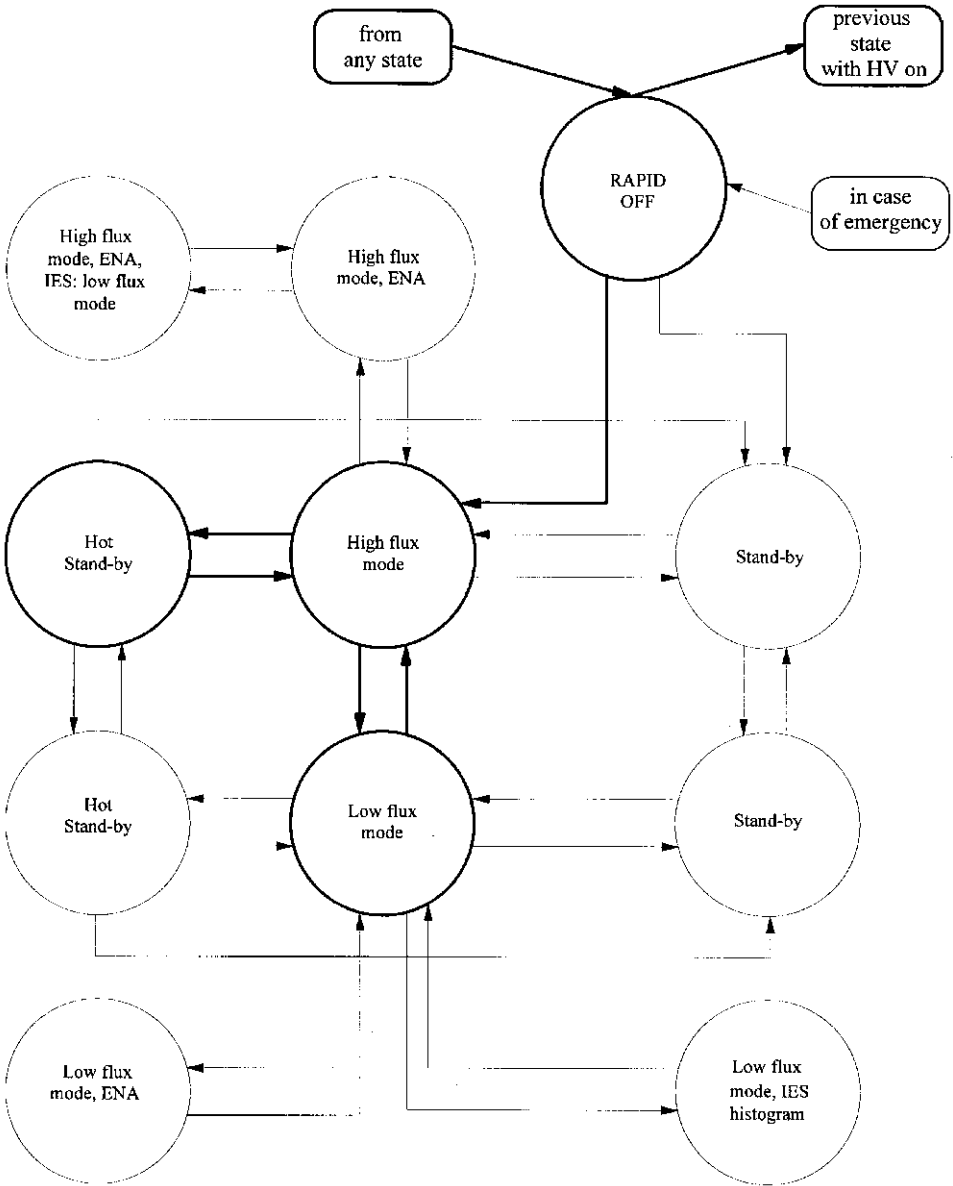
Figure 22. Road map for transitions between different configuration modes CM illustrating the principle. Major modes are connected by heavy lines.

CLUSTER passes through regions in geospace with vastly different field topologies and plasma properties. Reliable region identification is therefore essential for a successful interpretation of the RAPID measurements. Identification of characteristic regions in the magnetosphere such as plasmasheet, lobes, cusp, and
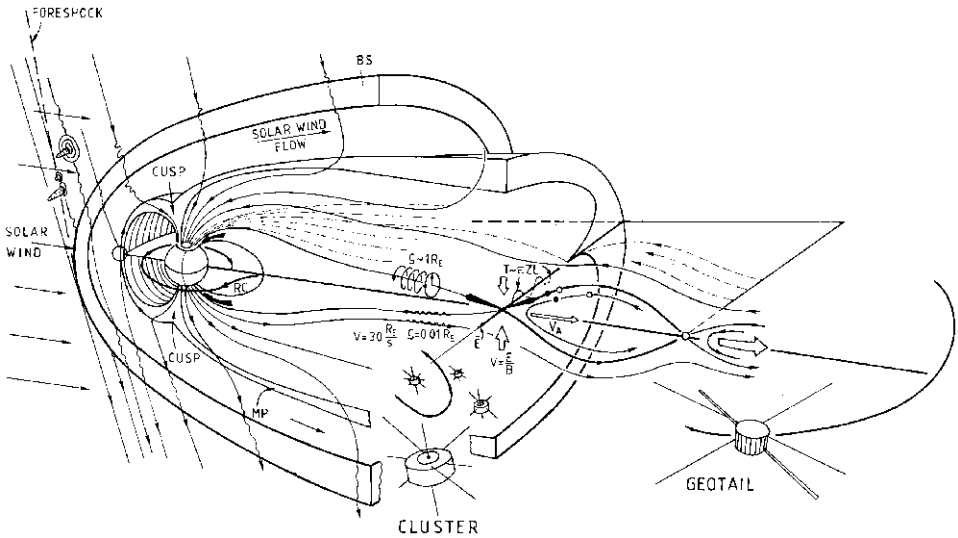
Figure 23. Three-dimensional 'tail-view' of the Earth's magnetosphere with the Cluster fleet of spacecraft and *Geotail*.

magnetopause make it mandatory to combine the RAPID data with magnetic field and plasma observations. An important contribution from RAPID is the coverage of the high energy tail in the particle distribution functions and the detection of boundaries by remote sensing techniques (e.g., deviations from gyrotropy).

3. Scientific Objectives

3.1. INTRODUCTION

The energetic-particle measurements with RAPID will be able to expand significantly our understanding of solar-terrestrial physical processes in most principal regions of the magnetosphere. These are in particular the: (1) middle magnetosphere, (2) low latitude boundary layer, (3) auroral zone extension to high altitude, (4) plasma sheet and its associated boundary layer, (5) plasma mantle/tail lobes, (6) magnetopause, (7) cusp/magnetosheath, and (8) bow shock region.

Figure 23 illustrates a tail-view of the magnetospheric system, showing most of the plasma regions and boundaries presently believed to exist in geospace. The microphysical processes occurring within these key regions – especially during the times of major dynamical reconfigurations – are areas in which RAPID will provide essential information. These studies are particularly dependent upon the four-spacecraft Cluster configuration.

The following topics are meant to highlight the scientific contributions that can be made with RAPID but they can by no means give a complete picture of the

return expected from this instrument.

3.1.1. *Energetic Particles as Scientific Tools*

The energetic tail of the plasma distribution is often considered insignificant in plasma dynamics, though in many of the magnetospheric regions it can contribute significantly to the total plasma energy density. Furthermore, the high speed and substantial gyroradii of energetic particles can probe with high time resolution plasma properties and magnetic-field topologies over large distances. For example, 50 keV electrons travel along field lines with a speed of nearly 20 R_E s^{-1}. These swift electrons trace-out field lines in the magnetosphere and in the magnetotail in a rather short time. They can provide nearly instantaneous information about changes in the field configuration in distant regions of geospace.

Energetic ions, on the other hand, have large gyroradii which sense the existence or the approach of boundaries over thousands of kilometres. Figure 24 delineates the remote-sensing capabilities of 100 keV protons (90° pitch-angle assumed) in the context of a Cluster tetrahedron (the separation distance between the four spacecraft is assumed to be 1 R_E). The approximate dimensions of the tetrahedron/gyroradius systems are shown schematically for five selected key regions in geospace. The five insets illustrate the length of the local gyroradius in relation to the spacecraft separation distance.

It is obvious from Figure 24 that large separation distances between the Cluster spacecrafts are particularly important in the upstream region and in the magnetotail (in particular in the plasma sheet). For short separation distances (1000 km or less) the remote-sensing ranges of the four spacecrafts overlap strongly and the performance of the tetrahedron is essentially reduced to that of a single platform. It should be noted, however, that electron gyroradii (100 keV) are always small compared to the size of the tetrahedron.

Finite gyroradius effects in the ion angular distribution function have been successfully used on ISEE to probe the dayside magnetopause (Fritz *et al.*, 1982), FTE motion (Daly and Keppler, 1982), and plasma sheet motion in the geotail (Andrews *et al.*, 1981). The remote-sensing method can be applied in many ways, both for step function gradients and for finite density gradients.

Although this method has the advantage that boundary orientations and motions can be determined by a single spacecraft, it does contain some problems and ambiguities. The application of the step function gradient is often complicated, being tailored to each event individually. The finite gradient permits an analytical application by means of particle anisotropy measurements, but the additional Compton-Getting (motional) anisotropies must also be corrected for. In both cases, a rotation of the magnetic field during the analysis period introduces intractable complications.

A necessary assumption in all applications of remote-sensing is that the particle boundaries have a radius of curvature much greater than the ion gyroradius, i.e.,
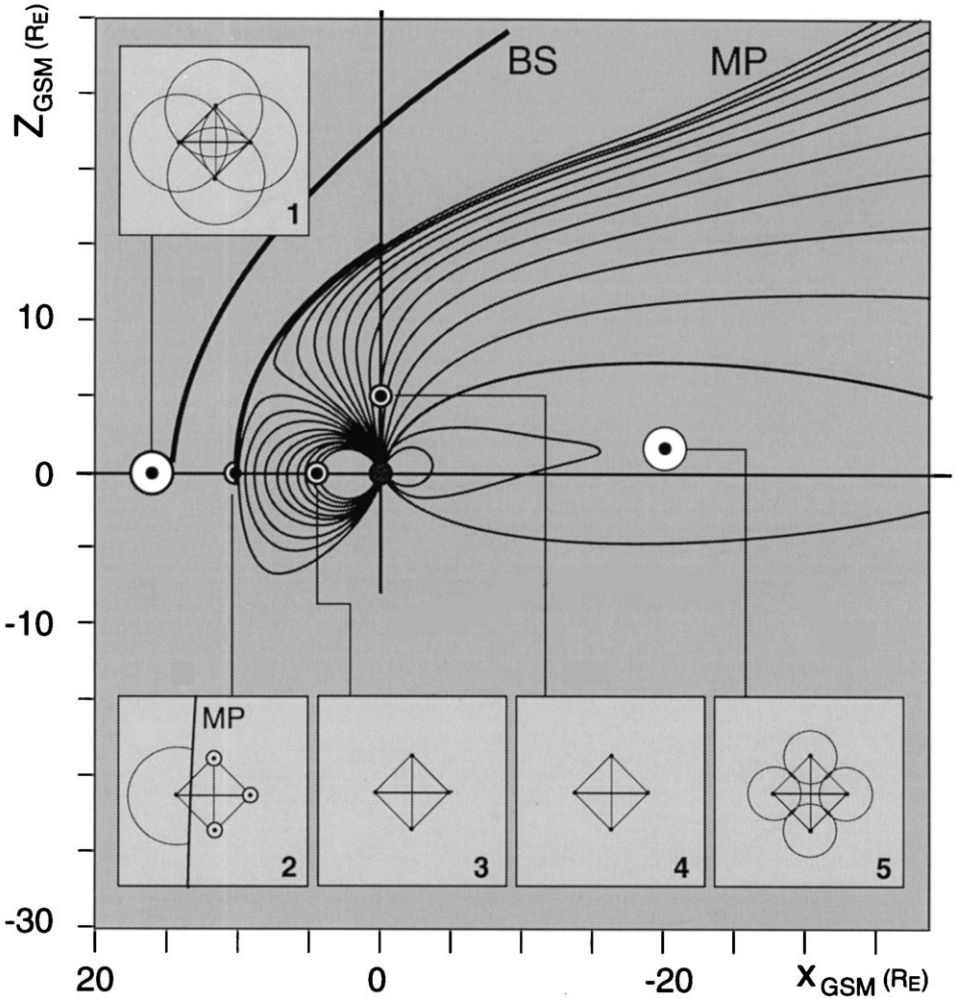
Figure 24. The Cluster tetrahedron (separation 1 R_E) and the remote-sensing distance of energetic particles in geospace illustrated for 100 keV protons and 90° pitch angle. Circles in five selected regions in the noon-midnight meridian indicate the approximate size of the local tetrahedron-plus-gyroradius geometry (the circles are drawn in the paper plane but they are actually perpendicular to the local magnetic field vector). The five insets show the relative length of the gyroradius for the different locations. In the inner magnetosphere 3 and 4 the gyroradii are too small to be resolved.

that they be planar. Departures from this assumption have been found at the magnetopause (Fahnenstiel, 1981) and in the geomagnetic tail (Andrews *et al.*, 1981). In such situations only multi-spacecraft analyses will be able to determine the complicated surface-wave motion of the boundary in question.

3.1.2. *The Role of Energetic Particles in Space Physics*

As we consider the orginal exploration of the terrestrial magnetosphere, we see that energetic particles (along with magnetic-field measurements) first revealed the existence of the Van Allen radiation belts, the magnetopause, the magnetosheath, the bow shock, the plasma sheet and much about the length and persistence of the geomagnetic tail. In a very real sense, the exploration of the rest of the Solar System has also been led by the detection of energetic particles. The remarkable discoveries and interpretations of the Pioneer-10 and -11 missions to Jupiter and to Saturn basically relied upon energetic (≥ 50 keV) particle measurements: the discoveries made and the models formed based upon these measurements remain very much in place today, even after other missions to these planets have occurred. Similarly, in the case of Mercury – explored thus far only by Mariner-10 – we basically only have knowledge of the ≥ 35 keV electron population and a portion of the thermal electron population. Nonetheless, we have a remarkably persuasive picture of the basic elements of the Hermean system (Baker *et al.*, 1986).

The IMP-8 spacecraft had on-board sensors of large geometric factor that provided very sensitive measurements of ≥ 200 keV electrons at $\sim 35 \, R_E$ geocentric distance. With these nearly continuous measurements, Baker and Stone (1976, 1977a, b, 1978) were able to map and probe the complete structure of the middle magnetotail as never before. Energetic electron layers were discovered carrying significant energy flows outside the magnetopause and this energy flux was seen to vary with the nature of the solar wind-magnetosphere interactivity. In an even more dramatic demonstration of the importance of energetic electrons, such early work clearly delineated regions of open and closed magnetic field lines in the midtail region and thus contributed crucially to understanding and resolving an internal debate going on between groups measuring only the lower energy (≤ 30 keV) plasma. Subsequent work using the IMP-8 electron sensors (Bieber *et al.*, 1982) demonstrated in a clear way that energetic electrons, and only energetic electrons, can be used to fully assess magnetic-field-line topology and thus distinguish between competing magnetotail dynamics models. The work referred to here remains definitive and similar methods were used extensively on ISEE-1 and -2 (Fritz *et al.*, 1984) to assess where, when and how acceleration and transport processes occur in and around the magnetosphere.

In another context, a large data set dominated by 3D electron measurements for energies ≥ 30 keV has been obtained for nearly two decades at geostationary orbit by the Los Alamos spacecraft (Baker *et al.*, 1982). Using these data as a basis, it has been possible to understand many of the issues related to the acceleration, transport and loss of energetic particles in the near-tail region. Indeed, it is the improved understanding of the microphysics of near-tail (substorm) acceleration that will be in the focus of Cluster. The beauty and strength of energetic-particle measurements lies in their high rectilinear speed and their relative immunity to large-scale magnetospheric convection electric fields. With such particles we can see clearly separated plasma regions, we can uniquely assess field-line topologies,

we can map connectivity from the magnetospheric equatorial plane to the ionosphere, and we can sense the global changes in magnetospheric configuration that lead inevitably to substorm onset (Baker *et al.*, 1981, 1984).

Quite recently our team has had the experience of ISEE-3 and *Geotail* in the deep-magnetotail, as a case in point of the importance of energetic particles. A major result of the ISEE-3 tail mission was the confirmation of the release of plasmoids during substorms and the ≥ 70 keV electron have proven to be crucial in establishing the field structure, topology and scale size of plasmoids (Scholer *et al.*, 1984, 1985; Wilken *et al.*, 1995).

There can be a tendency in the study of plasma systems to look only in the region of maximal number density and ignore the tail of the plasma distribution function. However, in an astrophysical sense, most of what we know about the Universe comes from energetic-electron-associated processes. It is the synchrotron emission in active galactic nuclei, in radio jets and in remote stellar systems that tell us of the magnetic, electrical and plasma properties of these systems. It is the synchrotron and bremsstrahlung X-ray emissions that come from electrons that tell us of the environments of distant pulsars. It is energetic electrons that give us Type II and Type III solar radio bursts and it is electrons that let us diagnose distant supernova shock fronts as they propagate through the interstellar medium. Thus, we are reliant upon energetic electrons in the cosmic sense, and this emphasises even more the importance of understanding their acceleration and transport in our best and greatest local opportunity, namely, the Earth's magnetosphere.

What, then, will emerge as the principal science foci of Cluster? Undoubtedly there will be great attention to magnetotail acceleration regions and to plasma boundary regions. Key to making progress will be assessing field-line mapping and topology, the nature of the acceleration process, the mechanisms of particle transport in the tail and detailed study of the boundaries separating distinctly different plasma regions. We can sensibly carry out these studies only by using complete energetic-particle measurements on Cluster. Only energetic particles have the high speeds ($\geq 0.2c$) to allow assessment of magnetic reconnection regions. Only electrons counterpointed with ion measurements can be used to diagnose the nature of the tail acceleration region. Only electrons, specifically, have the small gyroradii to permit the rapid probing while preserving the clear separation between topologically distinct plasma regimes.

3.1.3. *RAPID and the Plasma Instruments CIS and PEACE*

The Cluster scientific payload is a carefully balanced set of instruments covering the full range of plasma waves, fields and particle parameters. All of these instruments are needed to generate a comprehensive description of static and dynamic plasma conditions. Among these instruments the energetic-particle spectrometer RAPID and the plasma instruments CIS (Cluster Ion composition Spectrometer) and PEACE (Plasma Electron and Current Experiment) form a triad of particle instruments in which the inherent low pass filter functions of the two plasma ana-

lysers is complemented by the RAPID high pass filters for ions and electrons. The combined CIS/PEACE/RAPID measurements effectively eliminate 'window effects' which often lead to misinterpretations.

The ion composition instrument CIS is capable of obtaining full 3D ion distributions with mass per charge composition determination. It covers the energy range between about 0 and 40 keV e^{-1}. The electron analyser PEACE measures electrons between 0.7 eV and 26 keV. The energy ranges of these instruments connect directly to the energy ranges of the RAPID instrument (20 keV to 450 keV for electrons and 40 keV to 1500 keV for protons).

Comprehensive energy coverage is fundamental in studying for example boundaries and boundary layers in space plasmas. This may help to answer the following selected questions:

– How does the plasma cross the magnetopause and enter onto closed field-lines?

– How can the reconnection sites on both the equatorward and poleward edges be identified? Where does reconnection most preferentially take place?

– What are the widths of magnetopause boundary layers? How do they vary along the flanks and how do they depend on the IMF polarity (northward/southward)? How important are these boundary layers in driving large-scale magnetospheric convection?

– How do the magnetopause (dayside) currents couple to the cusp field-aligned currents?

– What are the general characteristics of current sheets (density, flow, temperature, heat fluxes, beta)?

– What is the structure of the cross-tail current sheet?

– Which feature in the magnetosphere corresponds to the Harang discontinuity?

3.2. BOW SHOCK AND UPSTREAM PHENOMENA

One prominent feature in the solar wind interaction with the magnetosphere concerns the various particle-acceleration processes occurring upstream of and at the bow shock. The ISEE-1 and -2 observations have shown that these regions are very rich in small- and large-scale phenomena directly related to the generation of plasma turbulence and particle energisation, and hence are most important for testing theories of different shock acceleration mechanisms and wave-particle interactions. Some of the ISEE results and the advances expected from the Cluster mission are outlined in the following.

Particle acceleration at MHD shocks has become one of the key topics in space plasma physics during the last decade, stimulated by both extensive theoretical studies and in-situ measurements within the Solar System. In this field, the Earth's bow shock has attracted particular attention because of its proximity. The energetic-particle population near the bow shock has been related to diffusive Fermi acceleration (Gosling *et al.*, 1978; Scholer *et al.*, 1979; Wibberenz *et al.*, 1985) and compared

with model calculations (Lee, 1982; Ellison, 1985). Recently, the bow shock origin of the diffusive upstream ions has been questioned (Anagnostopoulous *et al.*, 1986; Sarris *et al.*, 1986) and it has been proposed that this energetic-particle population is due to escape of magnetospheric ions into the upstream region. The question is of considerable importance.

Diagnostic tools to distinguish these two origins are the following:

– simultaneous measurements of ions and electrons at different positions inside and outside the Earth's magnetosphere,

– check for the simultaneous occurrence of an electron component (the bow shock acceleration in the energy range above 20 keV is restricted to ions),

– correlation with the momentary directions of the interplanetary magnetic field and flow direction of the solar wind,

– measurement of the energy spectrum over a wide range, throughout various phases of individual events,

– measurement of the chemical composition,

– correlation with the simultaneous occurrence of an increased level of turbulence in the magnetic field,

– study of anisotropies in three dimensions.

Apart from the question of the origin of upstream particles, a number of fundamental problems in the interaction between the bow shock and energetic particles are still unsolved. These include: the injection of thermal solar wind ions into the diffusive shock acceleration mechanism, in relation to the shock structure; the efficiency of shock acceleration as a function of the shock Mach number, the shock normal angle, the position on the bow shock etc.; the escape mechanism (upstream, downstream, perpendicular to the average field) which finally determines the shape of the energy spectrum; conditions for the growth of wave turbulence; the scattering of particles by hydromagnetic turbulence, in particular, the variation of the mean free path with particle parameters like velocity and/or energy/charge; the conditions for the appearance of limiting fluxes in a steady state situation; the influence of the accelerated particles on the ambient medium.

Previous studies established, depending on the location around the shock front, two separate populations of suprathermal ions. The so-called beam ions, observed predominantly in the quasi-perpendicular bow shock regime (Asbridge *et al.*, 1968; Gosling *et al.*, 1978; Paschmann *et al.*, 1979) were identified as beams of particles streaming along the interplanetary magnetic field, with energies that seldom exceed 20 keV. However, at higher energies, a reflected diffuse ion population exists in the quasi-parallel shock regime (Lin *et al.*, 1974; Gosling *et al.*, 1978). The diffuse ions (protons, alphas, and CNO) have energies in the range 30–100 keV, and exhibit rather isotropic distribution, indicating a process of random scattering. Diffuse shock acceleration might be at work here. Another population, intermediate between the beam ions and the diffuse ions, has also been identified (Paschmann *et al.*, 1981).

It is possible that, while the beam ions have their origin in the specular reflection of solar wind ions at the quasi-perpendicular shock front (Sonnerup, 1969; Paschmann *et al.*, 1980) some of them could act as seed particles for the diffuse ions via further acceleration. The energy density of the reflected diffuse ions is about one third of the solar-wind-energy density (Ipavich *et al.*, 1981b), the shock acceleration is thus a very efficient mechanism. Mitchell and Roelof (1983) have made the interesting suggestion that the acceleration of the diffuse ions is self-limiting in the sense that the parallel energy ($E_{\parallel}$) of the 30–200 keV energy ions cannot exceed the magnetic-field-energy density ($B^2/2\mu_0$) by more than a factor of 2. This effect can be investigated in detail with the RAPID instrument as it has comprehensive angular (4π) as well as energy (20 keV to 1 MeV) coverage for different ion species (p, α, and CNO). Observations at the four different positions relative to the shock will specifiy the boundary conditions for models of the processes occurring.

The appearance of the diffuse energetic ions is usually accompanied by large-amplitude low-frequency waves in the magnetic field as well as the solar wind plasma. The presence of ULF waves is essential in the theoretical model of first-order Fermi acceleration (Axford, 1981; Lee, 1983). The Fermi acceleration mechanism requires that the ions be resonantly scattered between the converging upstream magnetic irregularities and the shock front or the downstream waves. Several ingredients are important in the diffuse shock acceleration process. First of all, the diffusion coefficient ($K_{\parallel}$) should have a certain energy dependence such that the scale length λ for the e-folding distances for the upstream distribution of the diffuse ions should be different for ions of different energies. While Ipavich *et al.* (1981a) have determined $\lambda = 7.2 \ R_E$ for 30 keV-protons, Wibberenz *et al.* (1985) have found $\lambda = \text{const.} \ (6.5 \pm 1.5 \ R_E)$ for 25–36 keV protons without significant energy dependence. With the energy window of the RAPID experiment covering the full energy width of the upstream diffuse ions and with multiple measurements at the different positions of the spacecraft, this outstanding issue will be thoroughly addressed by the Cluster mission.

Cluster will offer the advantage of simultaneous multipoint composition measurements of complete spectra from thermal energies up to hundreds of keV, with coordinated RAPID and CIS measurements. In addition, both RAPID and CIS are capable of obtaining full 3D ion distributions with high time resolution.

Other issues that shall be thoroughly addressed by RAPID measurements are:

– exact determination of the bow shock and its motion through detailed examinations of small-scale structures,

– energy dependence of the diffusion coefficient K through the multipoint measurements of RAPID that cover the full energy width of the upstream diffuse ions,

– comparative importance of parallel and perpendicular diffusion,

– specification of the boundary conditions for the models of the processes leading to beam ions and diffuse ions.

The temporal and directional variations of the interplanetary magnetic field have obviously strong effects on the upstream particle population. Simultaneous observations of the undisturbed solar wind by the SOHO and WIND spacecraft will be of great importance in correlating the various magnetospheric phenomena with interplanetary conditions.

3.3. THE MAGNETOPAUSE, MAGNETOSHEATH, AND CUSP REGIONS

After deceleration at the bow shock, the solar wind plasma continues to travel through the magnetosheath around the magnetopause, the actual separation between the solar wind and terrestrial magnetic field. The main questions regarding this region are:

  – Which is the dominant source for energetic ions in the magnetosheath?
  – What processes occur during the propagation of the plasma from the bow shock to the magnetopause?
  – To what extent, where and under what conditions is the magnetopause penetrated by the solar wind?

Several studies have shown that both the bow shock and the magnetosphere are sources of energetic ions in the magnetosheath (Anagnostopoulos and Kaliabetsos, 1994). Multispecies measurements from the AMPTE/CCE spacecraft covering the wide energy range 1.5 keV–2 MeV (Paschalidis, 1994) indicated that the leakage of magnetospheric particles is the most important contributor to the energetic ($E \geq 50$ keV) population of the magnetosheath, as compared to Fermi acceleration and to shock drift acceleration. Fermi acceleration predicts the opposite local time asymmetry than that observed by AMPTE/CCE (spectra harder at the duskside than at the dawnside), and shock drift acceleration should be a minor contributor to the energetic population because of upper-energy cutoff limitations.

Cluster will provide multi-point composition measurements over a wide energy range which are essential for the assessment of the issues regarding the magnetosheath and magnetopause region.

3.3.1. *Magnetic-Field-Line Reconnection and Flux Transfer Events (FTE)*

Over a quarter century ago it was suggested that the magnetic field lines in the solar wind could combine with those of the Earth to provide direct entry and acceleration of solar wind plasma into the magnetosphere. This process, known as 'reconnection' or 'merging', is thought to be the basic mechanism responsible for the input of solar wind energy into the magnetosphere, and formation of the plasma convection in the magnetosphere and ionosphere. Dungey (1961) first suggested that magnetic reconnection between the Earth's magnetic field and the IMF may occur at the dayside magnetopause when the IMF has a southward orientation. Fast plasma observations from ISEE-1 and -2 provided the first convincing *in-situ* evidence for quasi-steady-state reconnection at the dayside magnetopause (Paschmann *et al.*, 1979; Korth *et al.*, 1982; Sonnerup *et al.*, 1981). By analysing

data of ISEE-1 and -2, Russell and Elphic (1978, 1979) found that reconnection in the dayside magnetospheric boundary region appears to be more frequently associated with the FTEs. Since then various theoretical transient reconnection models have been developed to explain the formation and observed features of FTEs (Lee and Fu, 1985; Scholer, 1988; Southwood *et al.*, 1988; Liu and Hu, 1988).

The reconnection process has turned out to be far more complicated than originally imagined. The multi-point measurements of the Cluster experiments will be able to probe the complex structure of reconnection events in terms of spectra, composition and flow directions, thus yielding information on energisation, sources and motion of the particles. In addition, the ability to use finite gyroradius effects is a powerful tool to detect the motion of the structure as a whole.

Principal observational features of so-called FTEs at the magnetopause are:

– a sinusoidal fluctuation in B_N, the component of the magnetic-field normal (and outwards) to the magnetopause,

– isotropic electrons and streaming ions in the magnetosheath.

Field-aligned anisotropies of energetic ions uniquely identify the magnetospheric hemisphere to which the magnetosheath field line is connected.

In the magnetosphere, the energetic-particle intensities are reduced during FTEs, to values that are only slightly higher than in the magnetosheath FTEs. This indicates that the FTEs have a continuity through the magnetopause permitting magnetospheric energetic particles to escape into the magnetosheath, and possibly into interplanetary space. Conversely, it has also been demonstrated by Paschmann *et al.* (1982) that magnetosheath plasma is found within the magnetospheric FTEs. These phenomena have also been observed by GEOS and STARE (Sofko *et al.*, 1979).

Surveys of the occurrence and properties of FTEs (Rijnbeek *et al.*, 1984; Daly *et al.*, 1984) demonstrate that they are a persistent feature of the dayside magnetopause during times when the interplanetary field is directed southward.

Using ISEE-1 and -2 to make two-point measurements of FTEs, Saunders *et al.* (1984) have shown that the events are highly structured, possessing twisted field-lines and vortex plasma motion. In fact, based on these measurements alternate interpretations of FTE signatures have been proposed by Saunders (1983) and Southwood *et al.* (1988). According to the suggestion by Saunders (1983) FTE signals will be observed if a flux bulge due to transient changes in the rate of quasi-steady reconnection passes across the satellite. It is quite clear that four-point measurements will greatly add to our understanding of these complex features by probing in detail their cross-sectional structure and temporal variations.

That FTEs are spatially and temporally localised reconnection events is now widely (although not universally) accepted. It is even believed that there is a continuous spectrum of reconnection event sizes and time scales covering the range from quasi-stationary reconnection to the fastest FTEs. Another possibility is that FTEs are very large scale features of the magnetopause that only appear to be localised due to wave motion of the magnetopause surface and the (at best) two-

point measurements previously available. The four-point measurements of Cluster will be able to answer this question in ways that the two-point measurements of ISEE could not. Energetic-particle measurements are vital to any investigation of reconnection events because:

– they are the only reliable indicator in the magnetosheath of the hemisphere to which the flux tube is connected (necessary for source determination);

– the fact that the particles exist for longer than their bounce time (about 1 min for 25 keV protons) means that there is a resupply process, which is still one of the mysteries of reconnection observations for which multi-point spectral measurements are required;

– composition measurements are essential for the resupply and source determination;

– the use of energetic particles as remote-sensing probes can determine orientation and motion of the events, needed to discover their ultimate destination and four-point measurements will be necessary if the radius of curvature of the event surface is comparable to the ion gyroradius, as appears most likely.

So far reconnection at the dayside magnetopause for southward IMF has been studied extensively. It has also been suggested that when the IMF has a northward component, reconnection proceeds in high latitudes behind the cusps. Dungey (1963) first inferred that magnetic reconnection could occur at the nightside magnetopause while the IMF is northward. Following Dungey's expectation some authors discussed the possible reconnection site, processes and associated effects during northward IMF periods (Russell, 1972; Maezawa, 1976; McDiarmid, 1978; Crooker, 1979). ISEE-3 data showed that plasmas in the magnetosheath can enter the magnetosphere through a large area on the magnetopause, implying that in general the magnetotail has an open configuration (Gosling *et al.*, 1984, 1985). Song and Russell (1992) suggested that high-latitude reconnection behind the polar cusps may lead to the formation of the low-latitude boundary layer for northward IMF. Stasiewicz (1991) discussed a global model of magnetic merging in more general situations.

A recent two-dimensional MHD simulation studied the transient reconnection in the high-latitude boundary layer (HLBL) and proposed a global reconnection model for the period of northward IMF (Liu *et al.*, 1994; Liu *et al.*, 1995; Zhang and Liu, 1995; Zhang *et al.*, 1995). It was found that the Kelvin-Hemholtz instability generated by the flow shear in the boundary layer causes generator effects which may increase the growth rate of the tearing mode instability, thus leading to reconnection in the nightside HLBL.

It has been shown that when the IMF is northward, in the auroral magnetosphere, the electric-field patterns, field-aligned currents, particle precipitation and auroral phenomena are considerably different to those in southward IMF periods (Schunk, 1988). We suggested that magnetic reconnection in HLBL plays a crucial role in leading to these complex phenomena.

Signatures of reconnection in the HLBL which RAPID measurements will help to identify include:

– Generally energetic particle flows in the nightside HLBL are tailward. If there are Earthward energetic particle flows somewhere behind the cusps, they may be regarded as clear evidence of nightside high-latitude boundary-layer reconnection.

– When magnetic reconnection proceeds, the magnetic line in the reconnection region must be open. Thus it is expected that the particles in the HLBL are a mixture of magnetospheric and magnetosheath populations, albeit with occasional heating.

– Magnetic reconnection at HLBL should produce plasmoids as well.

– High-speed plasma flows with a magnitude greater than $400 \, \mathrm{km \, s^{-1}}$ persisting in various time scales can also be regarded as a signature of transient and quasi-steady-state reconnection.

– Heavy ions from the ionosphere may be observed in both the HLBL and the adjacent nightside magnetosheath.

3.4. MAGNETIC STORMS AND SUBSTORMS

3.4.1. *The Storm Time Magnetosphere*

RAPID will be an ideal instrument to continue the line of research in the investigation of Geomagnetic Storms suggested by work with the CRRES and Viking satellites. Viking found a polar cap dominated by He^{+2} ions, and a transition to a more equatorial, trapped belt of He^{+} ions. This feature can also be seen by CRRES, and is compatible with the charge exchange process. There is a need to compare observations with detailed models for charge exchange processes, in order to establish how much of this behaviour is due to charge exchange, and how much to the injection of new populations.

Solar wind alpha-particle entry to the magnetosphere during quiet times was initially investigated using *Viking* data. It was found that the variation of the mean charge state with invariant latitude is significantly different from that of the anisotropy. This indicates the existence of a transition region where particles diffusing to lower latitude are trapped. They subsequently diffuse to still lower latitudes, and undergo charge exchange, thus providing a major source of inner magnetosphere singly-charged helium. There appears to be a very low abundance of oxygen in this region, again suggesting that the singly-charged helium population is not extracted from the ionosphere.

Studies with calculations of ion trajectories have shown that high cross-tail electric fields at very disturbed times allow direct access of ions from the solar wind into the midnight region. The four-spacecraft configuration of Cluster and the full angular coverage available from RAPID will be a powerful tool for testing the entry model calculations, as well as investigating flows along the lobe boundaries, in order to investigate the connectivity at this time.

The composition ratios of energetic ions measured by RAPID, combined with data from the upstream monitors (Wind and SOHO), can help to identify changes in

the solar wind source populations during storms. The speed of entry into the magnetosphere will be compared with estimates from existing models (Fennell *et al.*, 1993; Yeoman *et al.*, submitted) to assess the required magnitude and variation of the cross-tail electric field. During quiet times we can use the particle pitch-angle distributions and composition ratios to examine the inward diffusion of solar wind material from polar cap entry to trapping region and subsequently to lower latitudes in order to assess this mechanism as a major source of magnetospheric ions.

An interesting aspect will be to study large scale changes and the calorimetry of the ring current during active storm and substorm periods. This will be performed by using a relatively novel technique which was previously used on *Geotail*: a special operating mode of the RAPID instrument (ENA mode, Section 2.5.5) allows the detection of Energetic Neutral Atoms (ENAs). ENAs are produced as a result of charge exchange reactions between energetic ring current ions and low-energy neutral hydrogen. As the resulting neutrals are unaffected by magnetic or electric fields they provide a useful mechanism for remote-sensing dominant source region enabling calorimetry of the energy transfers to the ring current during storms and substorms to be performed. The detection of ENAs with RAPID is delineated in Section 3.5.

3.4.2. *Substorms and Their Near-Earth Manifestations*

Magnetospheric substorms have been investigated for several decades (Akasofu, 1991). Substorm phenomena are related to the interaction between the solar wind, the magnetosphere and the ionosphere. Current phenomenological models describe substorms in terms of different phases: growth phase, expansion phase, and recovery phase (Rostoker *et al.*, 1980). The sequence of these phases is reflected in the development of the cross-tail current (Kaufmann, 1987). The growth phase begins typically about one hour before the onset of the expansion phase and results in a stretching of the geomagnetic field-lines towards a more tail-like configuration (McPherron, 1972) attributed to an increase in the cross-tail current in the near-Earth plasma sheet. The stretched magnetic field in the tail represents a large reservoir of magnetic energy which can drive magnetospheric substorms. An outstanding feature of substorms is the sudden onset of the expansion phase (the so-called substorm onset) characterised by auroral breakup phenomena and strong spatial and temporal variations of the relevant magnetospheric parameters. During this short time interval (a few minutes) the magnetosphere recovers from the stretched configuration towards a more dipolar-like configuration with strong variations of the particle fluxes (Sauvaud and Winkler, 1980). The reconfiguration (the so-called dipolarisation) is associated with a partial diversion (i.e., decrease) of the cross-tail current into the ionosphere (Kaufmann, 1987). Increase in the electron fluxes (electron injection) and the accompanying dipolarisation may be delayed by up to a few minutes with respect to substorm onsets (Korth *et al.*, 1991; Pu *et al.*, 1992).

Over the last decade, new and better observations are gradually leading to a more consistent model of the interrelations between these various magnetospheric

phenomena. Despite these advancements it has not yet been possible to establish a model that fits all sets of observations. Fundamental arguments related to basic substorm physics persist and different competing substorm models describing the observations are appearing in the literature. Summaries of substorm models were given by Lui (1991) and Siscoe (1993).

Most of the controversies in connection with substorm models are associated with the processes that are thought to trigger the expansion phase, in which region of geospace the expansion is initiated, and the relationship between near-Earth observations and high-speed ion flows further down the tail (Lopez, 1993). The suddenness of the expansion onset led to the assumption of an instability which diverts (or disrupts) the cross-tail current. Auroral morphology studies performed with data from the Viking satellite (Elphinstone *et al.*, 1991) demonstrate that the first arcs to develop at breakup are conjugate in the Tsyganenko magnetic field model (Tsyganenko, 1987) with the inner edge of the plasma sheet being typically at 6–9 R_E from the Earth. Jacquey *et al.* (1991) concluded on the basis of the magnetic signatures observed in the tail lobes by ISEE-1 that the dipolarisation starts close to the Earth ($R < 15\ R_E$) and propagates tailward. In a multi-point study based on observations in the near-Earth tail, Jacquey *et al.* (1993) found indications that the current disruption associated with the substorm onset starts at 6–9 R_E and propagates tailward after the onset of the substorm expansion. These results, as well as the investigations of substorm phenomena using observations in the auroral zone and GEOS-2 observations (Korth *et al.*, 1991; Roux *et al.*, 1991a, b; Kremser *et al.*, 1992; Ullaland *et al.*, 1993), are consistent with the inner edge of the plasma sheet being the location of expansion phase onsets. Therefore, expansion phase is very likely triggered on closed field-lines by the near-Earth ($R < 10\ R_E$) magnetotail processes in agreement with Lui (1991) and Fairfield, (1992), who further summarised arguments for a near-Earth triggering region.

A most prominent characteristic of the near-Earth Neutral Line (NL) model of substorms (Hones, 1976) is the formation of a plasmoid by magnetic reconnection at substorm onset. In this model an X-type neutral line is formed close to the Earth implying tailward ion flows. McPherron and Hones (1991) found observational evidence for the existence of the near-Earth X-type neutral line to be located between 10 and 20 R_E downtail. On the other hand Baumjohann *et al.* (1989) and Baumjohann *et al.* (1990) analysed a large ion flow data set and magnetic field measurements in the mid-tail ($-9\ R_E < X_{\mathrm{GSM}} < -19\ R_E$; AMTE-IRM). Their observations of the plasma flows in the plasma sheet show that jet-like high-speed flows are often present and that they are dominantly Earthward, which would imply that a possible NL forms somewhere tailward of $-20\ R_E$. In a study based on *Geotail* and IMP-8 data Mitchell *et al.* (1994) found indications of NL formation Earthward of $X = -35\ R_E$. A conclusion based on these observations will be that the distance between the near-Earth NL and the location of expansion phase onset often is too large for a NL formation to be the proximal cause of the expansive phase (Siscoe, 1993).

The four Cluster spacecrafts will cross the current sheet most frequently at large distances (about 19 R_E) which is at the outer edge of the region of interest for local substorm breakup phenomena. Complementary measurements from ground-based instrumentation and from space platforms such as geosynchronous, polar-orbiting, and solar-wind satellites should be used in addition to the RAPID, CIS, and FGM data in order to resolve fast-moving substorm phenomena.

3.4.3. *Substorms and Magnetotail Dynamics*

A major topic to be addressed using energetic-particle measurements is that of acceleration processes in the tail. Energetic particles have been observed continuously over time periods of hours with impulsive time variations on time scales < 1 min. However, because of the motion of the plasma-sheet over a single spacecraft and the limited intensity thresholds in the instrument, it has not been possible to distinguish the continuous plasma-sheet energetic-particle population and its sources from the population produced by impulsive acceleration associated with substorms. Such distinctions are vital to theories of substorms and related induced electric fields such as those associated with tearing mode instability theory. A group of four spacecrafts will make it possible to address this problem by simultaneously sampling nearby regions within the relatively narrow plasma sheet and its boundary layer.

The best direct evidence for particle acceleration and probably the most important energetic phenomena in the magnetosphere are the high-intensity field-aligned 'impulsive' bursts, displaying Inverse Velocity Dispersion (IVD). These events are usually detected at the high-latitude plasma-sheet boundary during thinnings of the plasma sheet. However, a number of cases have been found where 'impulsive' bursts with inverse velocity dispersion were observed well inside the plasma-sheet or during plasma-sheet expansions. These observations suggest that for some events the IVD may be a temporal rather than a spatial effect. However, the most straightforward explanation is that the events are caused by accelerations at a neutral line (Sarris and Axford, 1979). Cluster is a perfect mission for resolving spatial from temporal effects. The RAPID high-resolution electron measurements can provide an extra 'fingerprint' of the acceleration mechanism, which is missing from all previous observations of impulsive bursts because of instrumental limitations.

The passage of a 'source' of energetic particles over a spacecraft inside the plasma-sheet has been inferred on the basis of reversals in both the streaming of the energetic particles and the plasma flow. However, severe objections have been raised to such interpretations of the observations. Cluster must search specifically for such events with good time resolution, since the expected 'reversal' must be observed simultaneously at all energies (within $\sim$ few seconds.) at each spaceceraft. If such an encounter with the 'source' is observed, then the RAPID measurements on the multiple Cluster spacecrafts will be able to measure its size and speed.

Single-spacecraft measurements of the time evolution of the angular distributions of energetic particle intensities during cases of counterstreaming between

energetic ions and electrons have been used to infer the presence of transient ($\sim$ 10–20 s) **E**-fields parallel to the magnetic field. From simultaneous measurements of the variations in the energy spectra of the ambient energetic proton and electron populations under the influence of the $\mathbf{E}_{\parallel}$-field, the 'effective' potential traversed by the energetic particles has been estimated to be a few tens of keV. The region over which the inferred transient $\mathbf{E}_{\parallel}$-field extends may be determined using multi-point observations of such events. Furthermore, such multi-point measurements of various species with different charges will provide an excellent self-consistency test for the assumed existence of the field-aligned **E**-field.

The **B**-field microstructure (i.e., magnetic loops or islands with lengths of a few R_E) which develops in the magnetotail following acceleration events, has been inferred mostly on the basis of single-spacecraft measurements. Suspected neutral line formation in the near-Earth tail region and the subsequent plasma acceleration has led Baker *et al.* (1979) to propose the substorm sequence reproduced in Figure 25. Energetic electron anisotropies were used to indicate whether field-lines were open or closed, but such mapping cannot be certain given the spatial scale sizes and temporal variation. Multiple-spacecraft measurements of energetic particles, plasma and field with good time resolution ($\leq$ few seconds) can contribute to resolving these uncertainties.

Pulsations of the plasma-sheet boundary with periodicities of approximately 2 to 9 min have been detected from measurements of energetic-particle intensities. Such oscillations are not apparent in the measurements of the **B**-field alone. There is strong evidence that these pulsations are due to a standing (and not a travelling) wave at the plasma-sheet boundary.

Energetic particle measurements will also be useful in the tail lobes during periods of observable solar particles. Regions of open lobe field-lines can be identified, and using timing comparisons with SOHO or Wind, the length of open field-lines can be estimated. In the past, incorporating two spacecrafts inside and outside the magnetosphere, the time delay in the entry of solar particles in the lobes of the magnetotail was used in order to infer the 'effective' length of the geotail (Van Allen *et al.*, 1971; Fennell *et al.*, 1973). However, the entry of solar particles into and transport inside the plasma-sheet has not been studied in detail. Recent results have indicated that the access of solar particles into the plasma-sheet is prompt near the neutral sheet and delayed at high plasma-sheet latitudes, being always considerably faster than the particle access in the lobes of the magnetotail. With simultaneous multi-spacecraft observations by Cluster (with spacecrafts located at various distances from the neutral sheet as well as inside the lobes) it will be possible to examine directly the access of solar particles to the different regions under distinct configurations of the upstream field. Furthermore, the study of the expected dawn-dusk asymmetries in the time delay for the entry of solar particles into the plasma-sheet will become possible by multi-spacecraft observations across the magnetopause.
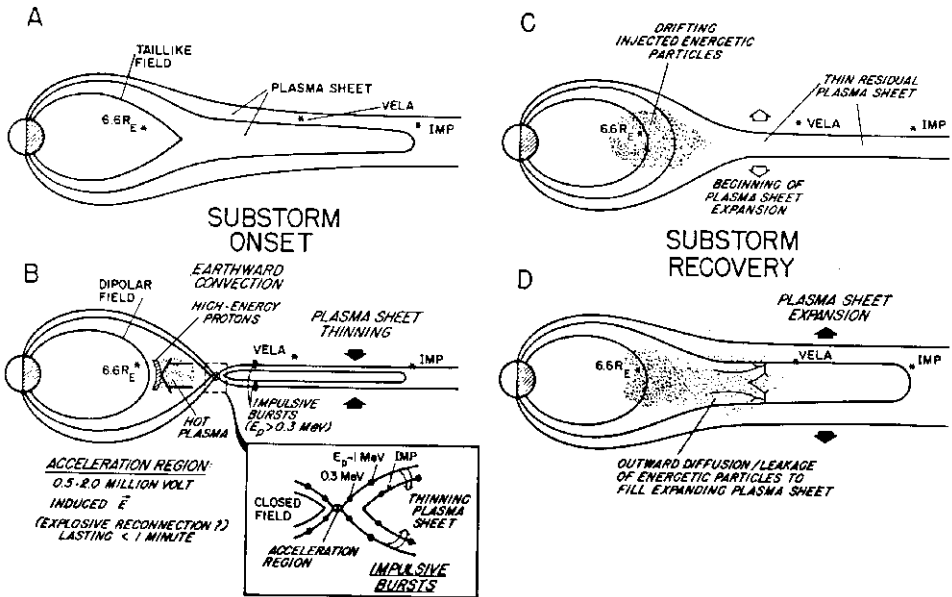
Figure 25. Schematic sequence of energetic particle events predicted by the substorm model of Baker *et al.* (1979). (a) The inner magnetosphere just prior to substorm onset showing the buildup of stress evidenced by the tail-like field. (b) The magnetosphere just after onset showing a dipolar field configuration and the accelerated ion bunches streaming sunward toward the trapped radiation zones and antisunward along the thinning plasma sheet. (c) Conditions just prior to substorm recovery at the beginning of the plasma sheet expansion. (d) Expansion of the plasma sheet and the subsequent filling of the expanding sheet with energetic protons diffusing out of the trapped region.

3.5. DETECTION OF ENERGETIC NEUTRAL ATOMS (ENA)

Energetic neutral atoms are produced in the Earth's magnetosphere through charge exchange between hot ($E \geq 1$ keV) magnetospheric or outflowing ionospheric plasma and the geocorona. The geocorona is an exospheric extension of relatively cold (~ 1000 K) neutral atoms (mainly hydrogen), which resonantly scatter solar Lα radiation. The produced neutrals leave the interaction region with essentially the same energy and velocity direction as the incident ion. In a way the geocorona acts like an imaging screen for magnetospheric/ionospheric ions. Thus, imaging the neutral atom distribution is a means to make the magnetospheric plasma visible. Remote-sensing of energetic neutral atoms (ENA) can provide line-of-sight integrated observations of source populations. The extraction of physical parameters will, however, require unfolding of the product ($j_{ion} \times n_H$) from the line-of-sight integrals (Roelof *et al.*, 1992).

Following the pioneering work of Roelof on the observation of the terrestrial ring current through energetic neutral atom imaging (Roelof *et al.*, 1985; Roelof, 1987), growing attention has been paid by the scientific community to the potential importance of neutral atom imaging for magnetospheric research (Williams *et al.*,

1992; Daglis and Livi, 1995), and several modelling studies were conducted during the last few years (Hesse *et al.*, 1993; Orsini *et al.*, 1994).

The polar orbit of Cluster is particularly favourable for neutral atom imaging of the ring current and near-Earth magnetotail because of the low ion background in the lobes and the polar region. Its relatively long orbital period is ideal for the continuous monitoring of the evolution of dynamical processes in the magnetosphere (storms, substorms).

In order to detect energetic neutral atoms, the RAPID unit on one spacecraft is operated in the ENA Mode as described in Section 2.5.5. In this mode the 10 kV deflection voltage in the collimator is activated. The electric field reduces the transmission of ions with energies below 200 keV by 3 to 4 orders of magnitude. Particles observed in the critical energy band 40–200 keV are then considered neutral atoms. Figure 26 illustrates, as an example, the angular resolution obtainable in the equatorial magnetosphere when Cluster passes over the pole. Although the pixel size is coarse the 'image' can probably detect the location and resolve the spatial extent of plasma injections into the active magnetosphere with sufficient resolution.

The geometry shown in Figure 26 refers clearly to a rather favorable situation in terms of angular resolution and radial distance to the dominant ENA sources. The storm time ENA differential flux at this location can be of the order of 50 part./(cm^2 s sr keV) for energies above 30 keV. At apogee (19.6 R_E) an integral flux of $\prec 1$ part./(cm^2 s keV) is expected.

3.6. HEP/*Geotail* – A PRECURSOR OF RAPID

The energetic-particle package HEP on the Japanese spacecraft *Geotail* (launched 24 July, 1992) contained a first version of an imaging ion spectrometer which is identical to RAPID in all relevant components, performance, and Science Data discussed in this report (except for IES). In a first phase *Geotail* studied the deep tail in double lunar swing-by ecliptic trajectories which, unlike Cluster, allowed extended observations in the plasma sheet. Figure 27 illustrates the IIMS technique for particle identification. Each particle is characterised by an energy (E) and time-of-flight (T) measurement. The sorting parameter in the (E, T) plane is the particle mass A (from the left side the mass lines refer to hydrogen, helium, CNO, and Si–Fe group ions, respectively).

The four frames in Figure 27 document an impulsive oxygen event observed at about $X = -60 \; R_E$ in the magnetotail. The pre-event chemical composition consisted mainly of hydrogen and helium with only little oxygen present. At 19:00 UT the oxygen flux suddenly increased for a short time to a substantial level. These frames are constructed from the Science Data 'Direct Events' (DE) which represent the full resolution of the spectrometer. As mentioned earlier in this report, the majority of these events are reduced on-board to a lower level of precision to meet the telemetry capacity.

RAPID/CL
ENA Imaging
64 pixels max.
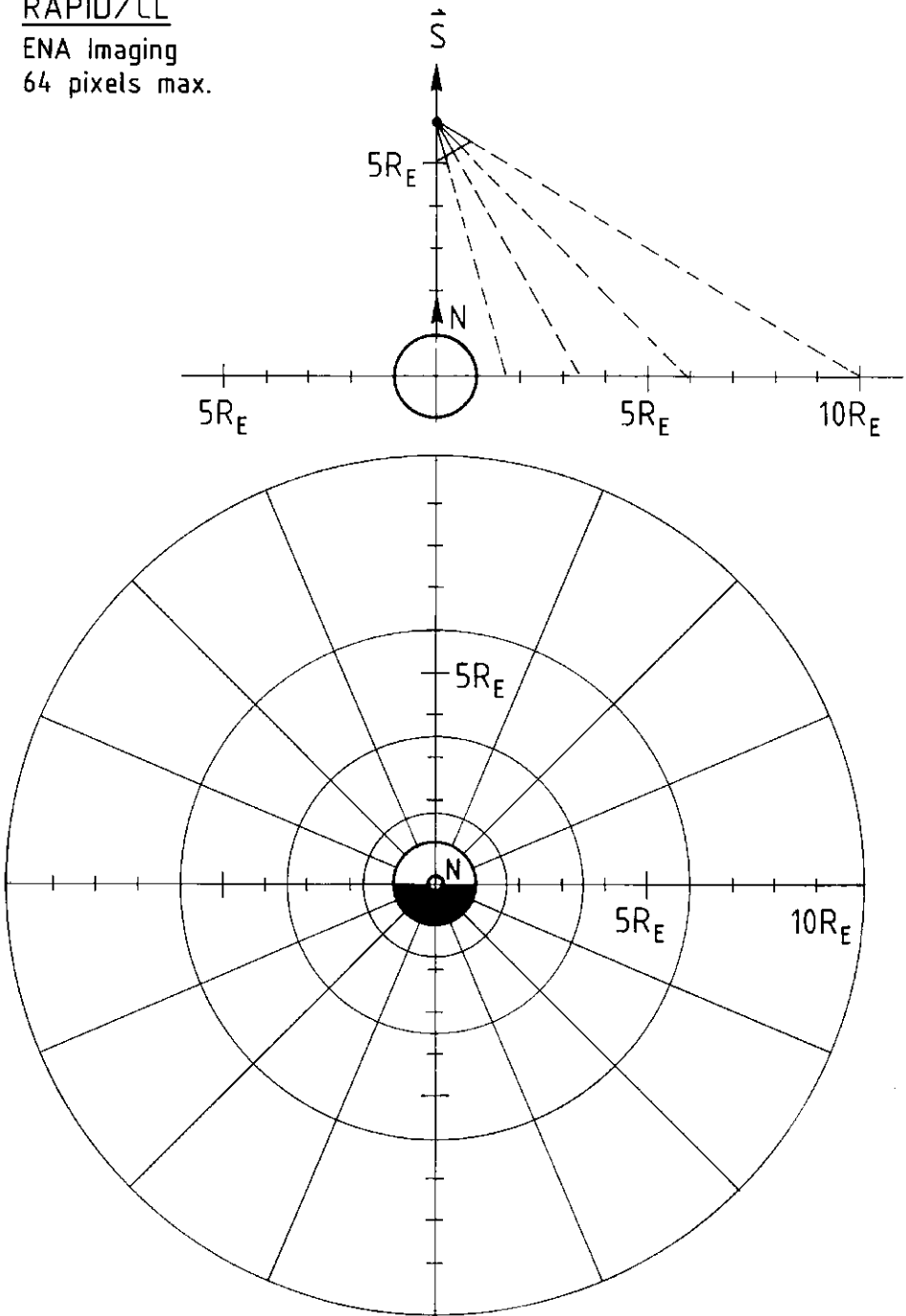
Figure 26. Imaging of energetic neutral atoms in the equatorial magnetosphere. The Cluster spacecraft with RAPID in the ENA mode is assumed to travel over the Northpole. The lower part shows the angular resolution.
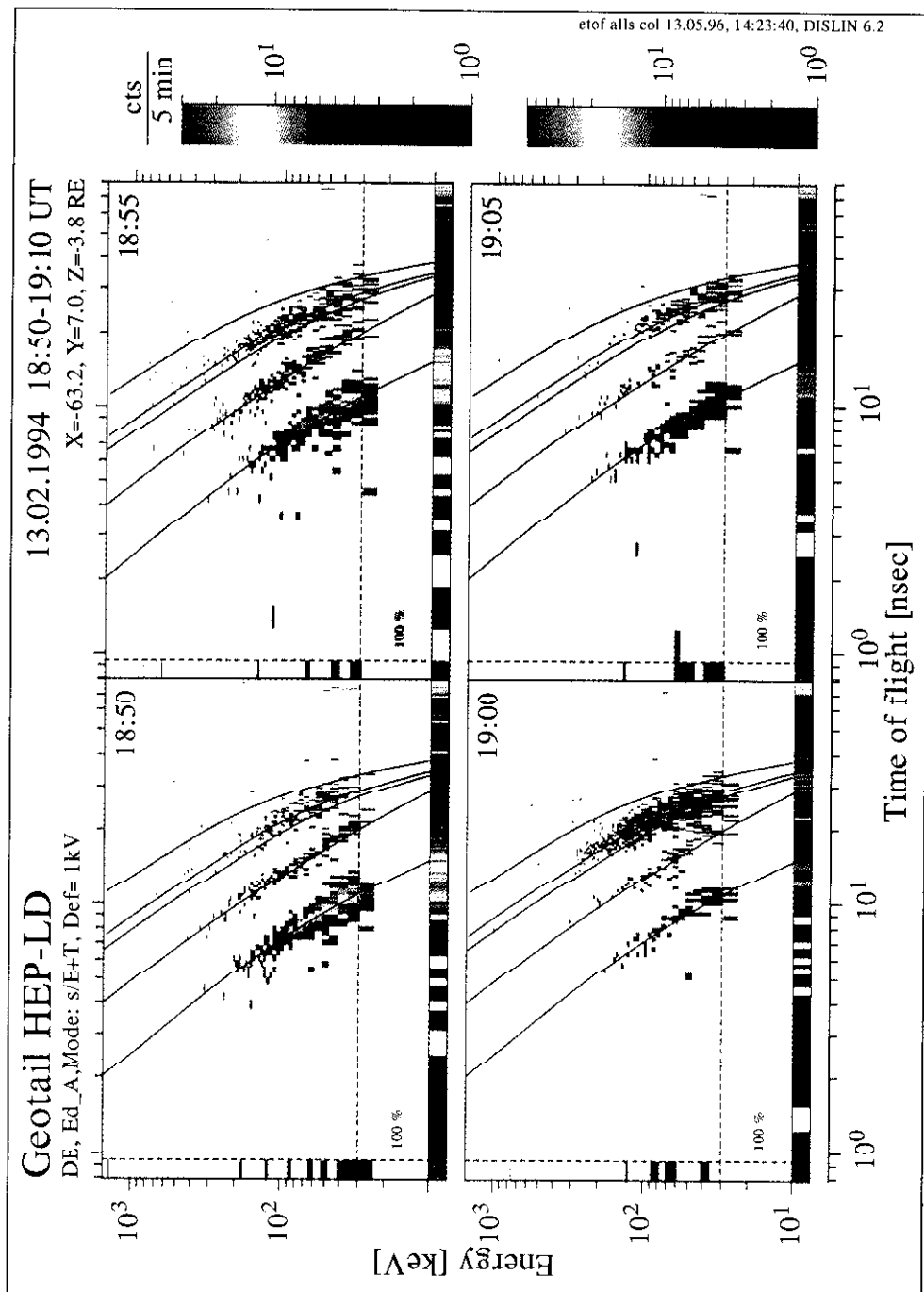
Figure 27. A sequence of two-parameter scatter plots from the spectrometer HEP-LD on *Geotail* demonstrate the mass sorting in the (E, T)-plane. The mass lines identify hydrogen, helium, CNO, and Si–Fe (from the left). A strong oxygen burst occured in the interval 19:00– 9:05 UT in the deep magnetotail (GSE coordinates on the upper right).

Figure 28 shows the evolution of the three-dimensional intensity distributions for the same time intervals. The oxygen (19:00–19:05 UT) appears mainly at or near 90° pitch angle. This is evidence for strong plasma convection potentially driven by a reconnection process Earthward of the spacecraft.

Although *Geotail* observed these oxygen-rich events well tailward of the Cluster nightside apogee distance, the above representations may serve as guidelines for the type of measurements RAPID is expected to return. Most regions of geospace visited by Cluster are expected to show strong angular anisotropies either due to gradients in the plasma or to streaming distributions.

3.7. DERIVATION OF PLASMA PARAMETERS FROM RAPID MEASUREMENTS

The orientation of RAPID on the spacecraft platform and the coverage in phase space (unit sphere) is described in Section 2.5.1. The conversion from observed counting rates n_c to the differential flux intensity j can then be completed through functions of the form

$$j = [GF\epsilon(E, M; SD)]^{-1} n_c , \tag{1}$$

where GF indicates the geometric factor, ϵ denotes the detection efficiency as a function of particle energy E, particle mass M and selected science data channel SD. By definition, the differential directional flux intensity $j(E, \theta, \phi)$ represents the number of particles per energy unit centred at the energy E, per unit area in the direction of (θ, ϕ), per unit time interval, and per unit solid angle; θ and ϕ denote the polar angle and azimuthal angle in the local satellite coordinate system, respectively. It can be shown that $j(E, \theta, \phi)$ is related to the particle-distribution function f in the phase space (E, θ, ϕ) as (Pu *et al.*, 1992)

$$f(E, \theta, \phi) = (m/2)^{1/2} \frac{j(E, \theta, \phi)}{E^{1/2}} , \tag{2}$$

or,

$$f(E_k, \theta_i, \phi_l) = (m/2)^{1/2} \frac{j(E_k, \theta_i, \phi_l)}{E_k^{1/2}} , \tag{3}$$

where $k = 1, 2, \ldots, N_k$ indicates energy channels of the spectrometer, $i = 1, 2, \ldots, N_i$ and $l = 1, 2, \ldots, N_l$ denote the polar and azimuthal looking directions of detectors, respectively. Furthermore, a number of fundamental plasma quantities such as the number density N, the mean velocity $\mathbf{U}$ and the thermal pressure tensor P, etc., can be obtained by calculating moment integrals of $f(E, \theta, \phi)$ (Lundin *et al.*, 1982). Therefore, the observed function $j(E, \theta, \phi)$ may be considered a basic element to derive a variety of plasma parameters (the technique to extract plasma parameters is described in detail by Pu *et al.* (1996)).
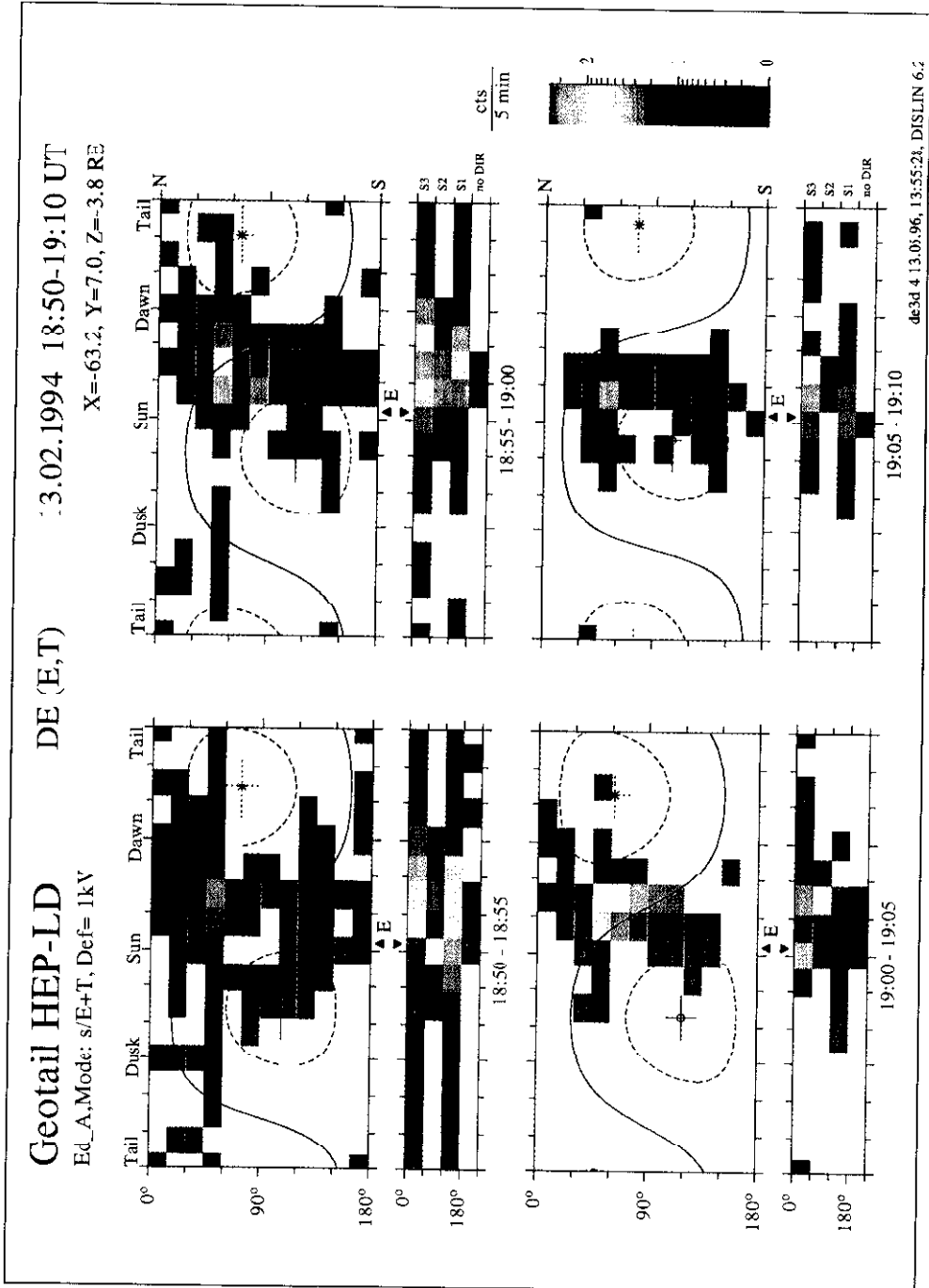
Figure 28. Polar-versus-azimuthal angle displays for the same time intervals as in Figure 27. The color-coded counts per angular bin represent the integral rate (summed over energy and particle mass). Each frame shows the direction of the B-vector and the loci of selected pitch angles ($<5°$ and $135°$ dashed $90°$ heavy line). The small frames are similar displays with reduced resolution in the polar angle ($60°$ only). The intensity increase in the $19:00-19:05$ UT frame is mainly caused by CNO group particles (presumably oxygen) as indicated in Figure 27.

It is possible to transform from the Local Satellite Coordinate System to Boundary-Normal Coordinate Systems, such as the Magnetopause-Normal Coordinate System, the Shock-Normal Coordinate System and the Principle-Axes Coordinate System, by knowing the rotation matrices. We may also define a Local Magnetic Field Line Coordinate System $(x'y'z')$ in which the z' axes is along the local magnetic field. The latter can be obtained either by *in-situ* measurements, or from current magnetic-field models.

Energetic particles measured by RAPID at the same instance in time may originate from different sources. These different groups of particles are heated or accelerated through different mechanisms, and hence may possess different number density, mean velocity and thermal pressure tensor. In general they lie in different energy ranges, and are characterised by different types of distribution functions. Thus, it makes more sense for the derivation of plasma parameters to begin with distinguishing different populations of particles, and then to calculate moment integrals for them separately.

4. Summary

The dual sensor system in the RAPID spectrometer identifies energetic electrons and ions in the energy range 20–400 keV and 10 keV nucl^{-1}–4000 keV, respectively. The moderate ion mass resolution of about 4 (for oxygen ions) allows the identification of all ions and ion groups with significance in geospace plasmas.

Novel concepts are employed in the sensor systems to achieve angular resolution over a 180° range in polar angle. The imaging ion mass spectrometer IIMS uses two-dimensional time-of-flight/energy analysis to determine the particle mass. Addition of position sensing on the entrance foil (START foil) is a major evolutionary step in the detection technique which, in combination with a geometrically small STOP detector (at the end of the flight path), provides direction sensitivity. This approach divides the 180° polar range in 12 contiguous angular intervals. Sectoring the satellite spin plane with a maximum of 16 azimuthal intervals covers the unit sphere in velocity space completely with a total of 192 angular bins.

The imaging electron spectrometer IES achieves directional sensitivity by using novel microstrip solid-state devices in combination with a pin-hole acceptance. This technique divides the 180° polar range into 9 angular intervals which, with 16 sectors in the spin plane, corresponds to a total of 144 bins on the unit sphere. A major thrust of the paper is to show the signal processing and the formation of so-called Science Data which contain the ultimate return from RAPID.

The advanced RAPID concept represents an important scientific tool in the complement of plasma instruments on-board the four Cluster spacecraft. New capabilities of the novel spectrometer type permit a variety of studies in all regions of geospace visited by Cluster. Three selected areas, the bow shock and upstream region, reconnection at the magnetopause and FTEs, and substorms and the dynam-

ics in the magnetotail are discussed in detail to highlight outstanding physical problems to be addressed by the RAPID investigation, and to emphasise specific contributions expected from studies of the suprathermal plasma component. On a broader scale, the three instruments RAPID, CIS, and PEACE form a set of spectrometers which covers an energy range from 0.7 eV to 400 keV for electrons and approximately 0 keV to 4000 keV for ions. This wide energy range is a pre-requisite for advanced studies in geospace.

Acknowledgements

University Center for Space Physics; and with Contract Number NAS5-31452 at The Aerospace Corporation, Los Angeles.

References

Akasofu, S. I.: 1991, in J. R. Kan, T. A. Potemra, and T. Iijima (eds.), 'Development of Magnetospheric Physics', *Magnetospheric Substorms*, Geophysical Monograph 64, American Geophysical Union, p. 3.

Anagnostopoulos, G. C. and Kaliabetsos, G. D.: 1994, 'Shock Drift Acceleration of Energetic ($E \geq 50$ keV) Protons and ($E \geq 37$ keV nucl^{-1}) Alpha Particles at the Earth's Bow Shock as a Source of the Magnetosheath Energetic Ion Events', *J. Geophys. Res.* **99**, 2335.

Andrews, M. K. *et al.*: 1981, 'Plasma Sheet Motions Inferred from Medium-Energy Ion Measurements', *J. Geophys. Res.* **86**, 7543.

Asbridge, J. R. *et al.*: 1968, 'Outward Flow of Protons from the Earth's Bow Shock', *J. Geophys. Res.* **73**, 5777.

Axford, W. I.: 1981, 'Acceleration of Cosmic Rays by Shock Waves', workshop on Plasma Astrophysics, organised by the International School of Plasma Physics, held at Varenna, Italy, *ESA SP-161*, p. 425.

Baker, D. N. and Stone, E. C.: 1976, 'Energetic Electron Anisotropies in the Magnetotail: Identification of Open and Closed Field-Lines', *Geophys. Res. Letters* **3**, 557.

Baker, D. N. and Stone, E. C.: 1977a, 'The Magnetopause Electron Layer Along the Distant Magnetotail', *Geophys. Res. Letters* **4**, 133.

Baker, D. N. and Stone, E. C.: 1977b, 'The Relationship of Energy Flow at the Magnetopause to Geomagnetic Activity', *Geophys. Res. Letters* **4**, 395.

Baker, D. N. and Stone, E. C.: 1978, 'The Magnetopause Energetic Electron Layer. 1. Observations Along the Distant Magnetotail', *J. Geophys. Res.* **83**, 4327.

Baker, D. N. *et al.*: 1979, 'High-Energy Magnetospheric Protons and Their Dependence on Geomagnetic and Interplanetary Conditions', *J. Geophys. Res.* **84**, 7138.

Baker, D. N., Hones, E. W., Jr., Higbie, P. R., Belian, R. D., and Stauning, P.: 1981, 'Global Properties of the Magnetosphere During a Substorm Growth: A Case Study', *J. Geophys. Res.* **86**, 8941.

Baker, D. N., Higbie, P. R., Belian, R. D., Hones, E. W., and Klebesadel, R. W.: 1982, in C. T. Russel and D. J. Southwood (eds.), 'The Los Alamos Synchronous Orbit Date Set', *The IMS Source Book*, AGU, Washington DC, p. 82.

Baker, D. N., Akasofu, S. I., Baumjohann, Bieber, J. W., Fairfield, D. H., Hones, E. W., Jr., Mauk, B. H., McPherron, R. L., and Moore, T. E.: 1984, 'Substorms in the Magnetosphere, Chapter 8 of Solar Terrestrial Physics - Present and Future', *NASA Publ.*, Washington DC, p. 1120.

Baker, D. N., Simpson, J. A., and Eraker, J. H.: 1986, 'A Model of Impulsive Acceleration and Transport of Energetic Particles in Mercury's Magnetosphere', *J. Geophys. Res.* **91**, 8742.

Baumjohann, W., Paschmann, G., and Cattell, C. A.: 1989, 'Average Plasma Properties in the Central Plasma Sheet', *J. Geophys. Res.* **94**, 6597.

Baumjohann, W., Paschmann, G., and Lühr, H.: 1990, 'Characteristics of High-Speed Ion Flows in the Plasma Sheet', *J. Geophys. Res.* **95**, 3801.

Bieber, J. W., Stone, E. C., Hones, E. W., Jr., Baker, D. N., and Bame, S. J.: 1982, 'Plasma Behavior During Energetic Electron Streaming Events: Further Evidence for Substorm-Associated Magnetic Reconnection', *Geophys. Res. Letters* **9**, 664.

Crooker, N. U.: 1979, 'Dayside Merging and Cusp Geometry', *J. Geophys. Res.* **84**, 951.

Daglis, I. A. and Livi, S.: 1995, 'Merits for Substorm Research from Imaging of Charge-Exchange Neutral Atoms', *Ann. Geophys.* **13**, 505.

Daly, P. W. and Keppler, E.: 1989, 'Observation of a Flux Transfer Event on the Earthward Side of the Magnetopause', *Planetary Space Sci.* **30**, 331.

Daly, P. W. *et al.*: 1984, 'The Distribution of Reconnection Geometry in Flux Transfer Events Using Energetic Ion, Plasma, and Magnetic Data', *J. Geophys. Res.* **89**, 3843.

Dungey, J. W.: 1961, 'Interplanetary Magnetic Field and Auroral Zones', *Phys. Res. Letters* **6**, 47.

Dungey, J. W.: 1963, in C. DeWitt, J. Hiebolt, and A. Lebeau (eds.), 'The Structure of the Ionosphere, or Adventures in Velocity Space', *Geophysics: The Earth's Environment*, Gordon and Breach, New York, p. 526.

Ellison, D. C.: 1985, 'Shock Acceleration of Diffusive Ions at the Earth's Bow Shock: Acceleration Efficiency and A/Z Enhancement', *J. Geophys. Res.* **90**, 29.

Elphinstone, R. D., Murphree, J. S., Cogger, L. L., Hearn, D., Henderson, M. G., and Lundin, R.: 1991, in J. R. Kan, T. A. Potemra, and T. Iijima (eds.), 'Observations of Changes to the Auroral Distribution Prior to Substorm Onset', *Magnetospheric Substorms*, Geophys. Monogr. Ser. 64, AGU, Washington, D.C., p. 257.

Fahnenstiel, S. C.: 1981, 'Standing Waves Observed at the Dayside Magnetopause', *Geophys. Res. Letters* **11**, 1155.

Fairfield, D. H.: 1992, 'Advances in Magnetospheric Storm and Substorm Research: 1989–1991', *J. Geophys. Res.* **97**, 10 865.

Fennell, J. F. *et al.*: 1973, 'Access of Solar Protons to the Earth's Polar Caps', *J. Geophys. Res.* **78**, 1036.

Fennell, J. F., Roeder, J., Spence, H., Livi, S., and Grande, M.: 1993, *Composition Changes in Association with Energetic Particle Flux Drop Outs*, IAGA, Buenos Aires.

Fritz, T. A. *et al.*: 1982, 'The Magnetopause as Sensed by Energetic Particles, Magnetic Field, and Plasma Measurements on November 22, 1977', *J. Geophys. Res.* **87**, 2133.

Fritz, T. A., Baker, D. N., McPherron, R. L., and Lennartsson, W.: 1984, in E. W. Hones Jr. (ed.), 'Implications of the 11:00 UT March 22, 1979 CDAW-6 Substorm Event for the Role of Magnetic Reconnection in the Geomagnetic Tail', *Magnetic Reconnection in Space and Laboratory Plasmas*, Vol. 203, AGU, Washington DC.

Gosling, J. T. *et al.*: 1978, 'Observations of Two Distinct Populations of Bow-Shock Ions in the Upstream Solar Wind', *Geophys. Res. Letters* **5**, 957.

Gosling, J. T., Baker, D. N., Bame, S. J., Hones, E. W., Jr., McComas, D. J., Zwickl, R. D., Slavin, J. A., Smith, E. J., and Tsurutani, B. T.: 1984, 'Plasma Entry Into the Distant Tail Lobes: ISEE-3', *Geophys. Res. Letters* **11**, 1078.

Gosling, J. T., Baker, D. N., Bame, S. J., Feldman, W. C., and Zwickl, R. D.: 1985, 'North-South and Dawn-Dusk Plasma Asymmetries in the Distant Tail Lobes: ISEE 3', *J. Geophys. Res.* **90**, 6354.

Hesse, M., Smith, M. F., Herrero, F., Ghielmetti, A. G., Shelley, E. G., Wurz, P., Bochsler, P., Gallagher, D. L., Moore, T. E., and Stephen, T. S.: 1993, 'Imaging Ion Outflow in the High-Latitude Magnetosphere Using Low-Energy Neutral Atoms', *Society of Photo-Optical Instrumentation Engineers, Title: Instrumentation for Magnetospheric Imagery II*, **2008**, 83.

Hones, E. W., Jr.: 1976, in D. J. Williams (ed.), 'The Magnetotail: Its Generation and Dissipation', *Physics of Solar Planetary Env.*, AGU, Washington, D.C., p; 559.

Ipavich, F. M. *et al.*: 1981a, 'Temporal Development of Composition, Spectra and Anisotropies During Upstream Particle Events', *J. Geophys. Res.* **86**, 11153.

Ipavich, F. M. *et al.*: 1981b, 'A Statistical Survey of Ions Observed Upstream of the Earth's Bow Shock: Energy Spectra, Composition and Spatial Variation', *J. Geophys. Res.* **86**, 4337.

Jacquey, C., Sauvaud, J. A., and Dandouras, J.: 1991, 'Location and Propagation of the Magnetotail Current Disruption During Substorm Expansion: Analysis and Simulation of an ISEE Multi-Onset Event', *Geophys. Res. Letters* **18**, 389.

Jacquey, C., Sauvaud, J. A., Dandouras, J., and Korth, A.: 1993, 'Tailward Propagating Cross-Tail Current Disruption and Dynamics of Near-Earth Tail: A Multi-Point Measurement Analysis', *Geophys. Res. Letters* **20**, 983.

Kaufmann, R. L.: 1987, 'Substorm Currents: Growth Phase and Onset', *J. Geophys. Res.* **92**, 7471.

Korth, A., Pu, Z. Y., Kremser, G., and Roux, A.: 1991, in J. R. Kan, T. A. Potemra, and T. Iijima (eds.), 'A Statistical Study of Substorm Onset Conditions at Geostationary Orbit', *Magnetospheric Substorms*, Geophysical Monograph 64, American Geophysical Union, p. 343.

Korth, A. *et al.*: 1982, 'Two-Satellite Study of Proton Drift on Quiet Days', *Adv. Space Res.* **1**, 173.

Kremser, G., Tanskanen, P., Ullaland, S., Perraut, S., Roux, A., and Korth, A.: 1992, 'Influence of Storm Sudden Commencements on Magnetospheric Substorms', *Proc. International Conference on Substorms ICS-1*, March 23–27 1992, Kiruna, Sweden, ESA SP-335, p. 291.

Lee, M. A.: 1982, 'Coupled Hydromagnetic Wave Excitation and Ion Acceleration Upstream of the Earth's Bow Shock', *J. Geophys. Res.* **87**, 5093.

Lee, M. A.: 1983, 'Coupled Hydromagnetic Wave Excitation and Ion Acceleration at Interplanetary Traveling Shocks', *J. Geophys. Res.* **88**, 6109.

Lee, L. C. and Fu, Z. F.: 1985, 'A Theory of Magnetic Flux Transfer Events at the Earth's Magnetopause', *Geophys. Res. Letters* **12**, 105.

Lin, R. P. *et al.*: 1974, '30-to-100 keV protons Uplasma-Sheettream of the Earth's Bow Shock', *J. Geophys. Res.* **79**, 489.

Liu, Z. X. and Hu, Y. D.: 1988, 'Local Magnetic Field Reconnection Caused by Vortices in the Flow Field', *Geophys. Res. Letters* **15**, 752.

Liu, Z. X., Mu, S., and Pu, Z. Y.: 1994, 'Magnetic Field Configuration at Magnetopause for Different IMF Conditions', *Chinese Sci. Bull.* **39**, 1759.

Liu, Z. X., Zhu, Z., and Pu, Z. Y.: 1995, 'Transient Reconnection at High Latitude Boundary Layer', *Acta Geophys. Sinica* **39**, 1.

Lopez, R. E.: 1993, 'Auroral and Related Phenomena', *Adv. Space Res.* **4** (13), 189.

Lui, A. T. Y.: 1991, 'A Synthesis of Magnetospheric Substorm Models', *J. Geophys. Res.* **96**, 1849.

Lundin, R., Hultqvist, B., Pissarenko, N., and Zackarov, A.: 1982, 'The Plasma Mantle', *Space Sci. Rev.* **31**, 247.

McDiarmid, I. B., Burrows, J. R., and Wilson, M. D.: 1978, 'Magnetic Field Perturbation in the Dayside Cleft and Their Relationship to the IMF', *J. Geophys. Res.* **83**, 5753.

McPherron, R. L.: 1972, 'Substorm Related Changes in the Geomagnetic Tail: the Growth Phase', *Planetary Space Sci.* **20**, 1521.

McPherron, R. L. and Hones, E. W., Jr.: 1991, 'Relation of the Substorm Current Wedge to Dropout of the Near-Earth Plasma Sheet', *EOS* **72** (17), 251.

Maezawa, K.: 1976, 'Magnetic Convection Induced by the Positive and Negative Z-Components of the Interplanetary Magnetic Field: Quantitative Analysis Using Polar Cap Magnetic Records', *J. Geophys. Res.* **81**, 2289.

Mitchell, D. G. and Roelof, E. C.: 1983, 'Dependence of 50-keV Uplasma-Sheettream Ion Events at IMP 7&8 Upon Magnetic Field Bow Shock Geometry', *J. Geophys. Res.* **88**, 5623.

Mitchell, D. G., Angelopoulus, V., McEntire, R. W., Williams, D. J., Lui, A. T. Y., Decker, R. B., Krimigis, S. M., Roelof, E. C., Christon, S. P., Kokubun, S., Yamamoto, T., Paterson, W., Frank, L. A., Lepping, R. P., and Reeves, G. D.: 1994, 'Two-Point Correlations of Energetic Particle Beams in the Magnetotail', *EOS Trans. AGU* **75** (43), 575.

Orsini, S., Daglis, I. A., Candidi, M., Hshieh, K. C., Livi, S., and Wilken, B.: 1994, 'Model Calculation of Energetic Neutral Atoms Precipitation at Low Altitudes', *J. Geophys. Res.* **99**, 13 489.

Paschalidis, N. P., Sarris, E. T., Krimigis, S. M., McEntire, R. W., Levine, M. D., Daglis, I. A., and Anagnostopoulos, G. C.: 1994, 'Energetic Ion Distributions on Both Sides of the Earth's Magnetopause', *J. Geophys. Res.* **99**, 8687.

Paschmann, G. *et al.*: 1979, 'Plasma Acceleration at the Earth's Magnetopause: Evidence for Reconnection', *Nature* **282**, 243.

Paschmann, G *et al.*: 1980, 'Energization of Solar Wind Ions by Reflection from the Earth's Bow Shock', *J. Geophys. Res.* **85**, 4689.

Paschmann, G. *et al.*: 1981, 'Characteristics of Reflected and Diffuse Ions Upstream from the Earth's Bow Shock', *J. Geophys. Res.* **86**, 4355.

Paschmann, G. *et al.*: 1982, 'Plasma and Magnetic Field Characteristics of Magnetic Flux Transfer Events', *J. Geophys. Res.* **87**, 2159.

Pu, Z. Y. and Zong, Q-G.: 1996, *Plasma Parameters Derived from Data obtained with an Energetic Particle Spectrometer Onboard a Satellite*, MPAE-W-056-96-03.

Pu, Z. Y., Korth, A., and Kremser, G.: 1992, 'Plasma and Magnetic Field Parameters at Substorm Onsets Derived from GEOS 2 Observations', *J. Geophys. Res.* **97**, 19 341.

Rijnbeek, R. P. *et al.*: 1984, 'A Survey of Dayside Flux Transfer Events Observed by ISEE, 1 and 2 Magnetometers', *J. Geophys. Res.* **89**, 786.

Roelof, E. C., Mitchell, D. G., and Williams, D. J.: 1985, 'Energetic Neutral Atoms ($E \sim 50$ keV) from the Ring Current: IMP 7/8 and ISEE, 1', *J. Geophys. Res.* **90**, 10 991.

Roelof, E. C.: 1987, 'Energetic Neutral Atom Image of Storm-Time Ring Current', *Geophys. Res. Letters* **14**, 652.

Roelof, E. C., Mauk, B. H., and Meier, R. R.: 1992, 'Instrument Requirements for Imaging the Magnetosphere in Extreme-Ultraviolet and Energetic Neutral Atoms Derived from Computer-Simulated Images', *Society of Photo-Optical Instrumentation Engineers, Title: Instrumentation for Magnetospheric Imagery* **1744**, 19.

Rostoker, G., Akasofu, S. I., Forster, J., Greenwald, R. G., Kamide, Y., Kawasaki, K., Lui, A. T. Y., McPherron, R. L., and Russel, C. T.: 1980, 'Magnetospheric Substorms – Definition and Signatures', *J. Geophys. Res.* **85**, 1663.

Roux, A., Perraut, S., Robert, P., Morane, A., Pedersen, A., Korth, A., Kremser, G., Aparicio, B., Rodgers, D., and Pellinen, R.: 1991a, 'Plasma Sheet Instability Related to the Westward Traveling Surge', *J. Geophys. Res.* **96**, 17 697.

Roux, A., Perraut, S., Morane, A., Robert, P., Korth, A., Kremser, G., Pedersen, A., Pellinen, R., and Pu, Z. Y.: 1991b, in J. R. Kan, T. A. Potemra, and T. Iijima (eds.), 'Role of the Near-Earth Plasmasheet at Substorms', *Magnetospheric Substorms*, Geophysical Monograph 64, American Geophysical Union, p. 201.

Russell, C. T.: 1972, 'The Configuration of the Magnetosphere', in E. R. Dyer, Jr. (ed.), *Critical Problems of Magnetospheric Physics*, National Academy of Sciences, Washington D.C., p. 1.

Russell, C. T. and Elphic, R. C.: 1978, 'Initial ISEE Magnetometer Results: Magnetopause Observations', *Space Sci. Rev.* **22**, 681.

Russell, C. T. and Elphic, R. C.: 1979, 'ISEE Observations of Flux Transfer Events at the Dayside Magnetopause', *Geophys. Res. Letters* **6**, 33.

Sarris, E. T. and Axford, W. I.: 1979, 'Energetic Protons Near the Plasma Sheet Boundary', *Nature* **277**, 460.

Sarris, E. T. *et al.*: 1986, 'Simultaneous Measurements of Energetic Ion ($\geq$ 50 keV) and Electron ($\geq$ 220 keV) Activity Upstream of Earth's Bow Shock and Inside the Plasma Sheet: Magnetospheric Source for the November 3 and December 3, 1977 Upstream Events', preprint.

Saunders, M. A.: 1983, 'Recent ISEE Observations of the Magnetopause and Low Latitude Boundary Layer: A Review', *J. Geophys.* **52**, 190.

Saunders, M. A. *et al.*: 1984, 'Flux Transfer Events: Scale Size and Interior Structure', *Geophys. Res. Letters*, **11** 131.

Sauvaud, J. A. and Winkler, J. R.: 1980, 'Dynamics of Plasma, Energetic Particles, and Fields Near Synchronous Orbit in the Nighttime Sector During Magnetospheric Substorms', *J. Geophys. Res.*, **85** 2043.

Scholer, M.: 1988, 'Magnetic Flux Transfer Events at the Magnetopause Based on Single X-Line Burst Reconnection', *Geophys. Res. Letters* **15**, 291.

Scholer, M. *et al.*: 1979, 'Pitch Angle Distributions of Energetic Protons Near the Earth's Bow Shock', *Geophys. Res. Letters* **6**, 707.

Scholer, M., Gloeckler, G., Hovestand, D., Ipavich, F. M., Klecker, B., Baker, D. N., Baumjohann, W., and Tsurutani, B. T.: 1984, 'Simultaneous Observation of the Plasma Sheet in the Near Earth and Distant Magnetotail, ISEE-1 and ISEE-3', *Geophys. Res. Letters* **11**, 1034.

Scholer, M., Baker, D. N., Bame, S. J., Baumjohann, W., Gloeckler, G., Smith, E. J., and Tsurutani, B. T.: 1985, 'Correlated Observations of Substorm Effects in the Near Earth Region and the Distant Magnetotail', *J. Geophys. Res.* **90**, 4021.

Schunk, R. W.: 1988, 'Magnetosphere-Ionosphere-Thermosphere Coupling Processes', in *Solar-Terrestrial Energy Program: Major Scientific Problems*, Proc. of a SCOSTEP Symposium, held during the XXVII COSPAR Planetary Meeting, p. 52.

Siscoe, G.: 1993, 'Recent Activity in Substorm Research', *Adv. Space Res.* **4** (13), 165.

Sofko, G. J. *et al.*: 1979, in B. Battrick (ed.), 'STARE Ionospheric Electron Flows During the August 28, 1978 GEOS-2 Magnetopause Crossing', *Proc. Magnetospheric Boundary Layers Conf.*, Alpbach, ESA SP-148, p. 183.

Song, P. and Russell, C. T.: 1992, 'Model of the Low-Latitude Boundary Layer for Strongly Northward Interplanetary Magnetic Field', *J. Geophys. Res.* **97**, 1411.

Sonnerup, B. U. Ö.: 1969, 'Acceleration of Particles Reflected at a Shock Front', *J. Geophys. Res.* **74**, 1301.

Sonnerup, B. U. Ö., Paschmann, G., Papamastorakis, I., Sckopke, N., Haerendel, G., Bame, S. J., Asbridge, J. R., Gosling, J. T., and Russell, C. T.: 1981, 'Evidence for Magnetic Field Reconnection at the Earth's Magnetopause', *J. Geophys. Res.* **86**, 10049.

Southwood, D. J., Farrugia, C. J., and Saunders, M. A.: 1988, 'What Are Flux Transfer Events', *Planatary Space Sci.* **36**, 503.

Southwood, D. J. *et al.*: 1988, 'What Are Flux Transfer Events?', *Planetary Space Sci.* **36** (II), 503.

Stasiewicz, K.: 1991, 'A Global Model of Gyroviscous Field-Line Merging at the Magnetopause', *J. Geophys. Res.* **96**, 77.

Tsyganenko, N. A.: 1987, 'Global Quantitative Models of the Geomagnetic Field in the Cislunar Magnetosphere for Different Disturbance Levels', *Planetary Space Sci.* **35**, 1347.

Ullaland, S., Kremser, G., Tanskanen, P., Korth, A., Roux, A., Torkar, K., Block, L. P., and Iversen, I. B.: 1993, 'On the Development of a Magnetospheric Substorm Influenced by a Storm Sudden Commencement: Ground, Balloon, and Satellite Observations', *J. Geophys. Res.* **98**, 15 381.

Van Allen, J. A. *et al.*: 1971, 'Asymmetric Access of Energetic Solar Protons to the Earth's North and South Polar Caps', *J. Geophys. Res.* **76**, 4262.

Wibberenz, G. *et al.*: 1985, 'Dynamics of Intense Upstream Ion Events', *J. Geophys. Res.* **90**, 283.

Wilken, B.: 1984, 'Identification Techniques for Nuclear Particles in Space Plasma Research and Selected Experimental Results', *Rep. Prog. Phys.* **47**, 767.

Wilken, B., Zong, Q. G., Daglis, I. A., Doke, T., Livi, S., Maezawa, K., Pu, Z. Y., Ullaland, S., Yamamoto, T.: 1995, 'Tailward Flowing Energetic Oxygen Ion Bursts Associated with Multiple Flux Ropes in the Distant Magnetotail: *Geotail* Observations', *Geophys. Res. Letters*, accepted.

Williams, D. J., Roelof, E. C., Mitchell, D. G.: 1992, 'Global Magnetospheric Imaging', *Rev. Geophys.* **30**, 183.

Yeoman, T., Lühr, H., Friedel, R. W. H., Coles, S., Grande, M., Perry, C. H., Lester, M., Smith, P. N., Orr, D., and Singer, H.: 1997, CRRES: Ground-Based Multi-Instrument Observations of an Interval of Substorm Activity', *Ann. Geophys.*, submitted.

Zhang, H. and Liu, Z. X.: 1995, 'Manifestation of Disturbance at Magnetopause in Plasmasheet', *Chinese Sci. Bull.*, submitted.

Zhang, H., Liu, Z. X., and Pu, Z. Y.: 1995, 'Transient Reconnection at Nightside Magnetopause', *J. Geophys. Res.*, submitted.